1-1-2010

Application Of FBG Sensors For Fatigue Monitoring Of Advanced Polymer Matrix Composites

Marina Selezneva
Ryerson University

APPLICATION OF FBG SENSORS FOR FATIGUE MONITORING OF ADVANCED POLYMER MATRIX COMPOSITES

by

Marina Selezneva

Bachelor of Aerospace Engineering

Ryerson University, 2008

A thesis

presented to Ryerson University

in partial fulfillment of the

requirements for the degree of

Master of Applied Science

in the Program of

Aerospace Engineering

Toronto, Ontario, Canada, 2010

Author's Declaration

I hereby declare that I am the sole author of this thesis.

I authorize Ryerson University to lend this thesis to other institutions or individual for the purpose of scholarly research.

Signature

I further authorize Ryerson University to reproduce this thesis by photocopying or by other means, in total or in part, at the request of other institutions or individuals for the purpose of scholarly research.

Signature

APPLICATION OF FBG SENSORS FOR FATIGUE MONITORING OF ADVANCED POLYMER MATRIX COMPOSITES

Marina Selezneva – Ryerson University, Toronto

Master of Applied Science – Aerospace Engineering – 2010

Abstract

The utilization of polymer matrix composites (PMCs) in the aerospace industry has increased over the last decade due to their high specific strength. The next generation of PMCs has the potential of being used for applications at elevated temperature (ET). Work conducted in this thesis is aimed at developing test methodology for the characterization of fatigue behavior of PMCs at ET. Conventional strain measurement techniques (e.g. strain gages and extensometers) have limited applicability during cyclic loading. An alternative strain sensing technology is the Fiber Bragg Grating (FBG) sensor. In this thesis surface mounted and embedded FBG sensors are used to monitor stiffness degradation and damage development in woven PMCs during fatigue loading at temperatures up to 200°C. Results demonstrate the applicability of FBGs for fatigue monitoring of PMCs in this temperature range. Also, the effect of temperature on the off-axis properties of PMCs is captured and discussed.

Acknowledgements

My thesis would have not been possible without the support of many people and organizations for which I am very grateful.

I am immensely thankful to my supervisors, Dr. Zouheir Fawaz, Dr. Cheung Poon and Dr. Kamran Behdinan for their encouragement, guidance and support from the initial to the final stages of my thesis. I am especially grateful to them for giving me the opportunity to participate in conferences and international exchange programs.

I am also very thankful to the Natural Sciences and Engineering Research Council of Canada (NSERC), Consortium for Research and Innovation in Aerospace in Quebec (CRIAQ), Pratt & Whitney Canada, Rolls Royce and the Office of International Affairs at Ryerson University for their financial support.

I would also like to express my deepest gratitude to Dr. Xijia Gu, from the department of Electrical Engineering, whose knowledge and assistance were vital to the successful completion of my thesis. I am also thankful for the sensors Dr. Xijia Gu had provided me with.

I am greatly appreciative of Dr. Hiroyuki Hamada, Dr. Asami Nakai, with the department of Advanced Fibro Science at the Kyoto Institute of Technology (KIT) in Kyoto, Japan, for the warm hospitality during my work term at KIT.

I would like to thank our technical officers, Peter Bradley, Alan Machin and Qiang Li, whose support and guidance were also responsible for the successful completion of my Master Degree.

I would also like to acknowledge the help and support of David Begg, from the Office of International Affairs, who prepared me for my trips abroad with invaluable knowledge and advice.

I would like to extend a special thank you to my colleagues, John Montesano, Viktor Kulisek, Jordy Balvers and Brian Petz for their academic expertise and most importantly for the much needed motivation and emotional support.

Most importantly, I wish to express gratitude to my mother, Lioudmila Selezneva for her understanding and endless love through the duration of my studies.

Table of Contents

List of Tables

List of Figures

List of Nomenclature

List of Abbreviations

BMI	bismaleimide (polymer)
ET	elevated temperature
FB	fully bonded (FBG)
FBG	fiber Bragg Grating
FRAMES	Facility for Research on Aerospace Materials and Engineered Structures
LVDT	linear voltage differential transducer
OF	optical fiber
OSA	optical spectrum analyzer
PB	partially bonded (FBG)
PMC	polymer matrix composite
RT	room temperature
SEM	scanning electron microscope
SG	strain gage
UTS	ultimate tensile strength

List of Symbols

E	elastic modulus
E_1	longitudinal elastic modulus
E_2	transverse elastic modulus
F	fatigue modulus
f	factor that combines all the photoelastic constant
G_{12}	shear modulus
I_A	peak intensity of the debonded portion of the FBG
I_B	peak intensity of the bonded portion of the FBG
K_T	coefficient of thermal sensitivity of the FBG
N	factor used to scale the number of cycles and strain values
n	number of cycles

n_{eff}	index of refraction of an optical fiber
P_{ij}	Pockel's coefficient
R	stress ration of the minimum applied cyclic stress over the maximum
S-N	relationship between the applied stress and the number of cycles to failure
T	temperature
$T_{Desired}$	desired test temperature
$T_{Fatigue}$	surface temperature of the specimen during fatigue
$T_{Furnace}$	set furnace temperature
$T_{Surface}$	surface temperature of the specimen
Tg	glass transition temperature of the polymer
α	coefficient of thermal expansion
ΔT	change of temperature
ε	strain
Λ	period of the grating
λ_B	Bragg wavelength
σ	stress
ν	Poisson's ratio

1 Introduction

1.1 Background

Developments in the aerospace industry are largely driven by the demand to reduce fuel consumption and effectively lower operational costs. From the structural point of view, fuel consumption is directly related to the weight of the aircraft, and one way of reducing the weight is by using materials that possess high strength-to-weight properties. Composite materials, which consist of two or more distinct materials or phases on a macroscopic level, offer these properties. For this reason their utilization in the aerospace industry has increased in the recent years and is exemplified by the development of the Boeing 787 Dreamliner. Polymer matrix composite (PMC) materials are a particular type of composite materials commonly used in the aerospace industry. They are comprised of a polymer matrix and reinforcing fibers and can be further characterized based on the fiber architecture: unidirectional, woven or braided. The two latter types fall into the category of textile laminates and, in general, offer more balanced or stable performance than their unidirectional relatives [1-4].

The inhomogeneous and anisotropic nature of PMCs makes it difficult to determine their properties and complicates the design and analysis of components and parts made of PMCs. In particular, uncertainties exist regarding their response to cyclic loading, which is critical for predicting the lifetime of the structure. As the result, components made of PMCs are often overdesigned, hence negating the possible weight-savings. Consequentially, in spite of the weight-saving benefits offered by composites over the more conventional metallic alloys, they are not as widely used as they potentially could be. In order to further expand the applicability of PMCs for aerospace applications, additional experimental efforts are required to gain a better understanding of their behavior during fatigue loading with the aim to clarify the uncertainties.

At the present time, the use of commercially available PMCs is limited to 200°C due to the low glass transition temperature of the matrix [5-10]. Developments of advanced matrix materials have shown the potential to raise this temperature limit to 300°C, hence giving PMCs the edge to compete with metals for applications at elevated temperatures (ET) [11]. In fact, one of the experimental programs currently running at the Facility for Research on Aerospace Materials and Engineered Structures (FRAMES) at Ryerson University is focused on characterization of mechanical properties of a high temperature PMC (carbon/MVK-10), which has prospects to be utilized for jet engine components.

When monitoring mechanical properties of PMCs during cyclic loading, conventional techniques used for strain measurements involving strain gages and extensometers have considerable limitations. Strain gages have a low fatigue strain limit, while extensometers might slip during fast loading rates or frequencies. An attractive alternative, which has gained a lot of interest over the last decade, would be the fiber Bragg grating (FBG) optical sensors [12-18]. These sensors have also shown the potential to be implemented for damage or health monitoring of PMCs, due to their inherit sensitivity to a non-uniform strain field [15-18]. In addition, FBGs can be integrated into components or parts during the manufacturing process and hence can be used to measure the internal strains [13-18]. In fact, numerous FBGs can be embedded into the host structure without weakening it due to their compatibility with common resins and small size.

1.2 Objectives and Scope

The main goal of this thesis is to assess the applicability of FBG sensors for stiffness and damage monitoring of PMCs during fatigue. The resultant deliverable is to formulate recommendations that would facilitate the use of FBGs and increase their effectiveness for these applications. Also, as it was mentioned in the previous section, mechanical testing of an advanced carbon/MVK-10 PMC at ET is soon to commence at FRAMES. It is desired to gain expertise with the utilization of FBGs at ET as well as to evaluate the influence of temperature on mechanical properties and failure mechanisms of PMCs. The knowledge acquired during the span of this thesis will aid with the definition of the test protocol and with the set-up of the apparatus for ET fatigue tests.

This thesis comprises the work done for two experimental projects that encompassed different objectives, materials and procedures but, nonetheless, shared the same intertwining theme. One project focused on fatigue monitoring of on-axis carbon/epoxy woven laminates with embedded FBG sensors. Whereas the other project dealt with application of surface bonded FBGs for monitoring of off-axis carbon/BMI woven laminates at ET (up to 200°C). Since the two projects were characteristically different, separate chapters (4 and 5) are dedicated to them. Also, a clear definition of the scope and motivation of the each project is included in the beginning of these chapters. Similarly, separate sections summarizing the experimental methodologies are written. Moreover, since the focus of the thesis is twofold, two literature review sections were prepared: one for textile PMCs and one for FBG sensors. The overview of the thesis is presented in the next section.

1.3 Overview

Chapter 2 will present the literature review on textile polymer composites. It will discuss the general mechanical properties and failure mechanism of PMCs, and will describe their dependence on time and temperature.

Chapter 3 will review the fundamentals of FBG sensors and the bases for their applicability for damage and stiffness monitoring. It will also discuss the concerns associated with utilization of FBGs for these applications. The main focus of this chapter will be on interpretation of the FBG spectral data for damage monitoring.

Chapter 4 will focus on the experimental work conducted to evaluate the usability of embedded FBGs for stiffness and damage monitoring of on-axis woven laminates. It will explain the motivation and scope of this project, and will describe the experimental set-up and the test methodology.

Chapter 5 will focus on the experimental work conducted to assess the applicability of surface mounted FBGs for damage and stiffness monitoring of off-axis woven PMCs at elevated temperatures. It will also demonstrate the effect of temperature on the fracture mechanisms and material properties. The motivation and the scope of this project will be explained along with the experimental set-up and the test methodology.

Chapter 6 will merge results of the two experimental programs and will propose recommendations regarding utilization of FBGs for stiffness and damage monitoring.

Chapter 7 will draw conclusions based on the results of the experimental investigations that were discussed in Chapters 4 and 5. This chapter will also present the future work.

Chapter 8 will present additional figures pertaining to the experimental work covered in Chapter 4.

Chapter 9 will present additional figures pertaining to the experimental work covered in Chapter 5.

Chapter 10 will present the reference material.

2 Textile Polymer Matrix Composites

2.1 Introduction to Textile PMCs

Polymer matrix composites (PMCs) with fabric reinforcement layers, woven or braided, offer several advantages over the traditional composites with unidirectional laminas [1–4]. The bi-directional reinforcement of textiles gives them balanced in-plane performance, improved out-of plane performance and excellent impact resistance. Textile fabrics are also easier to handle compared to unidirectional-tapes, resulting in a cost-effective fabrication process. In addition, woven and braided fabrics come in a variety of weave patterns (e.g. plain, satin, twill) and braid architectures (braid angles, 2D vs. 3D braiding), allowing further customization of properties. Mechanical properties of woven and braided composites are comparable to those of cross-ply and angle-ply laminates. Nonetheless, textile PMCs exhibit some unique properties that are a direct result of their interweaving or braiding geometry. This chapter, while being primarily based on material properties and failure mechanism of textile composites, will make periodic references to cross-ply and angle-ply unidirectional laminates to further illustrate certain concepts.

2.2 Material Properties

2.2.1 General Stress-Strain Curves

Properties of composite materials result from a combined effect of the properties of the individual constituents, the microstructure or the lay-up of the material, and the type and direction of applied loading. For instance, unidirectional laminates loaded in the longitudinal (fiber) direction possess fiber-dominated properties and exhibit a linear response up to failure. In this thesis “failure” refers to the ultimate failure (i.e. fracture). On the other hand, specimens with off-axis plies become more influenced by the matrix properties as the angle and the number of off-axis plies increase. For instance, Figure 1 shows the stress-strain curves of woven specimens loaded at different (a) off-axis angles and (b) braided specimens with different braid angles [19, 20]. From these figures it is evident that with an increase of the off-axis or braid angle, stiffness and strength reduce significantly, and the stress-strain curve becomes increasingly non-linear. Similar observations were made with other lay-ups of off-axis, angle-ply and quasi-isotropic laminates [1, 2, 5, 21–26]. Due to the apparent non-linearity of the stress strain curve, the elastic modulus is usually calculated from the data in the 0.1-0.3% strain range [20, 24-26].

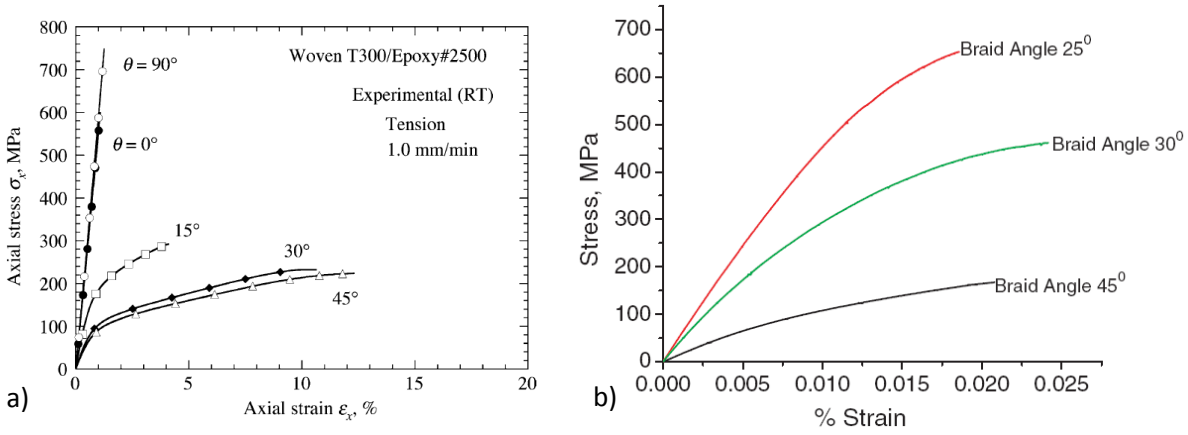

Figure 1: Stress-strain behavior of a) woven specimens with different off-axis angles [19] and b) braided specimens with different braid angles [20].

2.2.2 Fatigue Performance

The onset and evolution of damage during cyclic loading causes material properties to degrade. The common means of assessing fatigue performance of a material is by evaluating the reduction of strength, stiffness and fatigue life with respect to time (or the number of cycles). Analysis of residual strength and fatigue life requires destructive testing, whereas stiffness can be determined by non-destructive techniques, such as strain measurements with FBG sensors. Therefore, stiffness degradation can be monitored during the lifetime of a component and related to its residual fatigue life or structural integrity. For this purpose, an **S-N** curve is frequently employed that shows the relationship between the applied stress and the number of cycles to failure. A typical stiffness degradation curve of a composite material has three stages [6]. During the first stage, significant stiffness loss occurs, but it represents only 10-20% of the entire fatigue life. In the next stage, which accounts for 80-90% of the fatigue life, stiffness gradually decreases at a constant rate. In the last stage, stiffness drops abruptly and final failure occurs.

Moreover, an interesting phenomenon known as strain ratcheting or cyclic creep was reported in a number of papers, Figure 2 [27–29]. It was observed that during the cycling loading of polymers [27] and PMCs [28, 29] as the number of cycles increases, the hysteresis loop continuously shifts in the direction of increasing strain. However, with the progression of fatigue loading, the hysteresis loops become thinner and more linear, and the ratcheting rate decreases. As shown in Figure 2, after a certain number of cycles a stable or saturated ratcheting strain is reached. Furthermore, in the case of off-axis unidirectional laminates, ratcheting is more drastic in transverse and shear directions (Figure 2) when compared to the longitudinal (0°) or loading directions [29].

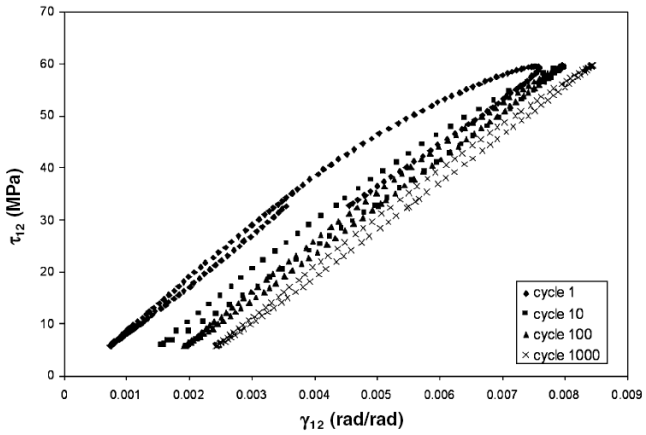

Figure 2: Hysteresis loops of a 10^{o} off-axis PMC specimen in shear [29].

For practical purposes, such as monitoring of stiffness degradation, it is convenient to relate material behavior after **n** number of cycles to the original undamaged state. This can be achieved by applying the concept of fatigue modulus, which was proposed by Hwang *et al.* [28] in the mid 1980's. In Figure 3, the line **nn'** denotes the elastic modulus **E(n)** after **n** cycles, and the line **on'** defines the fatigue modulus **F(n)** after **n** cycles. This concept is easy to implement because it bypasses the non-linearity of the stress-strain curve, which complicates definition of an elastic modulus.

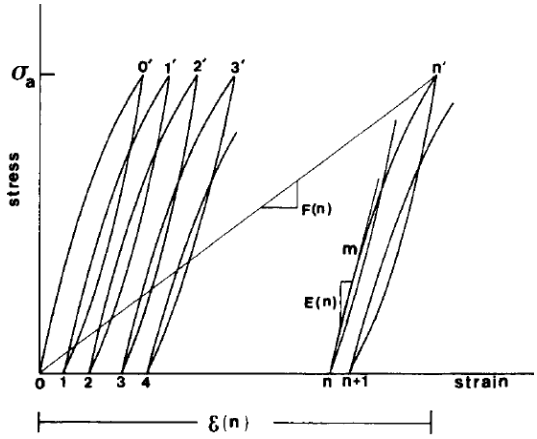

Figure 3: Concept of fatigue modulus [28].

The stress-strain response of polymers is dependent on time and temperature. This behavior is known as viscoelasticity and is also exhibited by polymer matrix composites [30–33]. The following two sections will discuss the influence of temperature and time (e.g. loading rate and frequency) on PMCs.

2.2.3 Time Dependence

The stress-strain response of a viscoelastic material is strongly influenced by the loading rate. For instance, it was shown that at higher strain rates, the hysteresis loop becomes less non-linear [27] and a higher ultimate tensile strength is reached before failure [1, 21, 34]. Similarly, during fatigue loading when higher strain rates are applied, the rate of residual strain accumulation and the resultant stable ratcheting strain are lower [27]. However, higher frequencies might cause self-heating of PMCs [1, 19, 27]. This phenomenon will be discussed in more detail in the section on temperature effect (Section 2.2.4). Moreover, viscoelastic materials are also known to undergo creep, which refers to elongation of a material over time under a constant stress level [11, 27].

The degree of influence of time on the stress-strain response of a PMC depends on how matrix-dominated the particular material is. For example, Branco *et al.* [21] compared the effects of frequency (1.5 Hz vs. 10 Hz) on the fatigue behavior of unidirectional and cross-ply laminates. The S-N curves of the cross-ply laminates had a transition point: fatigue strength increased with a decrease in frequency during high-cycle fatigue, but fatigue strength decreased during low-cycle fatigue. However, in the case of unidirectional specimens, the slope of the S-N curve was unaffected, while the strength reduced with a decrease in frequency [21]. Similarly, experiments conducted by Counts *et al.* [35] showed that bearing fatigue life of quasi-isotopic carbon/polyimide joints was independent of frequency (0.1-10 Hz). Overall, these studies showed that the effect of time has to be taken into account when considering the static and dynamic performance of PMCs, especially with matrix-dominated lay-ups.

2.2.4 Temperature Dependence

The discussion of mechanical properties of PMCs will now be expanded to include the effect of temperature. Earlier tests of unidirectional specimens demonstrated that longitudinal modulus ($\mathbf{E_1}$) is nearly independent of temperature, whereas transverse ($\mathbf{E_2}$) and shear ($\mathbf{G_{12}}$) modulii decrease significantly at temperatures approaching the glass transition temperature (**Tg**) of the polymer, Figure 4 [36, 37]. In the case of longitudinal properties thermal influence is minimal since carbon and glass fibers are not affected by temperatures in the range applicable to PMCs (<350°C). On the other hand, the off-axis properties are matrix-dominated, and the mechanical and failure properties of the matrix are temperature dependent [38]. Similarly, with lay-ups that are more fiber-dominated, such as unidirectional and quasi-isotropic laminates, only a small dependence on temperature was detected [7, 8].

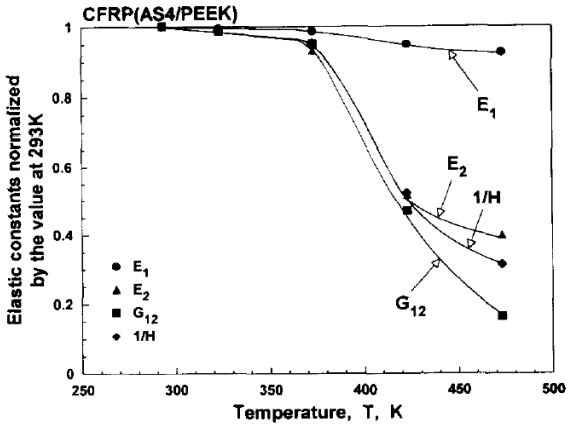

Figure 4: Relationship between elastic constants and temperature [36].

PMCs, especially those that exhibit matrix-dominated properties, experience a reduction of longitudinal stiffness, ultimate strength and fatigue life at elevated temperatures (ET) [21, 34, 38], refer to Figure 5a and b [19]. A more severe degradation occurs at temperatures near the Tg. These degradations occur primarily due to the decrease of shear strength and modulus of the matrix, and the weakening of the fiber-matrix bond [5, 6, 9, 19]. Similarly, at ET a matrix becomes more viscoelastic and properties of a PMC become increasing more time-dependent [11, 30, 37, 39].

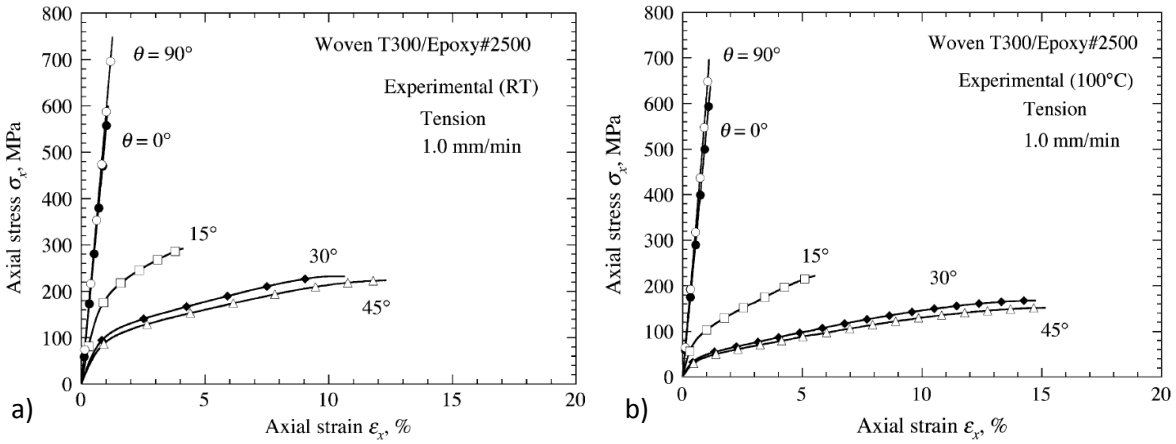

Figure 5: Stress-strain behavior of off-axis woven composites at a) room temperature (RT) and b) 100°C [19].

Furthermore, several authors have noted that PMCs might exhibit self-heating during mechanical loading, and its presence should not be ignored [1, 19, 24-27, 40]. It has been reported that specimens with off-axis fiber bundles (e.g. 30°-45°) tend to generate more heat [24, 25]. To deal with this issue, either forced cooling [24-26] or lower loading rates (or frequencies) are used to mitigate the temperature [1, 27].

2.3 Failure Mechanics

The type of damage commonly observed in textile laminates is transverse cracking, fiber-matrix debonding, and delamination between plies or tows. The general sequence of damage formation in these laminates was described by Khan *et al.* [6] and Lomov *et al*. [4], and is shown in Figure 6:

- transverse matrix cracks initiate in the weft or off-axis bundles and propagate along the fiber;
- as cracks saturate, local debonding and local delamination start at the tow crossover points;
- ply-delamination, fiber-matrix debonding and fiber fracture occur;
- abrupt and catastrophic failure of fiber bundles occurs.

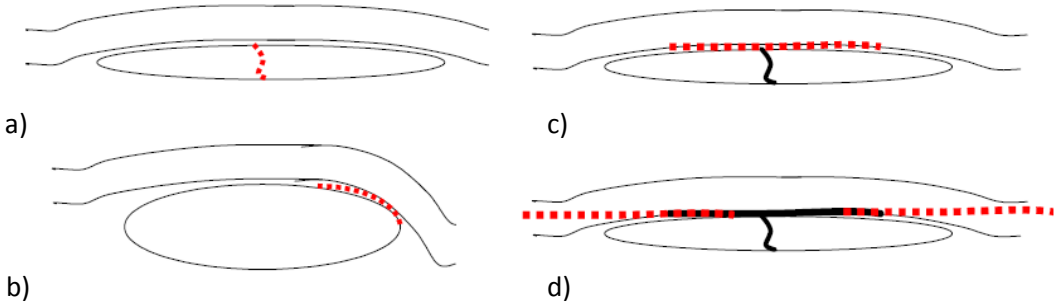

Figure 6: Development of damage in textile PMCs: a) transverse cracks initiate, b) local delamination occurs between yarns, c) delamination originates around transverse cracks and d) finally fiber breakage occurs due to delamination [4].

Transverse microcracks in PMCs are caused by transverse tension and shear strains [4]. These cracks appear to be confined within one yarn and as a result are limited in length and width [1, 4]. As Hansen [1] further explained, the bi-directional form of reinforcement present within the individual plies of textile laminates restrains damage of the weak matrix from developing and manifesting as a dominant failure mode, as is the case with unidirectional laminates. Hence textile laminas are more resilient than unidirectional laminas. Similarly, it was shown by Kobayashi *et al.* [10] that in the cross-ply unidirectional laminates propagation of transverse cracks in the thru-thickness direction is arrested when the crack tips hits the resin rich area between the 0° and 90° plies. However, when two bundles with the same orientation are in contact, cracks can extend between them [4]. Additionally, in the case of woven [0#90] and quasi-isotropic lay-ups, such as $[(45\#\text{-}45)(0\#90)]_{2s}$, matrix cracks first appear in the 90° tows and then in 45° tows [7].

Moreover, it was observed that woven and braided fibers tend to straighten out during axial loading [4, 6]. Additionally, the off-axis fibers tend to rotate towards the loading direction and by that creating an apparent increase in the longitudinal stiffness [19]. The latter point was also confirmed by experimental

and numerical work by Kawai *et al.* [19] on unidirectional off-axis laminates. Also, a number of authors reported the tendency of woven specimens to fail close to the grips due to the presence of a complex stress state [1, 19, 41].

Fatigue failure mechanisms of braided laminates were described in great detail by Huang *et al.* [2]. Three types of specimens were considered, having braid angles of: 10°, 28°, and a combination of 10° and 28°. Analysis of the failure modes suggested that braided laminates are less prone to delamination than their close relatives, the angle-ply laminates. After failure specimens fabricated from laminas of the same braid angle showed no signs of delamination. Also, quasi-isotropic woven laminates tested in static tension by Hansen [1] did not delaminate. However, when laminas had different angles, extensive delamination occurred. Delamination between the 0° and 28° plies was caused by the shear stresses between them that were induced by the difference in the longitudinal stiffness between the plies. However, it was interesting to note that specimens did not fail after delamination, and the separated plies continued to carry the load. Additionally, experiments performed by Tang *et al.* [41] showed that longitudinal stiffness of cross-ply laminates is almost insensitive to the onset and growth of delamination. In the case of the 28° braid angle, specimens fractured perpendicular to the load direction and formed a zig-zag pattern on the surface (Figure 7a). Authors concluded that the main failure mode was fiber breakage that occurred due to the local stress concentrations. Specimens with a 10° braid angle failed due to fiber breakage and fiber-matrix debonding that caused splitting between fibers along the length of a bundle, Figure 7b. An interesting observation was made regarding the specimen with laminas having 10° and 28° braid angles, each lamina type had its own failure mode. Previous studies that analyzed fatigue failure of unidirectional off-axis [22, 23] and woven specimens [4] showed that these types of specimens fail along the fiber direction due to fiber-matrix debonding.

Figure 7: Failure states of braided composites with a) 28° and b) 10° braid angles [2].

The failure phenomenon of textile laminates can be further examined through the work of Kawai *et al.* [19] which investigated the behavior of off-axis woven specimens during tensile loading at different temperatures. Specimens were cut from plain woven carbon/epoxy (Tg=130°C) laminates with

orientation angles of 0°, 15°, 30°, 45° and 90°. The on-axis (0° and 90°) specimens failed close to the end tabs and the fracture surface was perpendicular to the loading direction regardless of the temperature. Similar observations were reached by Kawai *et al.* [22] regarding the fracture surface of the 0° unidirectional specimens. In the case of static loading at room temperature (RT), off-axis specimens failed along the yarn direction, Figure 8a. At 100°C specimens exhibited necking and the fracture morphology was "brushy", Figure 8b. It was also noted that specimens with the 15° off-axis angle demonstrated signs of on-axis and off-axis failure modes that were induced by the transition from fiber-dominated to matrix-dominated failure. Overall, delamination and fiber pull-out were not significant. Fracture morphology of the specimens after fatigue loading was independent of temperature and was similar to fracture at 100°C under static loading, Figure 8b.

a)

b)

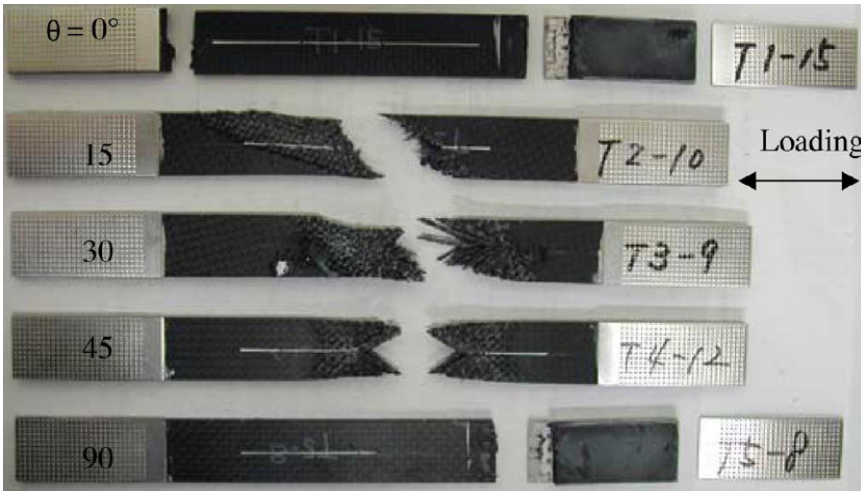

Figure 8: Fracture states of off-axis woven specimens tested in a) static tension at RT and b) static tension at 100°C, and tensile fatigue at RT or 100°C [19].

A particularly interesting “scissoring” damage mechanism of braided specimens was described by Fouinneteau *et al.* [3]. The objective of the study was to investigate the shear mechanism that drives deformation of braided PMCs during axial loading. Authors compared the response of carbon/epoxy and glass/epoxy specimens with a 45° braid angle. During tensile loading carbon and glass based composites show distinctively different responses. The glass specimens, being more ductile, stretched more and developed less shear stress than the carbon specimens. Carbon specimens underwent significant necking, which was distributed along the full length of the specimen. Necking was facilitated by the scissoring mechanism that occurred when the fiber-matrix interface failed, and the two constituents began to separate, hence allowing tows to re-align themselves towards the loading direction, Figure 9. The separation of the two constituents was particularly evident at the sites of tow overlap on the surface of the specimen where the matrix turned whiter.

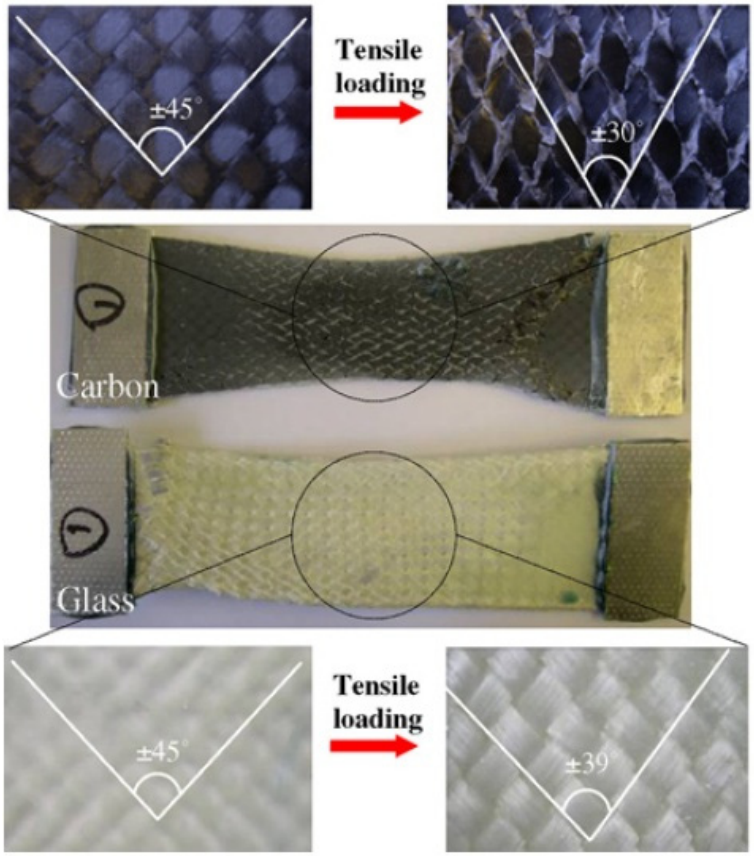

Figure 9: Scissoring mechanism of braided composites [3].

2.3.1 Temperature Effect

As previously mentioned, PMCs inherit their temperature dependence from the matrix material. Typically thermoplastics such as PEEK polyimide are ductile, whereas thermosets such as PMR polyimide and BMI resins are brittle [38]. Overall, brittle and ductile materials have characteristically different failure surfaces. At low temperatures microcracking of the matrix is induced by residual stresses, which are caused by the difference in the coefficient of thermal expansion between the fibers and the matrix [42]. As cracks grow and coalescence, hackle marks are formed on the surface and are considered to be characteristic of brittle fracture [22], see Figure 10a. However, as the temperature is increased, the matrix becomes more ductile and the strength of the fiber-matrix interface weakens. Also as noted by Kobayashi *et al.* [10] crack growth is impeded due to the softening of the matrix. As a result, failure is dominated by the debonding of the fiber and the matrix and leads to a relatively clean or smooth fracture surface void of any hackle marks [22], as shown in Figure 10b.

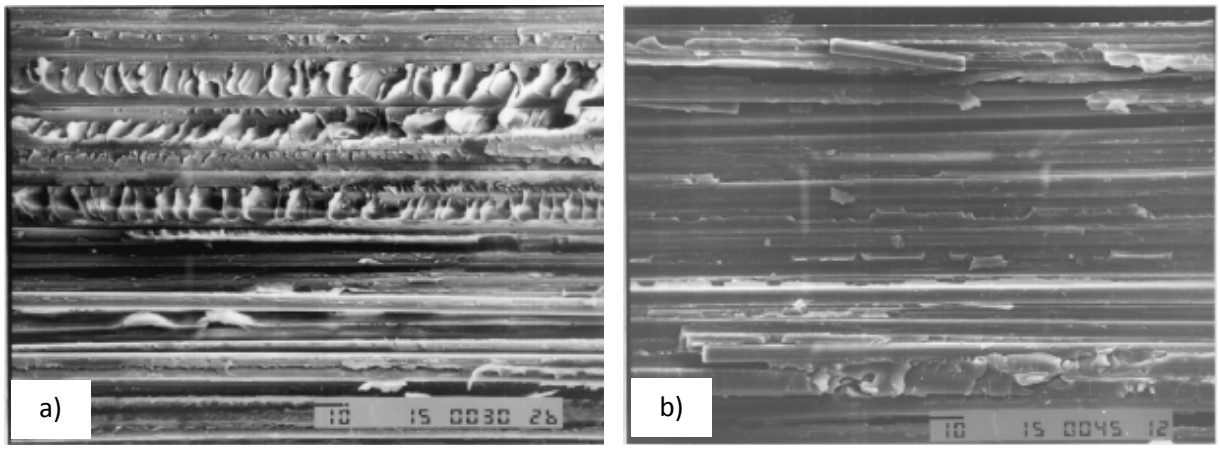

Figure 10: Fracture characteristics of a) brittle fracture with hackle marks and b) ductile fracture with a relatively smooth surface [22].

Experiments also showed that when subjected to thermal cycling or aging at elevated temperatures PMCs develop transverse microcracks [11, 43]. Shimokawa *et al.* [43] noted that the quantity of microcracks strongly depends on the matrix material. Additional tests were performed by Ahci *et al.* [11] to evaluate the effect of temperature on the growth of transverse matrix cracks in woven carbon/polyimide specimens. In this experimental program specimens were pre-damaged during fatigue and then held at ET for various periods of time. Results indicated that temperature has a negligible effect on crack growth. For further information on the effect of temperatures on PMCs, the reader is referred to [11, 22, 38, 42, 44].

2.4 Concluding Remarks

This chapter reviewed the stress-strain response and failure mechanisms of textile laminates. Overall, the behavior and fracture of woven and braided PMCs is similar to that of cross-ply and angle-ply laminates. However, interweaving or braiding architecture of the reinforcing fibers makes textile composites more resilient to transverse matrix cracking and inter-ply delamination and gives rise to interesting failure morphologies. Time and temperature have an influence on mechanical properties and fracture mechanics of PMCs, and have to be considered when characterizing the material.

3 Fiber Bragg Grating Sensors

3.1 Fundamentals of Fiber Bragg Grating Sensors

Prior to introducing the working principles of fiber Bragg gratings (FBGs), it is essential to have an understanding of the anatomy of an optical fiber (OF), Figure 11a. Light travels through the core section of the fiber by employing the principle of total internal reflection. This occurs because the core and the cladding are made from different types of glass and have different indices of refraction. The buffer, which is an outer part of an OF, serves as a protective layer since the bare fiber (cladding and core) is very fragile. It is usually made from polyacrylate or polyimide coating. An important property of this coating is its compatibility with common resins, a vital factor for embedding purposes.

Silica glass is photosensitive, and its index of refraction increases when it is subjected to intense laser radiation [45]. This property of glass can be utilized to write or create a periodic variation of the index of refraction in the core of an OF by exposing it to an ultraviolet-laser light. A common method is a phase masking technique. The resultant pattern acts as a stop-band filter to reflect a narrow band of wavelengths close to the Bragg wavelength $\boldsymbol{\lambda_B}$ while transmitting other wavelengths [46]. This coined the term, fiber Bragg grating. This principle is illustrated in Figure 11b.

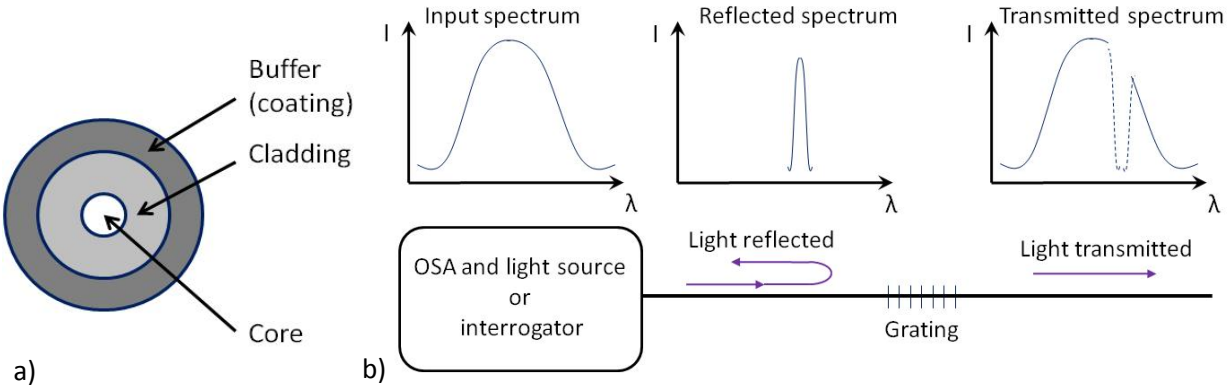

Figure 11: Schematic diagram of a) the anatomy of an optical fiber and b) the reflected and transmitted FBGs spectra.

There are different types of FBGs. Uniform FBGs, which will be the focus of further discussion, are most commonly used for damage, strain and temperature monitoring. The particular Bragg wavelength, to which an FBG is sensitive, is influenced by the index of refraction $\mathbf{n_{eff}}$ and the period of the grating $\boldsymbol{\Lambda}$, as shown in Eq. 1 [47]. The term uniform implies a constant grating period.

$$\lambda_B = 2n_{eff}\Lambda \qquad (1)$$

From Eq. 1 it is evident that a change in the index of refraction or period will lead to a shift of the Bragg wavelength. This relation can be further expanded to account for the effect of strain, temperature and fiber properties of the Bragg wavelength, as described by Eq. 2 [47],

$$\Delta\lambda_B = 2n_{eff}\Lambda\left[\left\{1-\left(\frac{n_{eff}^2}{2}\right)\left(P_{12}-\upsilon\left(P_{11}+P_{12}\right)\right)\right\}\varepsilon+\left\{\alpha+\frac{\left(\frac{dn_{eff}}{dT}\right)}{n_{eff}}\right\}\Delta T\right] \quad (2)$$

where $\mathbf{P_{ij}}$ is the Pockel's coefficient of the stress-optic tensor, **ν** is the Poisson's ratio of an OF, **ε** is the applied strain, **α** is the coefficient of thermal expansion of an OF, **T** is the temperature and **ΔT** is the change of temperature.

Equation 2 can be divided into the two parts: strain load influence and temperature influence. The FBG strain response arises due to both the physical elongation of the sensor (change of a grating period) and the changes in its properties due to photoelastic effects. The thermal response arises due to the thermal expansion of the OF and the temperature dependence of the $\mathbf{n_{eff}}$. To simplify the expression of Eq. 2, factor **f** (Eq. 3) can be introduced by combining all the photoelastic constants. Based on the typical properties of an OF, as were given by Tao *et al.* [48], the factor **f** has an approximate value of 0.8. Under constant temperature conditions Eq. 2 can be transformed into a strain-wavelength relationship, as presented by Eq. 4. Alternatively, under constant strain conditions, the temperature-wavelength expression takes the form of Eq. 5. The more frequently used form of this expression is Eq. 6, where $\mathbf{K_T}$ is the experimentally measured coefficient of thermal sensitivity of the FBG [49].

$$f = 1-\left(\frac{n_{eff}^2}{2}\right)*\left(P_{12}-\upsilon\left(P_{11}+P_{12}\right)\right) \quad (3)$$

$$\varepsilon = \frac{\Delta\lambda_B}{f\lambda_B} = \frac{1}{0.8}\frac{\Delta\lambda_B}{\lambda_B} \quad (4)$$

$$\Delta\lambda_B = \lambda_B\left[\alpha+\frac{dn_{eff}/dT}{n_{eff}}\right]\Delta T \quad (5)$$

$$\frac{\Delta\lambda_B}{\lambda_B} = K_T\Delta T \quad (6)$$

3.2 Concerns with FBGs

This section discusses certain concerns regarding the use of FBGs and the current approaches or best practices used to overcome them. The three main concerns are: the effect of the embedded FBGs on the host material, the proper bonding of the surface mounted FBGs, and the ability of FBGs to withstand cyclic loading.

3.2.1 Embedded FBGs

The use of embedded FBGs is advantageous as they can be integrated into the component during the manufacturing process and can provide useful information about the internal strains in the material. The early works involving embedded FBGs, or fiber optic sensors, were geared towards the analysis of its effect on the microstructure of the host material and its mechanical properties. Detailed reviews and summaries of such works are available in open literature [50]. Overall, studies have shown that the effects of embedded OFs on the host material vary significantly depending on the material type, loading, lay-up, and OF configuration [51]. The worst material property degradation is achieved when an OF is embedded perpendicular to the load carrying fibers and the loading direction. In fact, most researches that have employed embedded FBGs for strain monitoring of composites (except for woven or braided) embedded the OF parallel to the adjacent unidirectional fibers and the loading direction [52]. This placement 'shields' the OF from matrix cracking and minimizes its effect on the composite [52].

However, this may give rise to a new problem of embedding fiber optic sensors in woven or braided materials. Several researchers explored the option of co-braiding the optical fiber into the braided composite directly during manufacturing [53, 54]. FBGs have also been embedded in between the woven or braided plies [53, 54, 55]. However, no papers were found that addressed degradation of mechanical properties of the specimens, and the signal quality and longevity of the optical sensor.

Another parameter to consider is the coating of the fiber. As Vieira *et al*. [56] commented, it is generally accepted that polyimide coating offers better adhesion and higher interfacial strength compared to the standard acrylate coating. In fact, the combination of thickness and stiffness inherit to the polyimide coating used for optical fibers helps lower stress concentrations around the cladding [52]. Furthermore, polyimide coating is highly compatible with epoxies and other polymer resins, and can withstand temperatures up to 350^{o}C (vs. acrylate 170^{o}C) [52].

3.2.2 Surface Mounted FBGs

In the past, researchers have successfully used surface mounted FBGs for strain measurements during static and fatigue tests [12, 13]. FBGs are a particularly attractive alternative to strain gages, which have a significantly lower fatigue limit (2,000-3000 με) than OFs have (10,000 με). Also, they eliminate problems associated with embedding FBGs, especially for complex parts where the manufacturing process might introduce more complications.

Overall, when using surface mounted FBGs it is critical to achieve good strain transfer through the adhesive layer and a strong bond to minimize the chances of debonding. De Baere *et al.* [13] reported a surface preparation method similar to that required for a strain gage lay-out: surface cleaning, abrasion, conditioning, neutralizing, plus pre-tensioning to avoid buckling. In this study FBGs were bonded to a carbon woven laminate, and subjected to a fatigue loading for 500,000 cycles (5,000 με, 5 Hz and 50% of ultimate tensile strength).

A surface mounted FBG would sense a lower strain than that seen by the substrate due to the strain transmission loss through the bonding layer. This loss is small when the substrate is thick and stiff in comparison to the bonding layer and the FBG [57]. A thorough investigation of the influence of the adhesives layer (its thickness) on the FBG strain-transferring efficiency was presented in the paper by Malik *et al.* [58]. They varied the thickness of the adhesive layer (20-800 μm) used for bonding an FBG to an aluminum dog-bone, while using spacers to achieve a specific thickness. Refer to Figure 12a and b to see the micrographs that show different thicknesses of the adhesive layer. A comparison between the strain gage and FBG results (as shown in Figure 13) clearly showed a loss in transmission (reduction in strain values) for adhesive thicknesses above 600 μm.

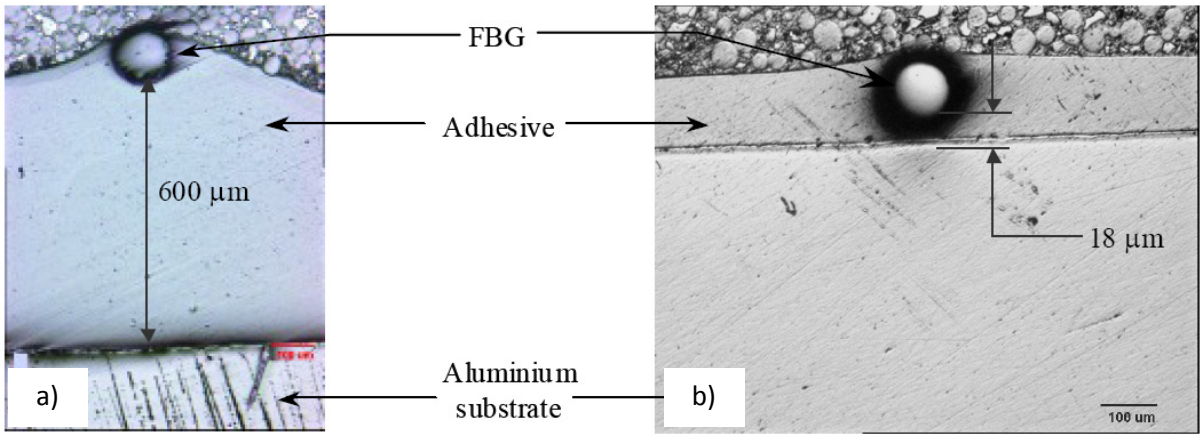

Figure 12: Micrographs of FBGs bonded with adhesives of different thickness a) 600 μm and b) 18 μm [58].

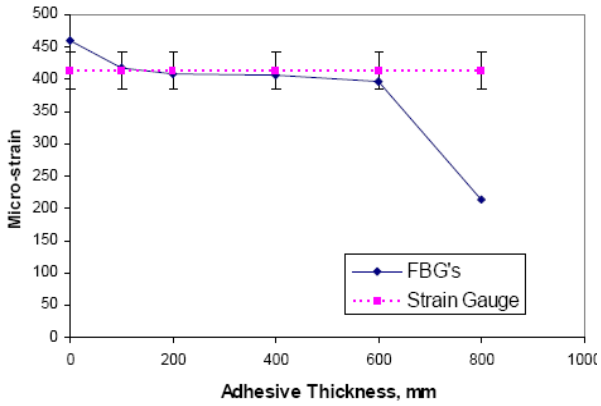

Figure 13: Comparison of strain values measured by FBG sensors and strain gages at varying adhesive thickness [58].

3.2.3 Lifetime of FBGs

The primary focus of this report is on the utilization of FBGs for strain, stiffness and damage monitoring during mechanical testing. However, it is also important to consider the mechanical performance of the sensors themselves. When it comes to high strain fatigue, FBGs significantly outlast strain gages. Thus far, a number of studies showed that FBGs exhibit good durability under cyclic loading [13, 14, 57]. For instance, Matthewson *et al.* [59] studied fatigue performance of the optical fibers (fused silica OF and acrylate coating) in bending at frequencies ranging from 0-100 Hz. They concluded that frequency of the cyclic loading has a minimal effect on the optical fiber in the specified stress range (up to the max load of 5050 MPa). Furthermore, Kosaka *et al*. [14] tested carbon fiber and glass fiber textile PMC specimens with embedded FBGs. Fatigue tests at 0.2 Hz lasted for 100,000 cycles, and the strain readings from FBGs matched those of strain gages. Additionally, in the study conducted by De Baere *et al.* [13], surface bonded FBGs lasted for 500,000 cycles. In the two latter studies, the fatigued specimens did not show any significant damage or stiffness degradation.

Additionally, Tao *et al.* [55] conducted 3-point bending tests on plain-woven glass laminates with an embedded FBG and concluded that: when the variation of temperature is less than 10°C and the measured strain is greater than 0.1%, the temperature effect on the measurement is negligible.

3.3 Damage Monitoring with FBGs

When an FBG is exposed to a non-uniform strain field, its spectrum will become distorted. This distortion hinders strain measurement capabilities of the FBG as it becomes difficult to detect the Bragg wavelength. Conversely, this property enables FBGs to detect damage since presence of damage creates a non-uniform strain field. This section will discuss the sensitivity of an FBG to damage formation with respect to different strain fields, grating lengths, and sensor locations and will review the direct applications of FBGs for damage monitoring.

3.3.1 Sensitivity of FBGs to Non-Uniform Strain

To illustrate the sensitivity of FBGs to a non-uniform strain distribution, the reader is referred to the numerical study performed by Ling *et al*. [60]. In this study FBG reflected spectra were simulated for cycling loading under uniform, linear and quadratic strain distributions. Results presented in Figure 14a-c, show that the shape (or its distortion) and the reflectivity of the FBG are all strongly dependent on the strain gradient.

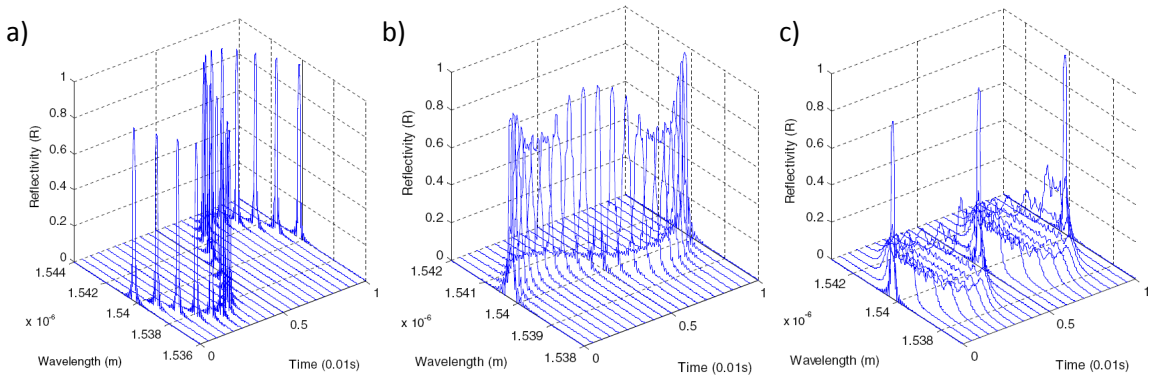

Figure 14: Comparison between the resultant FBG spectra subjected to a) uniform strain gradient, b) linear small strain gradient and c) linear large strain gradient during cyclic loading [60].

When it comes to the presence of damage in a material, the strain gradient is directly related to its position and location with respect to the damage epicenter. The study by Shin *et al.* [61] examined and compared the ability of FBGs embedded at four different locations to sense fatigue damage, which originated at the circular hole in the center of a quasi-isotropic laminate. It was observed that when damage had 'reached' the FBG, its loading spectra widened and the intensity of the signal decreased. It was also observed that the FBG closest to the open-hole chirped more and earlier on during the test than the other FBGs since it was exposed to a higher strain field. In fact, spectrum of the FBG placed the

farthest away from the hole did not chirp during the test. Hence the position of the FBG is extremely important when it comes to damage monitoring.

Moreover, the ability of embedded FBGs to detect delamination and their sensitivity to it was further examined by Ling *et al.* [62, 63]. The earlier study [62] aimed to characterize the response of the FBG loading spectra to damage in terms of the different thru-thickness locations of delamination. The grating was positioned such that the tip of the delamination occurred at the center of the grating. The specimens were statically loaded in 3-point bending, and the loading spectra were captured with an optical spectrum analyzer (OSA). Results showed that the FBG spectra remained essentially unchanged when the site of damage was far away (Figure 15a), and it became significantly distorted when the site of damage was nearby (Figure 15b). This further highlights the sensitivity of the FBG spectra to the location of damage.

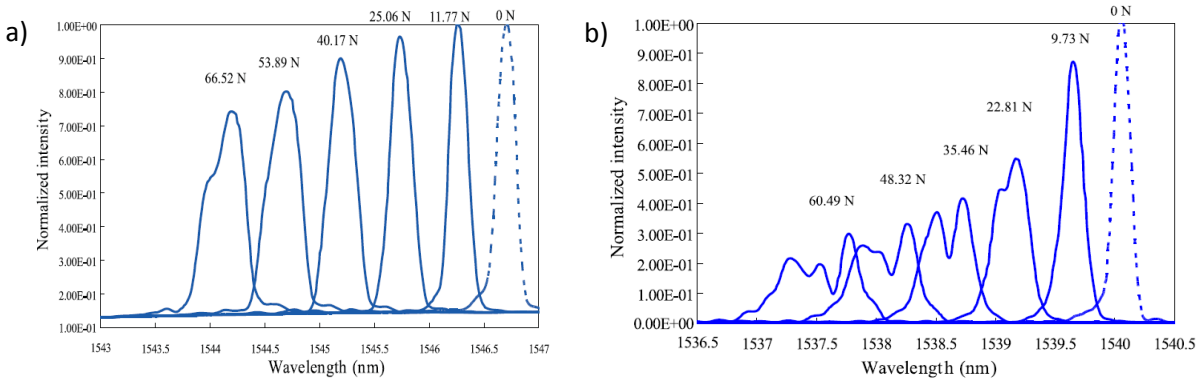

Figure 15: Response of an FBG when the site of damage is a) far from and b) close to the sensor [62].

Additionally, the influence of the grating length on the sensitivity of FBGs to a non-uniform strain field was discussed in the paper by Peters *et al.* [64]. FBGs of two different lengths (1.5 mm and 10 mm) were embedded into an epoxy specimen at different distances from the tip of the notch, which effectively created the non-uniform strain. It was found that when FBGs were sufficiently far from the notch their strain readings were identical regardless of the length of the grating. However, in the vicinity of the notch (<3 mm) signals of the 1.5 mm grating and the 10 mm grating became distinctively different. In addition, the spectrum of the 10 mm grating became chirped, whereas the spectrum of the 1.5 mm grating remained as a single pick. Thus the 1.5 mm grating was small enough to stay unaffected by the strain field; in other words, strain was uniform with respect to the scale of the gage length. Hence it can be concluded that short gratings measure strains at a single point and might not detect crack formation that occurs beyond their length. Moreover, long gratings provide strain measurements of a broader area and are more sensitive to strain non-uniformity caused by cracking. Hence long gratings are more

suitable for qualitative crack monitoring, but their ability to measure strain might be impaired due to strain non-uniformities.

Peters *et al.* [64] further noted that when an FBG is embedded, its analysis is further complicated due to the heterogeneity of the host material. The spectrum might become chirped due to inherent microstructural strain variations present in the material even in the absence of actual damage. An example of this is in the paper by Güemes *et al.* [65] that showed that surface mounted FBGs measured a 10% difference in strain values between warp and weft fibers of a woven material. Hence material non-homogeneity has to be considered when choosing the length of a grating.

Kosaka *et al.* [66] discussed the ability of FBGs to measure strain accurately in the presence of damage (i.e. non-uniform strain field). In this study FBGs were embedded into a flat braided PMC. Static tensile loading was applied on the specimen, and the strain levels were monitored with an FBG and a strain gage. It was found that the two sensors agreed well up to 0.8% strain, but the signal from the FBG became discontinuous above this strain level. By further considering the FBG spectra recorded at different strain levels, it was evident that the sensor detected a varying strain distribution due to the formation of damage and as a result became chirped. Hence chirping signals the onset of damage but complicates strain analysis of the FBG data.

3.3.2 Damage Monitoring via FBG Spectral Analysis

The previous section discussed the sensitivity of FBGs to the presence of damage, and this can provide useful insider information, especially with an embedded FBG, regarding the damaged state of the material. Articles that will be reviewed in this section were selected with the aim to better illustrate to the reader the type of changes that FBG spectra might undergo during damage initiation, growth and possibly saturation. Also, certain differences between the types of chirping caused by transverse cracking and delamination will be highlighted. The author found these articles especially helpful when interpreting spectra data during the course of her thesis. Additional articles on the subject are included in the reference section [67–77].

Takeda *et al*. [15] applied embedded FBGs to monitor delamination in cross-ply laminates subjected to a 4-point flexural static loading. As damage initiated, the presence of cracking resulted in a severely chirped spectrum (Figure 16a), whereas delamination led to a much ‘cleaner’ deformed spectrum (Figure 16b). It is also interesting to note that once delamination became larger than the length of the grating, the spectrum was restored to its original ‘clean’ single peak, Figure 16c. They further noted that

with the onset of delamination, the spectrum split into two peaks representing the bonded and the delaminated regions. Also, the relative intensity of the two peaks changed as delamination increased. Hence the peak that corresponded to the delaminated portion of the FBG started with a low intensity and significantly increased in intensity as delamination had propagated.

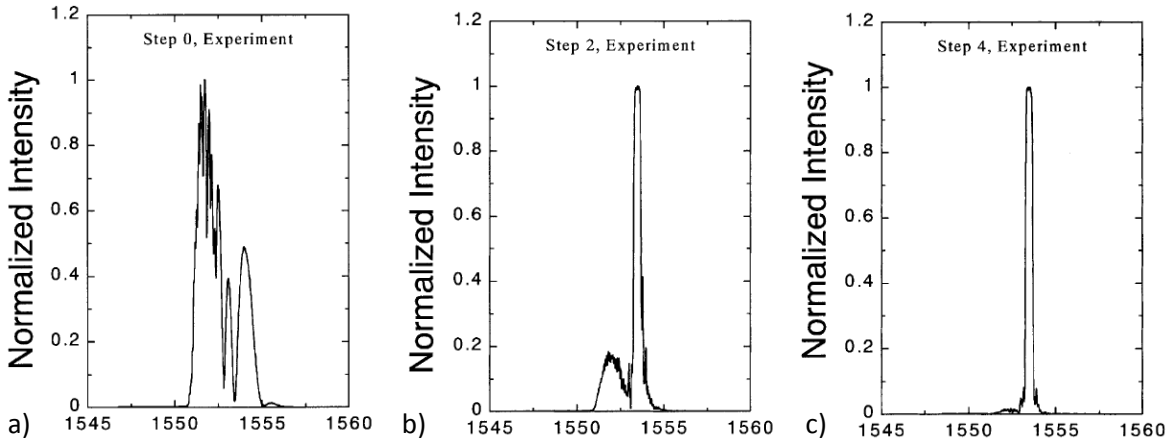

Figure 16: FBG spectra recorded when a) transverse crack had formed, b) delamination initiated and c) delamination became larger than the length of the grating [15].

Moreover, Takeda *et al.* [16] demonstrated the ability of an FBG embedded into a composite repair patch to monitor debonding of the patch. In this study [17] a clear differentiation was made between the different spectral changes characteristic to the onset and the progression of the different failure mechanism (cracking, debonding). Figure 17**,** illustrates how the presence of transverse cracks influences the strain distribution in the vicinity of the grating and shows the resultant chirped spectrum. On the other hand, debonding (or delamination) has a more pronounced effect on the spectrum, causing the spectrum to split into two distinctive peaks, each representing the bonded and the debonded regions. Takeda *et al.* [16] also noted that it was possible to define a relationship between the length of the debonded region and the intensities of the two peaks ($\mathbf{I_A/I_B}$), where **B** corresponds to bonded and **A** to debonded areas. Figure 18, shows the influence of applied loading on the spectral shift; two possible locations of the debonded region along the length of the grating are considered.

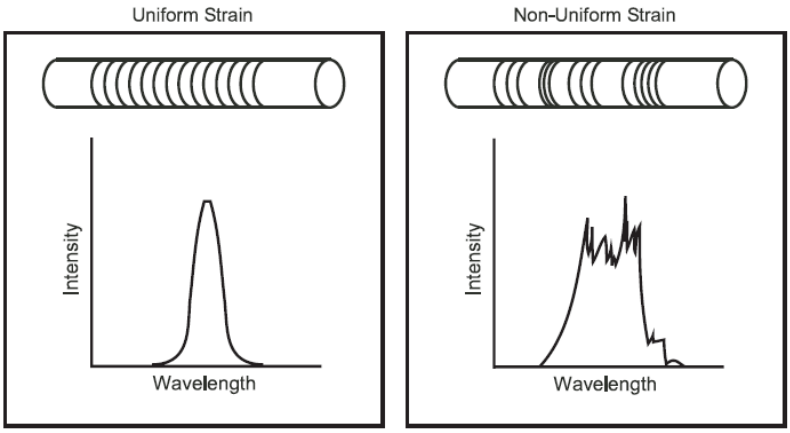

Figure 17: Influence of a non-uniform strain field on the FBG spectrum [16].

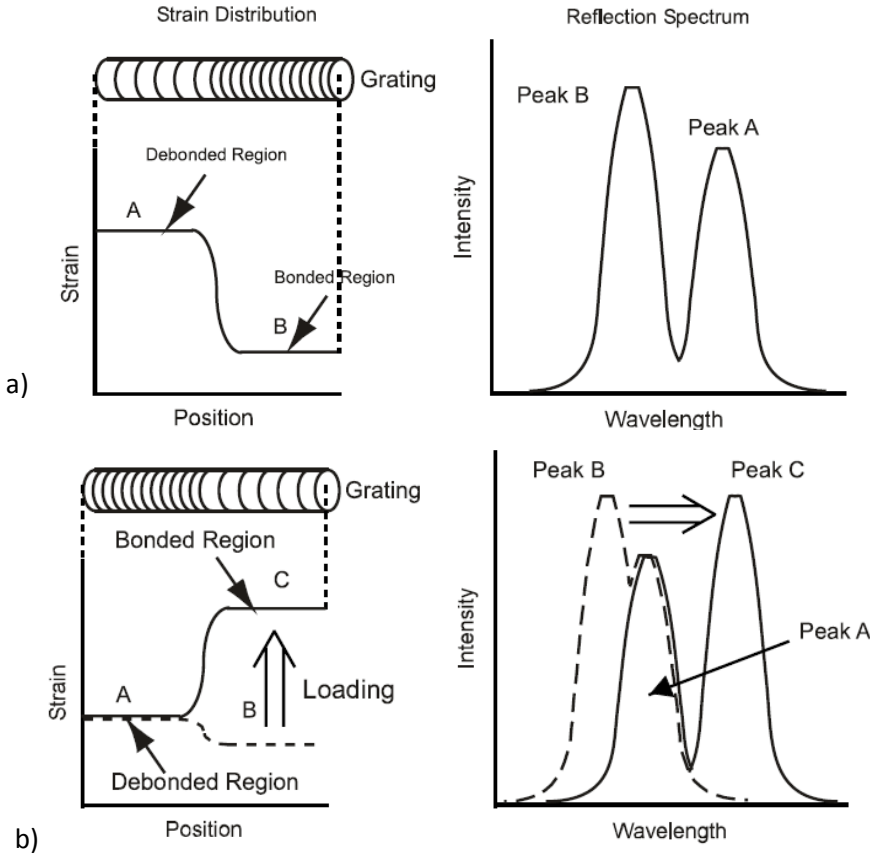

Figure 18: Influence of a) debonding or delamination and b) applied loading on the FBG spectrum [16].

The discussion of delamination monitoring would not be complete without considering the possibility of the FBG starting to debonding. Kadoya *et al.* [17] reported debonding of an embedded FBG during cyclic loading of a holed CFRP laminate. Based on the FBG spectral analysis it was noted that after 1,000 cycles the FBG spectrum chirped and widened (Figure 19a), but after 10,000 it regained its original shape (single narrow peak, Figure 19b). These results suggested that the FBGs had debonded. Knowledge of

the debonding time is important as it directly impacts the available utilization time of the FBG for damage monitoring.

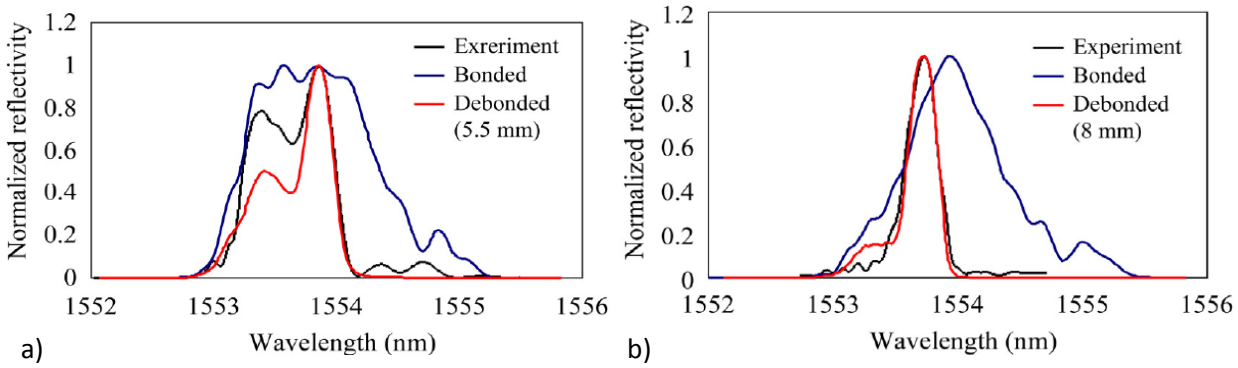

Figure 19: Comparison of the reflected spectra between the experiment and the simulation (bonded vs. debonded) after a) 1,000 cycles and b) 10,000 cycles [17].

The discussion can be further continued by touching upon the application of embedded FBGs to monitor transverse cracks during tensile testing of cross-ply carbon laminates. The resultant FBG response to the initiation and growth of transverse cracks is presented in Figure 20. Figure 20 shows that with an increase in the crack density (point B), the spectrum became distorted: intensity decreased, additional peaks appeared and the spectrum broadened. However, as the crack density came close to saturation (point D), the spectrum was restored to a narrow single peak. Takeda [18] explained this observation by stating that presence of cracks (small density) had created a non-uniform strain field that led to a distortion of the FBG spectrum. However, as the crack density approached saturation, the distance between the two neighboring cracks decreased, thus reducing the strain variation and causing the spectral shape to regain its original (pre-damaged) single narrow peak.

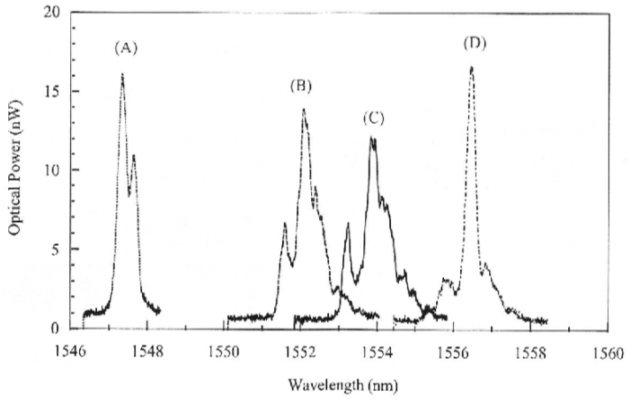

Figure 20: FBG spectra recorded at different tensile strains (and crack densities) [18].

3.4 Concluding Remarks

This chapter reviewed the working principles of FBG sensors, identified possible concerns with their utilization, and discussed their sensitivity to damage development. FBGs are sensitive to strain and strain gradients present in the material and have been successfully utilized for strain and damage monitoring [12-18, 52-55, 66-76]. While their sensitivity to strain non-linearity gives them the ability to detect and monitor damage, it also hinders their ability to provide a clear strain measurement. Hence the length of an FBG and its location with respect to damage prone area, have to be considered in order to achieve optimal strain-field sensitivity. Moreover, when utilizing the surface mounted FBGs care should be taken when bonding the OF in order to ensure proper strain transfer through the adhesive layer. In the case of embedded FBGs, location of an OF has to be carefully chosen in order to minimize the intrusive effect of an OF on the mechanical properties of the host material and to limit the possibility of an FBG failure due to OF breakage.

4 Fatigue Monitoring at Room Temperature

4.1 Motivation and Objectives

An interesting potential application of fiber Bragg grating (FBG) sensors is for the in-service structural health monitoring of aero-structures. Further development of this technology would reduce the time and cost associated with downtime needed for structural inspections. Thus far, embedded FBG sensors have been successfully applied to damage and stiffness monitoring of composite laminates [67–76]. The common methodology for embedding an OF is to orient it in the loading direction and place it parallel to the adjacent reinforcing fibers [0°]. For damage monitoring of angle-ply laminates, the OF is usually embedded close to the interface between the 0° and off-axis laminas. Such positioning effectively minimizes the intrusive effect of the OF on the host material and reduces the chances of the OF being broken during damage propagation. At the same time the FBG remains sensitive to damage that usually manifests in the form of transverse matrix cracks in the off-axis layers and delamination at the interface. However, this embedding configuration is essentially impossible to achieve with textile laminates.

Previous work by De Baere *et al.* [13] showed that FBGs, which were embedded into or surface mounted onto carbon/epoxy woven laminates, could last for at least 500,000 cycles at strain levels of approximately 5,500 με. However, specimens experienced minimal damage formation and stiffness degradation. Hence the aim of this study is to test FBGs embedded into PMCs that develop noticeable fatigue damage in order to assess the continued integrity of the sensor, and its ability to monitor stiffness degradation and damage evolution.

4.2 Experimental Set-Up

4.2.1 Specimens

Specimens under review were manufactured as a part of the project that was performed in collaboration between Ryerson University and Kyoto Institute of Technology and was aimed at investigating embedding methods for fiber optic sensors. Specimens were manufactured by a wet hand lay-up method, which is a basic technique usually employed during early stages of PMC development. During this process dry fabric is impregnated by pouring a desired amount of resin over it and using a hand roller to evenly distribute resin and eliminate voids. The resultant laminates were composed of two layers of plain carbon woven fabric (T300, TORAY Co., Ltd.) oriented in [0#90] direction and

vinylester resin (RIPOXY R806, Showa Highpolymer Co., Ltd.). During the fabric lay-up, an optical fiber with three FBGs was placed in between the two layers and oriented in the longitudinal [0°] direction. The specimen dimensions and the positioning of the OF and FBGs are illustrated in Figure 21a. It is also noteworthy that the OF was loosely affixed to the woven fabric; hence it could move during the manufacturing process. Further information on the manufacturing process can be found in the MASc thesis prepared by Kolubinski [77].

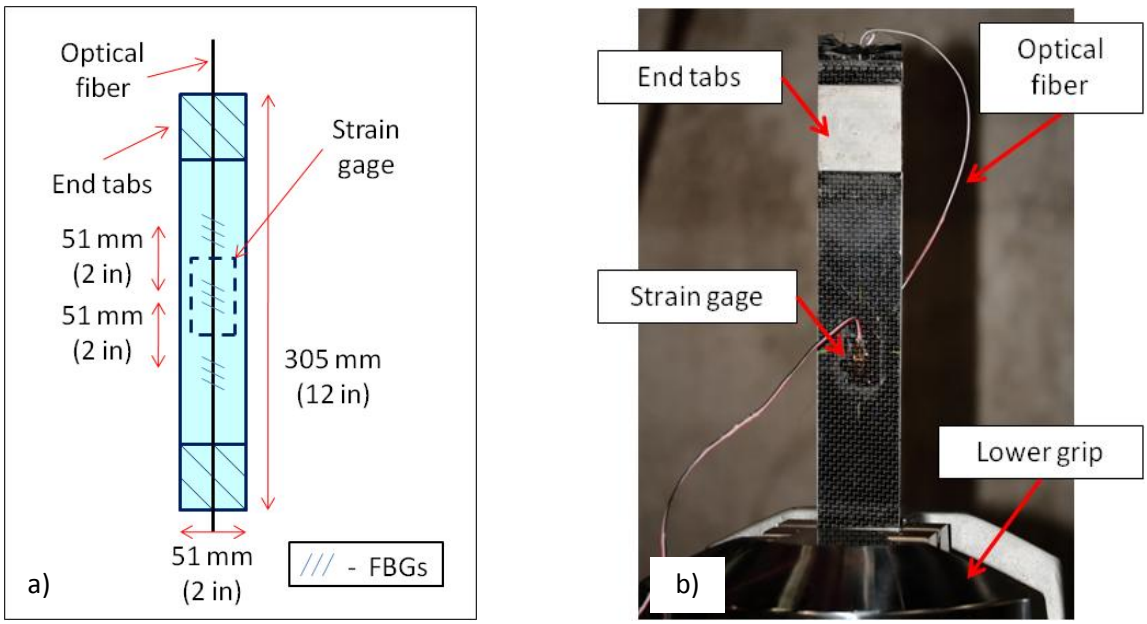

Figure 21: Images illustrating a) the dimensions of the specimens and positioning of the OF and FBGs, and b) the prepared specimen in the grips.

Fiber optic sensors were fabricated at the Fiber Optic Communication and Sensing Laboratory at Ryerson University. FBGs were written on a SMF-28 fiber with polyacrylate coating (Ø 250 µm) by using a phase mask method. A more detailed description of the method can be found in the paper by Lu *et al.* [78]. Once the gratings were written, they were coated with protective polyimide coating (Ø 160 µm) and annealed at 150°C for 15 hours to ensure their long-term stability. Gratings were 3 mm in length, had wavelengths in the range of 1535-1555 nm and were written 51 mm (2 in) apart.

Also, a strain gage (EA-06-250AE-350, Vishay) was used to validate FBG strain measurement. It was bonded to the center of the specimen using instant adhesive (Loctite 496), as shown in Figure 21a. To ensure proper adhesion, the surface of the specimen was degreased, wet abraded (400 grid), conditioned, and neutralized. Prior to testing, aluminum end tabs 51 x 51 mm (2 x 2 in) were bonded to the specimens using two-part epoxy (Araldite 12). Figure 21b shows the prepared specimen in the grips.

4.2.2 Test Protocol

All tests were conducted at Ryerson University at the Facility for Research on Aerospace Materials and Engineered Structures (FRAMES) using an MTS 322 test frame, MTS 647 hydraulic wedge grips, and MTS FlexTest GT/Teststar IIm controller and data acquisition unit. In order to monitor stiffness degradation and capture damage evolution, interrupted fatigue tests were performed in combination with static tests. Data recorded during fatigue tests was used to assess the usability of FBGs for real-time health monitoring, while data from the static tests was used to measure specimen stiffness degradation during fatigue. Specimens were tested at different strain levels, which are summarized in (Table 1).

Table 1: Summary of the specimens tested and the corresponding applied fatigue loads and initial strain levels (prior to stiffness degradation).

Specimen	Max Load Level (% UTS)	Fatigue Loads (N [lbs])	Initial Strain Levels (με)
Woven [(0#90)/FO/(0#90)]	50	F_{min} = 1,645 [370] F_{max} = 16,450 [3700]	4,800
	60	F_{min} = 1,960 [440] F_{max} = 19,600 [4400]	5,750
	70	F_{min} = 2,310 [520] F_{max} = 23,100 [5200]	6,750

Fatigue tests were performed under force control with a sinusoidal waveform, a stress ration R = 0.1 and a frequency of 5Hz. They were run in blocks of 1,000 or 5,000 cycles in the early stages of fatigue (<50,000) in order to adequately capture the initial stiffness drop (to be discussed in Section 4.5). During the later stages of fatigue, since stiffness degradation was subtle and did not required frequent monitoring, tests were run in sets of 50,000-100,000 cycles. During cyclic tests FBG wavelength and force-displacement data were recorded with the Micron Optics Si425 interrogator and the linear voltage differential transducer (LVDT), respectively.

Two types of static tests were performed in between the fatigue intervals. First, a quasi-static test was run in displacement control, and data was recorded with the interrogator and the LVDT. Then specimens were statically loaded to different load levels (about five or seven) up to the maximum cyclic stress, and while the force was kept constant, the FBG spectra were recorded with the Ando A66331 optical spectrum analyzer (OSA). Figure 22 illustrates the experimental set-up used with (a) the interrogator and (b) the OSA. During initial static tests (prior to fatigue) strain data was also recorded with a surface mounted strain gage by the Vishay P3 strain gage indicator. The strain gage data was used to provide an initial correlation between strain measurements of a strain gage and an FBG.

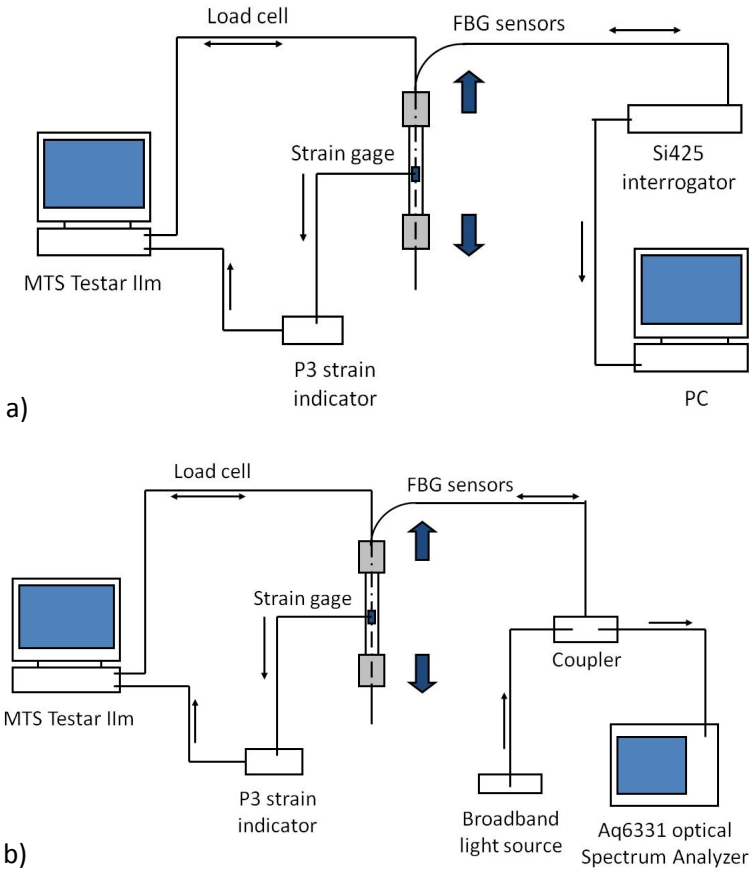

Figure 22: Experimental set up used with a) Si425 interrogator and b) Aq6331 OSA.

Fatigue testing was run to failure or was stopped after 1,000,000 cycles if the specimen did not fail. In this thesis "failure" refers to the ultimate failure (i.e. fracture). Once mechanical testing was completed, specimens were sectioned and used for damage analysis. In the case of a failed specimen, three samples were cut from one of the delaminated plies along the centerline (Figure 23a), and studied under JEOL JSM-6380LV scanning electron microscope (SEM) and an optical microscope with PAXcam 3 digital camera. One specimen that remained intact after testing was sectioned, and its cross-sectional areas were observed under an optical microscope. Figure 23b shows the locations of the cuts and the surfaces that were observed. These samples were cut with a water cooled diamond saw and then mounted into a puck to allow for easy handling. The puck was made from Lecoset^{TM} 7007 cold-curing resin, and a cookie cutter was used as a mold. Subsequently, to prepare samples for microstructural or damage examination, their surfaces were abraded (180, 320, 600 and 1200 grit paper with water) and polished (LECO^{R} 1 micro diamond compound, red felt cloth and diamond extender). Prior to moving from one abrasive step to the next finer step, the surface was checked under an optical microscope to ensure that previous larger scratches were removed.

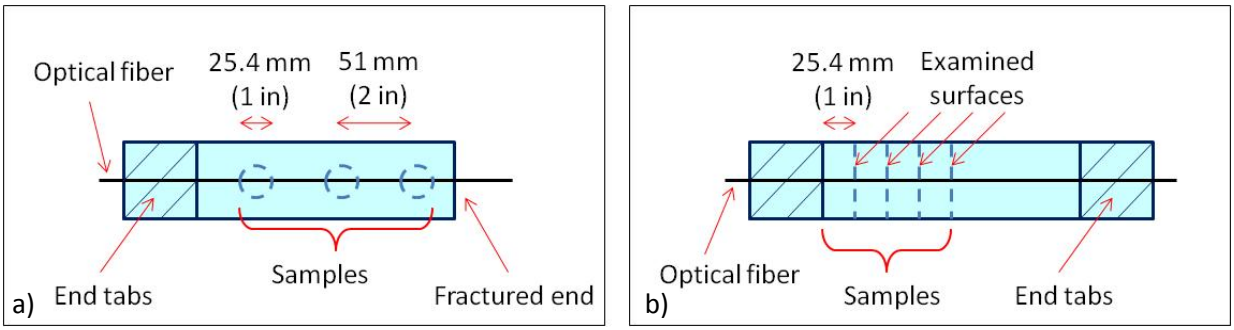

Figure 23: Samples used a) to study the surface of delaminated plies and b) to study the cross-sectional damage.

4.2.3 Data Analysis

Non-uniform strain distribution in the vicinity of a grating causes a distortion of the reflected spectrum, hence leading to spectrum widening, drop in signal intensity and peak splitting (chirping). This sensitivity can be utilized to detect damage initiation and track damage progression by monitoring changes of the FBG spectra. However, strain measurements might become problematic due to excessive chirping. To study stiffness degradation, it is important to obtain the average strain acting on the grating along its length. Thus instead of using the peak wavelength to track spectral shifts, an effective Bragg wavelength was found by applying the following steps (see Figure 24):

1. Measure power at the peak wavelength (max power or intensity);
2. Compute half-power;
3. Find bracketing wavelengths that correspond to the half-power; and
4. Calculate the effective Bragg wavelength by averaging these bracketing wavelengths.

This method provided an 'average' shift of the spectrum.

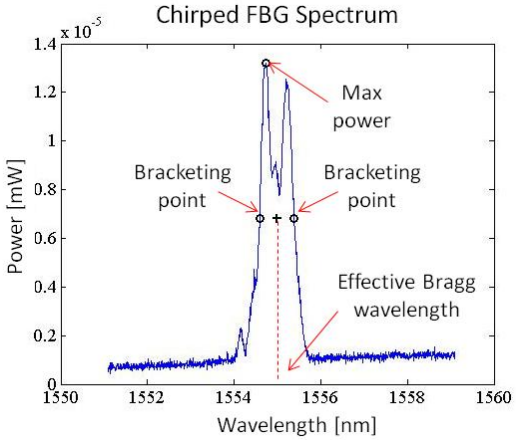

Figure 24: Chirped FBG spectrum and the wavelength-power points used to find an effective Bragg wavelength.

Data recorded with the interrogator was also affected by chirping. Figure 25 illustrates wavelength data, which corresponded to three FBGs, recorded during (a) static and (b) fatigue loading. In these graphs only the first five wavelengths were plotted even though at times as many as 15 were recorded. It is evident that the reconstruction of such data is a tedious process of questionable accuracy, hence making it unusable for present day work. When chirping was not significant the interrogator data was used to calculate stiffness. Direct synchronization of the LVDT and the interrogator signals was not possible, because the interrogator was not compatible with the controller of the universal testing machine (MTS). Alternatively, stiffness was determined by dividing the slope of the wavelength-time plot from the interrogator [nm/s] by the slope of the force-time plot from the LVDT [N/s] obtained during quasi-static testing. To quantify stiffness degradation, measurements were normalized by the initial value of stiffness.

Strain gages failed (i.e. were no longer reading strain) early on during fatigue, nonetheless, it was desired to compare stiffness drop measured by the FBGs to an alternative technique. For this purpose the LVDT force-displacement data was used to determine the relative 'stiffness' degradation during fatigue. This method is based on the assumptions that the length of the specimen between the grips is the same for each test (static or fatigue), and that strain is uniform along the length of the specimen. Even though these assumptions could not be entirely met during the fatigue test, the changes in the force-displacement response of the specimens provided adequate information regarding stiffness degradation and its severity.

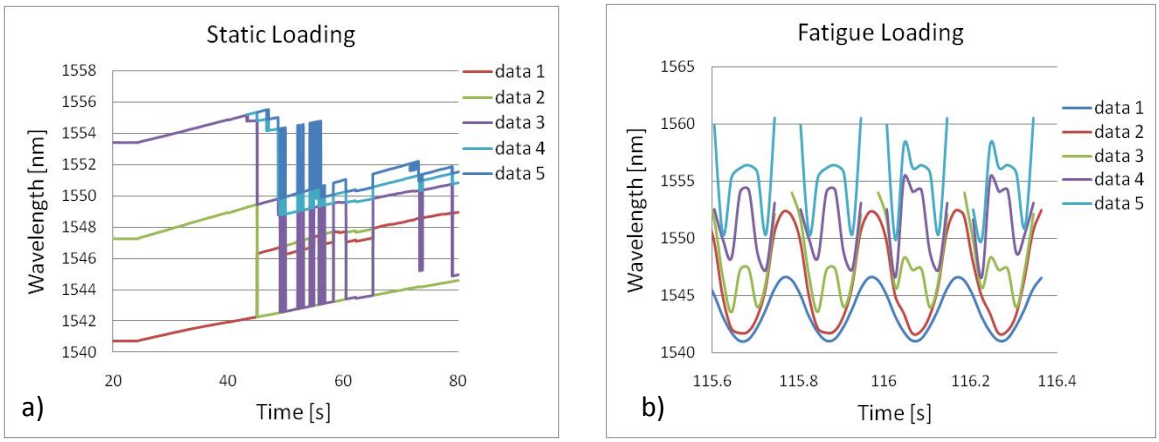

Figure 25: Wavelength data recorded by the interrogator during a) static and b) fatigue loading.

4.3 Strain Measurement: FBG vs. Strain Gage

Strain measurements recorded with embedded FBGs during the initial static test (prior to fatigue) were compared to those made with strain gages, as presented in Figure 26. Both types of sensors showed a linear stress-strain response of the material, which is be expected of $[0/90]_s$ unidirectional or woven laminates [19, 26]. However, there was a noticeable discrepancy between the FBG and the strain gage data.

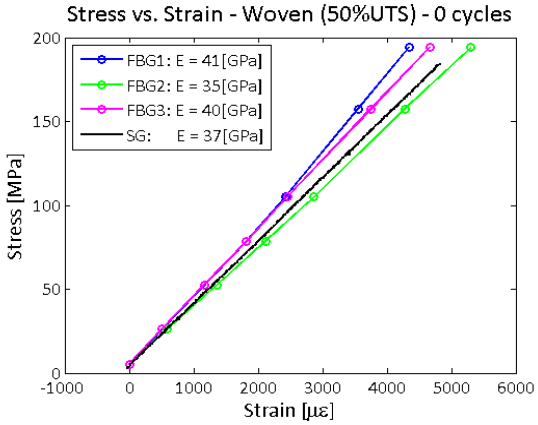

Figure 26: Comparison between the stress-strain relations measured with FBGs and a strain gage (SG) prior to fatigue.

By considering the evolution of the FBG spectra (Figure 27) with increase in loading it is evident that peak splitting occurred even at fairly low loads (~6700 N or 2000 μm), hence introducing an error into strain calculations. The onset of chirping can be attributed to the presence of damage or microstructural variation (i.e. interweaving warp and weft fibers). In fact, Güemes *et al.* [65] showed a 10% difference in strain measurements between FBGs that were surface mounted above the warp and weft fibers. Hence the initial chirped shape of the spectra (Figure 27b) can potentially be related to the warp-weft interaction. However, to properly support this argument a more accurate analysis of the microstructure or the damage state of the specimen at the onset of chirping is required. Such analysis can be achieved by the microscopic observation of the surface and the cross-section of the specimen. Also, the sensitivity of the FBG signal to the microstructural variations of the host specimen can be further studied by testing embedded FBGs of varying lengths. A longer grating (more than a unit cells) is expected to better capture global strain seen by the specimen, whereas a shorter grating (less than a unit cell) would capture a more localized strain value. However, if the material is damaged a longer grating would undergo more severe chirping than a shorter grating, as previously shown by Peters *et al.* [64].

With the further increase in static loading (>6700 N), chirping of the FBG spectra became more severe. This form of chirping (Figure 27d) suggests of damage initiation. In fact, during static loading cracking was heard and upon unloading the specimen, fine cracks were observed in the resin rich areas where the warp and weft fibers overlap, Figure 28.

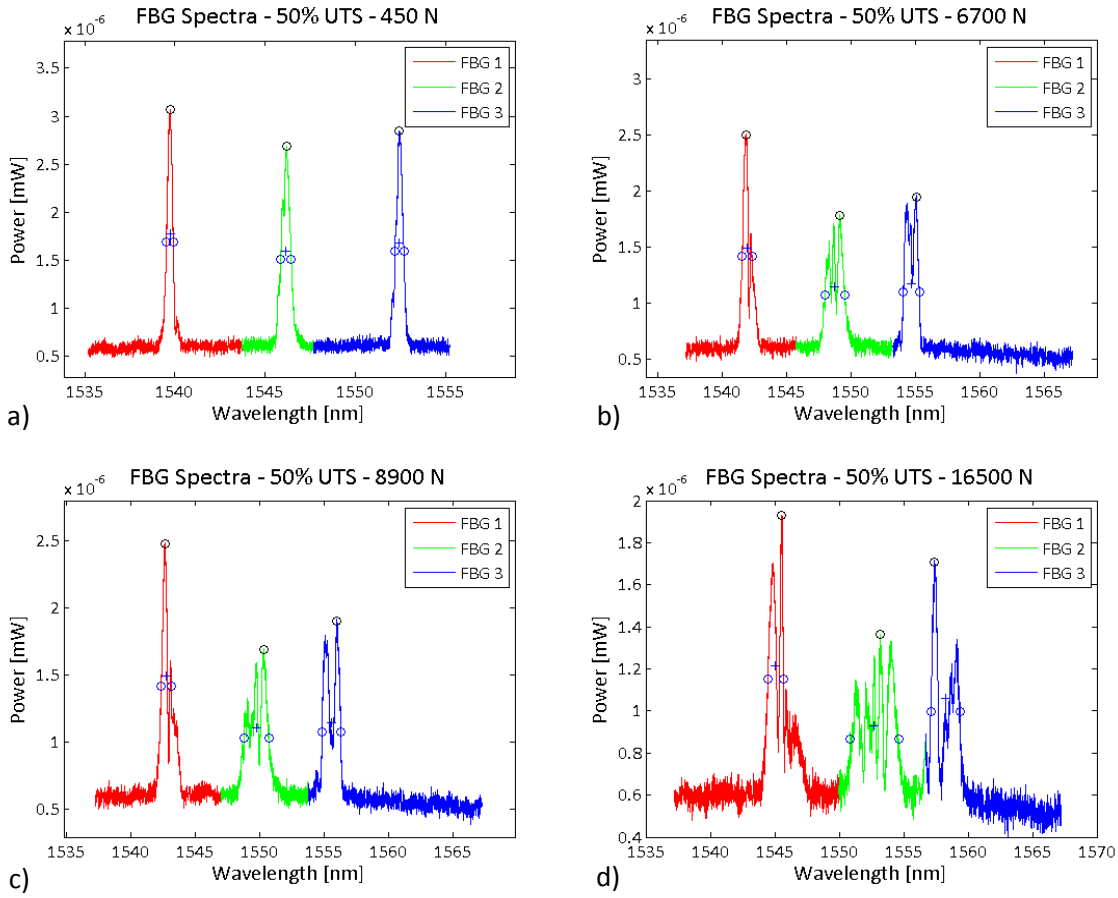

Figure 27: FBG spectra recorded at a) 450 N, b) 6700 N, c) 8900 N and c) 16500 N at 0 cycles (Woven (50% UTS)).

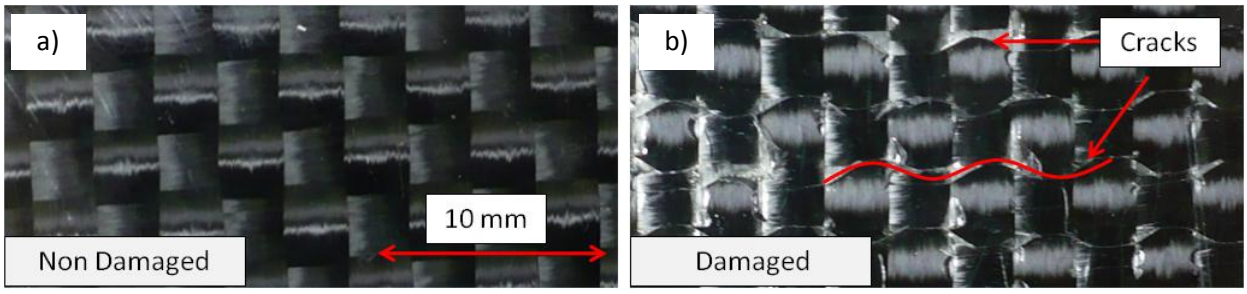

Figure 28: Woven specimen in its a) original non-damaged and b) damaged states. The shape of the cracks formed between the warp and weft yarn is shown by the red line.

The possibilities of misalignment errors also exist since these laminates were manufactured by a wet hand lay-up method, and a hand roller was used to distribute resin, hence potentially shifting the OF. In fact, upon the failure of one of the specimens, the two delaminated surfaces were observed and it was determined that the OF was not straight and had shifted from the centerline of the specimen. Figure 29 clearly illustrates the misalignment between the orientation of the OF and the adjacent warp bundles. These images were captured by an optical microscope (Figure 29a) and an SEM (Figure 29b).

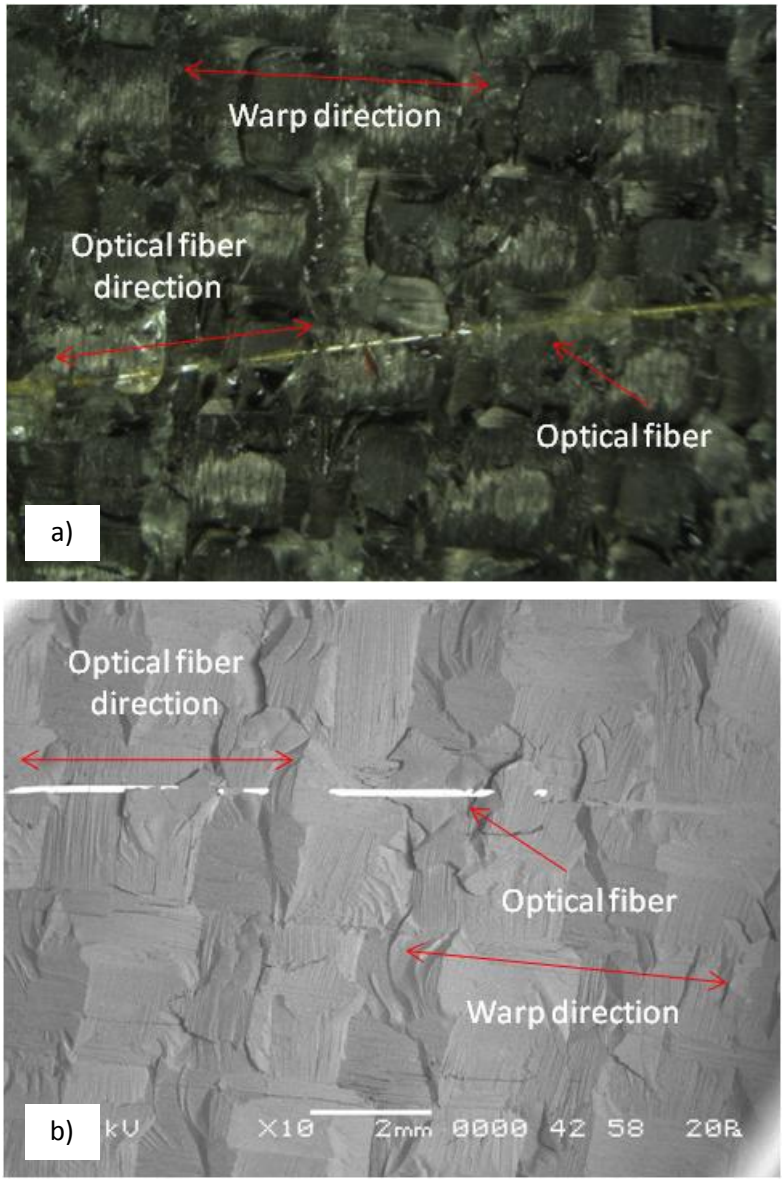

Figure 29: Misalignment between the orientation of the OF and the warp fibers. Images were taken with a) an optical microscope and b) an SEM.

4.4 Monitoring Damage Evolution

4.4.1 Failure Characteristics

Out of the three specimens that were tested, only one specimen, which was fatigued at 70% UTS, has failed. The other two remained intact until testing was terminated after 1,000,000 cycles. Table 2 summarizes the failure results of the specimens and the FBG sensors. Unfortunately some of the sensors have failed during fatigue. However, it is interesting to note that FBGs either failed during the first 15,000 cycles or have lasted for the entire test. The following Section 4.4.2 on FBG Spectral Analysis will propose reasoning for premature sensor failure in connection to damage formation in these laminates.

Table 2: Summary of the failure results of specimens and FBG sensors.

Specimen	Max Load Level (% UTS)	Specimen Failure (cycles)	FBG Failure
Woven [(0#90)/FO/(0#90)]	50	1,000,000	1 FBG failed after 10,000 cycles
	60	1,000,000	2 FBGs failed after 15,000 cycles
	70	740,000	3 FBGs failed after 3,000 cycles

Initial form of damage in woven specimens was the onset of matrix cracking that formed in the warp-weft overlap region and was observed after the initial static test. With continuation of cyclic loading these cracks extended in the widthwise direction and formed a curvy sinusoidal pattern, as shown in Figure 28. One of the specimens that did not fail was sectioned after the test. Cross-sections were examined with an optical microscope. Presence of delamination was clearly observed, as shown in Figure 30, and it essentially extended through the entire width of the specimen. Moreover, Figure 31 clearly illustrates the presence of delamination in the vicinity of the OF. Additional images can be found in the Appendix - A (Figure A1, Figure A2 and Figure A3).

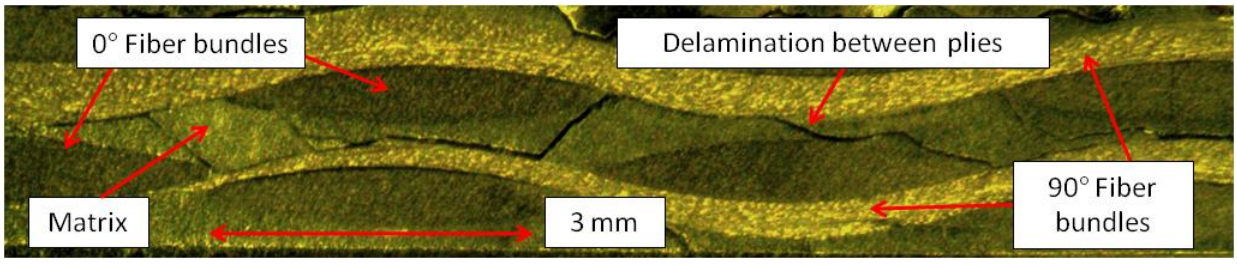

Figure 30: Propagation of delamination between the two woven plies.

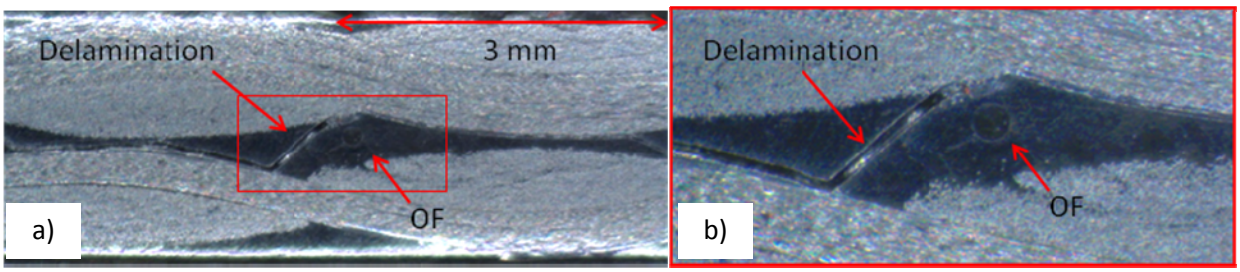

Figure 31: Presence of delamination in the vicinity of an OF captured at two magnifications; b) shows a magnified image of the section defined by a red box in (a).

Figure 32a and b illustrate final fracture of the failed specimen. It is evident that the two woven plies completely delaminated and that the specimen finally failed when the 0° fibers had broke. Fiber breakage occurred close to the grips along the 90° or the 45° line. SEM analysis of a delaminated surface (Figure 33) showed presence of hackle marks that are characteristic to brittle fracture [22]. Overall, the brittle nature of the resin contributed to the early initiation of matrix cracking. Additional images that capture the non-damaged (Figure A4) and fractured (Figure A5 and Figure A6) states of the specimen and the fracture surfaces (Figure A7, Figure A8 and Figure A9) can be found in Appendix - A.

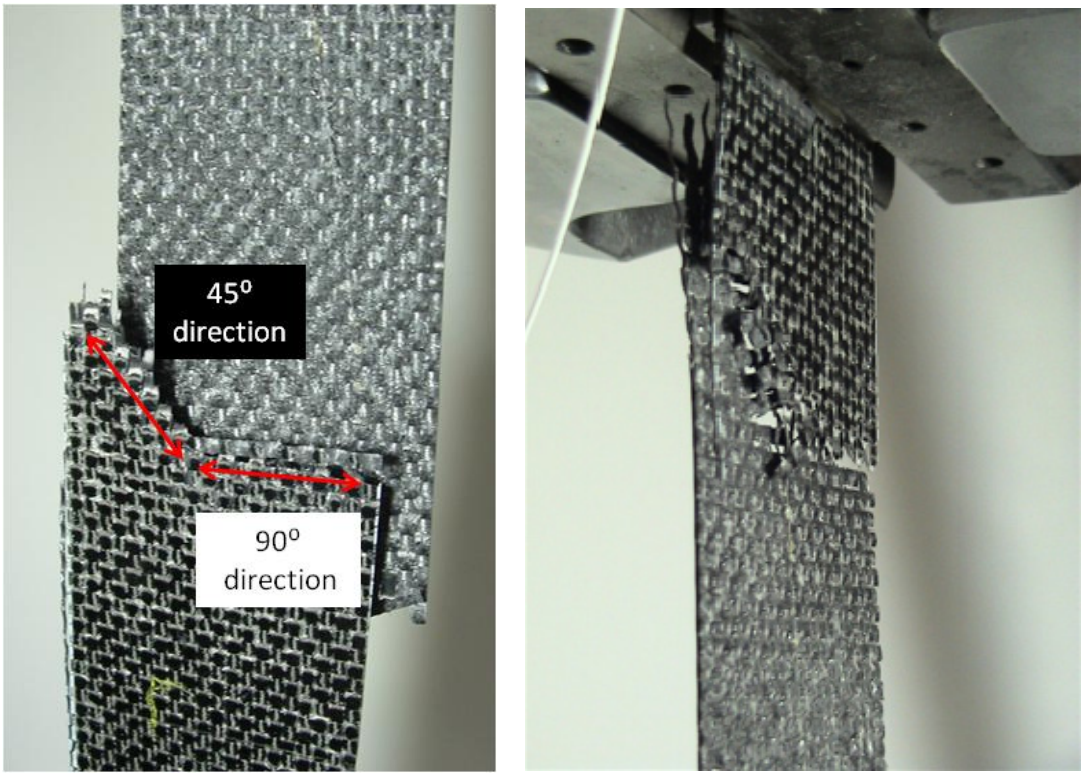

Figure 32: Fracture characteristics of a failed woven laminate.

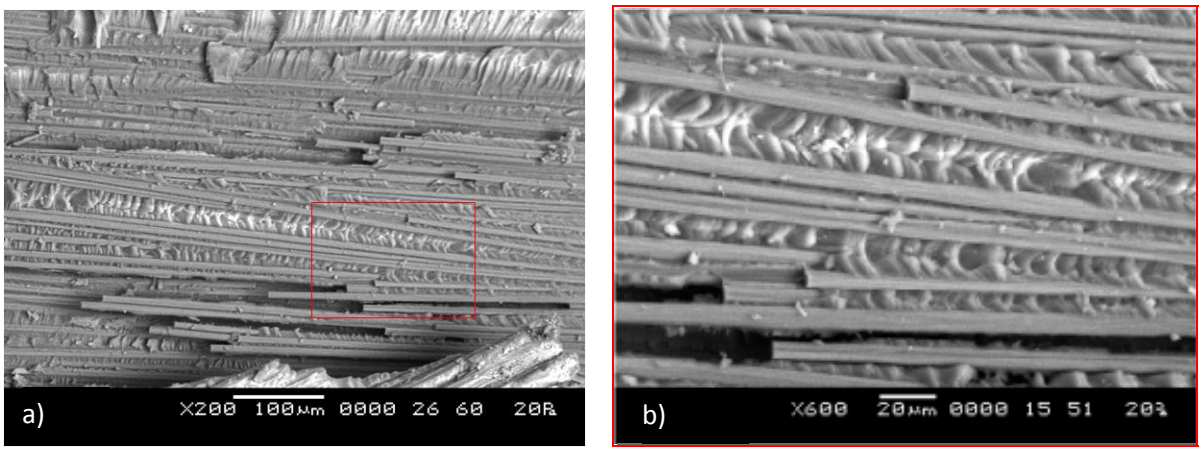

Figure 33: Fracture surface of a woven specimen with hackle marks captured at a magnification of a) x200 and b) x600.

4.4.2 FBG Spectral Analysis

An advantage of the FBG strain sensitivity is that it can be used to monitor damage progression. Generally, with the onset of damage, the FBG spectrum is expected to widen, experience a drop in intensity and exhibit chirping. This section will present the evolution of the FBG loading spectra during fatigue and will attempt to related these changes to the characteristic failure modes of woven laminates. In this report FBG loading spectra refers to a set of FBG spectra recorded during a single static test at different static loads (Figure 34).

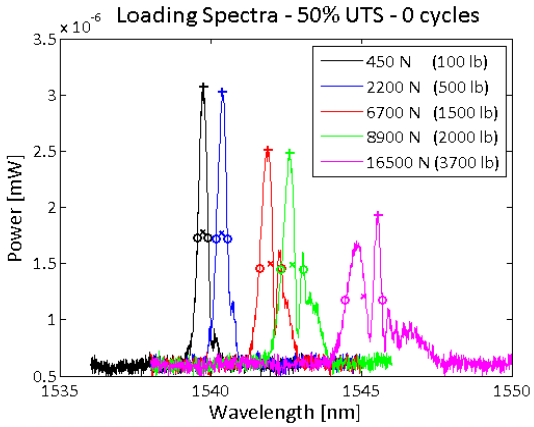

Figure 34: Loading spectra of the FBG1 recorded during the initial static test of Woven (50% UTS).

By first examining the initial loading spectra (Figure 34 or Figure 27) corresponding to the woven specimen fatigued at 50% UTS, it is evident that peak splitting occurred at low loads and became significantly more drastic at high loads. After unloading the specimen, matrix cracks were clearly visible in the warp-weft regions, see Figure 28. Hence it can be speculated that the presence of cracks caused

the spectra to chirp at higher loads. However, at lower loads the slight peak splitting can be linked to relative stiffness difference between the warp and weft fiber bundles and the matrix that was detected by the FBGs.

Moreover, the spectral shapes (Woven 50% UTS) did not change considerably until the 10,000 cycles mark; then they became significantly chirped even at low loads, and the signal from one FBG was lost, see Figure 35. This spectral change suggests the onset of a new failure mode, possibly delamination. Also since the stress level was fairly low for the optical fiber to break due to the longitudinal strain, it can be hypothesized that the FBG broke in shear caused by delamination or debonding.

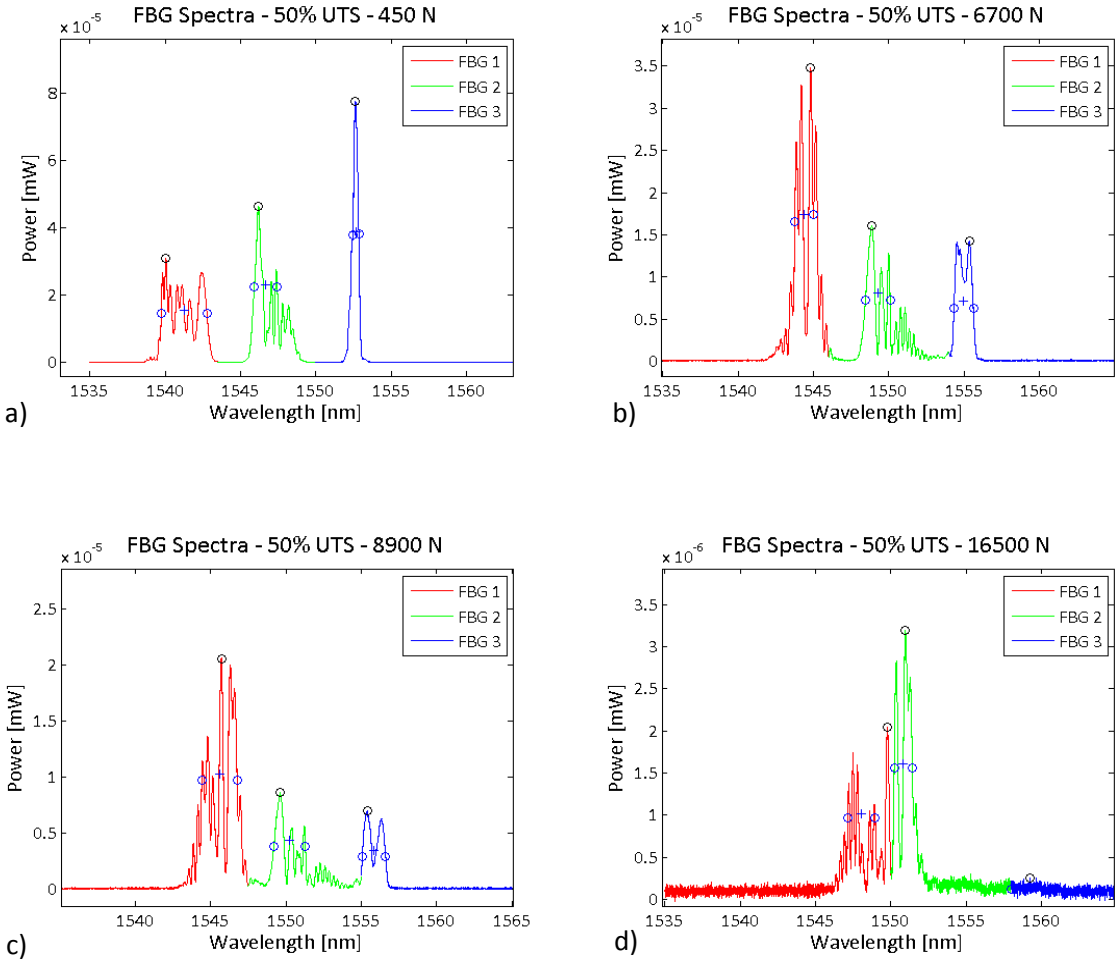

Figure 35: FBG spectra recorded at a) 450 N, b) 6700 N, c) 8900 N and d) 16500 N after 10,000 cycles (Woven (50% UTS)).

As fatigue testing progressed, the spectral profile began to "clean up". At 200,000 cycles the loading spectra of FBG1 restored itself to essentially a single peak (Figure 36a) and remained this way for the remainder of the test (Figure 36b). Such change could be caused by the complete debonding of the FBG.

This event can be anticipated since woven laminates failed by delamination, and the optical fiber was embedded between the two delaminated plies, as shown in Figure 29 - Figure 32.

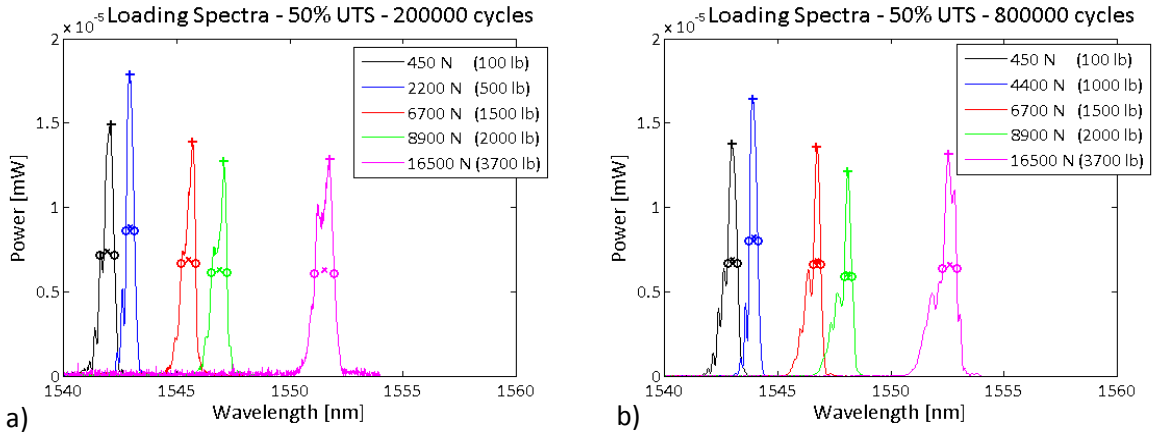

Figure 36: FBG1 loading spectra recorded after a) 200,000 cycles, b) 800,000 cycles (Woven (50% UTS)).

Similarly, by observing the loading spectra of the FBG2 after 50,000 cycles (Figure 37a), it is evident that the spectrum recovered from its previously chirped condition (Figure 35) and remained essentially unchanged until the end of the test, Figure 37b. However, under low loads (450 N) the spectrum was split into two peaks, and with increasing loading the intensity of one peak increased, whereas the intensity of the other decreased, Figure 37. This behavior of an FBG was previously reported to be caused by debonding or delamination [16].

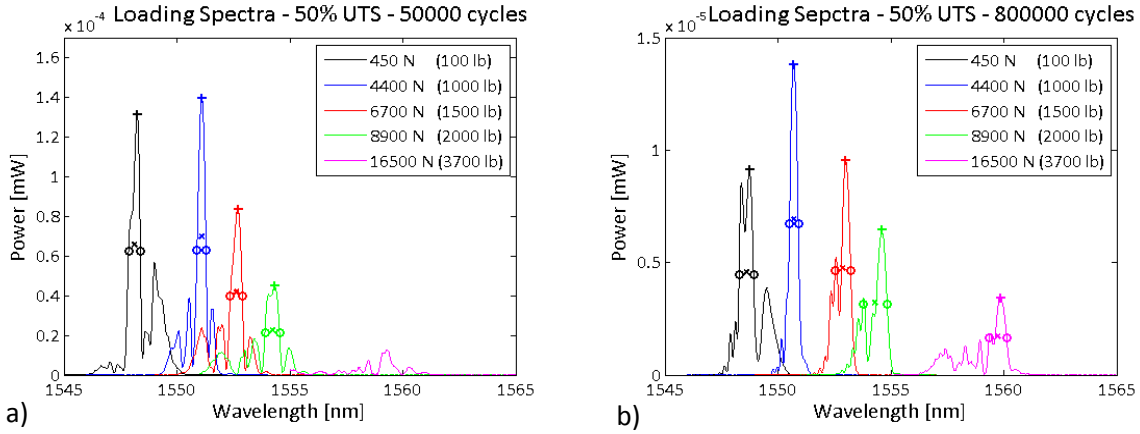

Figure 37: FBG2 loading spectra recorded after a) 50,000 cycles, b) 800,000 cycles (Woven (50% UTS)).

Furthermore, data captured by the interrogator has also improved significantly once the optical spectrum was restored. Figure 38 shows a sample of wavelength data recorded around the 800,000 cycles mark. Overall, analogous results were obtained with the specimen fatigued at 60% UTS. Thus far results indicate that FBGs are capable of detecting the onset of different failure modes and the transition between them. However, additional testing is required in conjunction with other techniques, such as SEM, to obtain a more exact correlation between the damage state of the material and the FBG loading spectra.

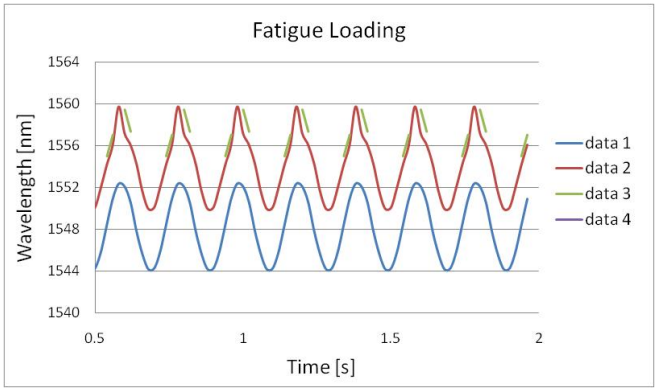

Figure 38: Wavelength data recorded by the interrogator around the 800,000 cycles mark (Woven (50% UTS)).

4.5 Monitoring Stiffness Degradation

As discussed in the previous section, chirping of the FBGs was substantial during the early stages of fatigue (<200,000 cycles) and consequently has significantly complicated strain measurements. To deal with chirping an effective Bragg wavelength (as discussed in the Data Analysis section) was approximated from the spectral data and was used for the calculation of strain and stiffness values. Approximation of the Bragg wavelength was difficult from the interrogator data since multiple wavelengths were recorded for a single sensor (Figure 25). As a result, only OSA data was used to quantify stiffness degradation during the early stages of fatigue. However, during the later stages once the loading spectra were restored, both the OSA and interrogator data were used.

The fatigue evolution of the load-strain curves, which was obtained through the OSA spectral analyses, is presented in Figure 39. This data pertains to the specimen fatigued at 50% UTS. It should be noted that in Figure 39 curves corresponding to 10,000 and 25,000 cycles are linear at low load levels (<8,000 N) but are incoherent at higher levels (>8,000 N). This incoherence is a result of errors associated with determination of the Bragg wavelength in the presence of chirping, which was more severe at higher load (or strain) levels, refer to Figure 35. Hence data points corresponding to loads above 8,000 N were

ignored in the analysis and hence not used for stiffness calculations. From Figure 39 it is evident that stiffness degradation experienced by woven specimens was fairly high (≈35%). This significant stiffness drop occurred due to the formation of transverse cracks at the boundary between warp and weft yarn, see Figure 29, thus permitting the warp bundles to straighten out and making the woven fabric more flexible. These results are in par with previous investigations [4, 6].

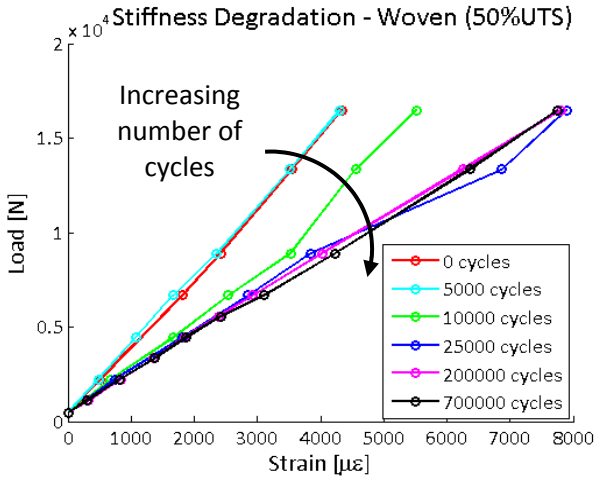

Figure 39: Stiffness degradation of the woven specimen tested at 50% UTS.

Stiffness degradation was further analyzed by comparing data obtained for different specimens and measured with different sensors. Figure 40a shows the normalized stiffness degradation curves derived from measurements with the FBGs (OSA and interrogator) and the LVDT for the specimen fatigued at 50% UTS. Figure 40b shows stiffness degradation curves for all specimens measured will all sensors. All sensors displayed the same pattern of stiffness degradation, the initial drastic drop before 100,000 cycles and then subtle degradation. Results obtained with the interrogator and OSA data for the same sensor (Figure 40a) were similar. The general noise in the FBG results is attributed to the misalignment of the OF and chirping of the FBG spectrum. Also, the magnitude of the stiffness drop was in the same range among the specimens despite the difference in the applied loading.

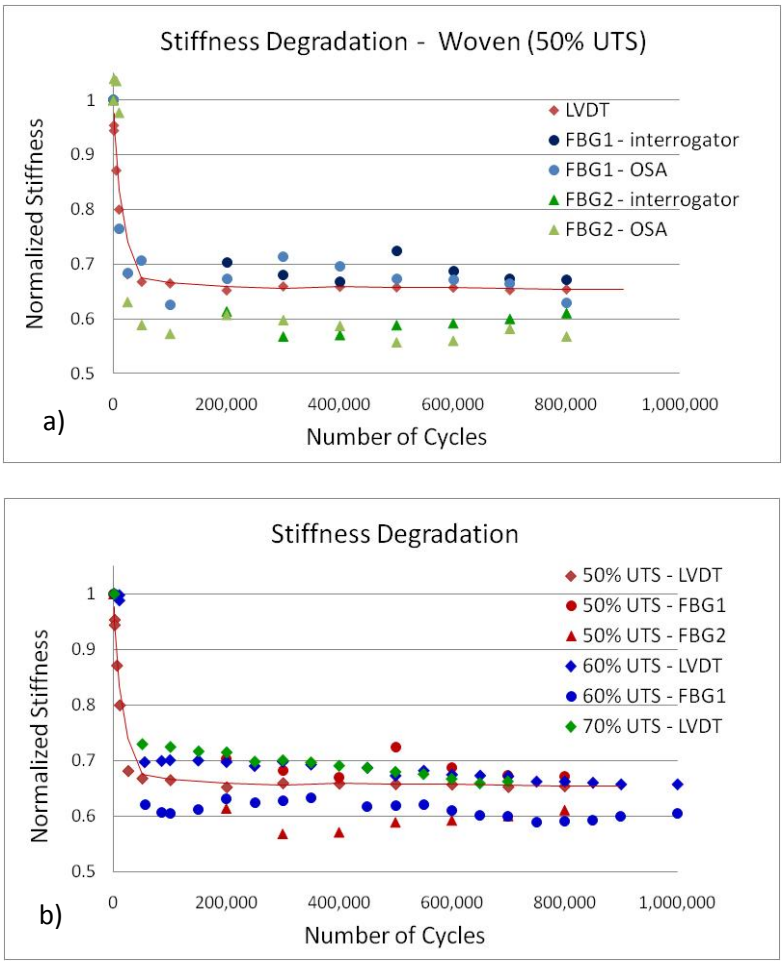

Figure 40: Comparison between stiffness degradation measured with FBGs and LVDT for a) Woven (50% UTS) and b) all the specimens combined.

Results obtained thus far show that FBGs are capable of detecting stiffness degradation, but further testing is required to achieve a better quantitative measure of the stiffness drop. The main difficulty in accurately capturing a stiffness drop can be attributed to the FBG sensitivity to strain non-uniformity created by cracks and delamination. Specimens considered in this study developed matrix cracks and began to delaminate early on in their fatigue life. However, in practical applications the part or component is taken out of service if it develops cracks and starts to delaminate beyond an allowable limit. The author believes that in this study specimens were fatigued beyond their allowable limit, and hence FBGs were subjected to a harsher environment, in terms of strain non-uniformity, than what is expected in practical applications. In other words, if a specimen lasted a larger number of fatigue cycles prior to the onset of any significant damage, FBG loading spectra would be cleaner and would provide an accurate measure of the stain in the material for a much longer time. In this case the onset of chirping would signal damage formation and call for further inspection or maintenance.

4.6 Concluding Remarks

In this study woven laminates with embedded arrays of multiplexed FBGs were manufactured by a hand lay-up method and subjected to high strain fatigue loading. FBG signals monitored with the OSA and the interrogator were used to derive information regarding the damaged state of the specimens and the corresponding stiffness loss. Stiffness degradation detected with FBGs was similar to that detected by an LVDT. The general shape of the stiffness vs. the number of cycles plot indicated that stiffness dropped sharply during the initial 100,000 cycles and then decreased subtly until 1,000,000 cycles. Although FBGs are able to detect stiffness degradation, further studies are required to assess their ability to accurately quantify its magnitude.

Spectral analysis of FBGs provided a qualitative description of the damage state of the laminate. The onset of chirping during the initial static test corresponded to the initiation of matrix cracks. Further worsening of chirping appeared to be linked to debonding of the OF or delamination of the plies. However, the consecutive restoration of the spectra suggested of complete debonding of the grating. Future testing is required to further support these conclusions and to precisely characterize spectral changes with respect to damage propagation. For damage monitoring the OSA was shown to be a more useful tool than the interrogator since it captured the whole spectrum.

With regards to the durability of FBG sensors, they either failed before 15,000 cycles or have lasted the entire test. It seems that initiation or propagation of delamination in between the plies might have caused FBGs to break. Hence the author believes that if the OF was embedded in a less hostile environment, the sensors would last significantly longer. Likewise, FBG sensors that remained functional for the entire test demonstrated their ability to survive prolonged exposure to cyclic mechanical loading.

Overall, FBGs has the potential to be utilized for in-situ health monitoring of parts and components during their lifetime. However, it should be noted that chirping might seriously hinder data analysis especially in the case of the interrogator data since only peak wavelengths are recorded.

5 Fatigue Monitoring at Elevated Temperature

5.1 Motivation and Objectives

The development of advanced polymers that can withstand prolonged exposure at elevated temperatures (ET) has sprung considerable interest in the utilization of polymer matrix composites (PMCs) for high temperature applications. The applications include but are not limited to supersonic vehicle airframes and jet engine components. Previous studies have investigated mechanical properties of polyimide (e.g. PMR-15) and bismaleimide (BMI) PMCs at temperatures up to 200^{o}C [8, 10, 22, 35, 43]. The next generation of polymers, such as polyimide MVK-10, will be able to raise the temperature limit to 300^{o}C. One of the main research projects that are currently being conducted at the FRAMES laboratory at Ryerson University is geared towards the characterization of the mechanical properties of carbon/MVK-10 PMC at ET. The experimental work to be discussed in this chapter was performed as a precursor to the work that will be done on the aforementioned MVK-10 PMC. The goal of this project is to familiarize the author and her colleagues with the test procedures and requirements specific to ET and to study the effect of temperature (up to 200^{o}C) on the mechanical properties and failure mechanisms of PMCs.

There are drawbacks with the application of strain gages (SG) and extensometers for monitoring mechanical properties during fatigue. Strain gages have a fairly low strain limit (<3000με) during cyclic loading, and extensometers might have a problem with slippage of the probe edges on the specimen surface at high loading rates and strain values. An alternative technique for strain and stiffness monitoring involves the application of fiber Bragg grating (FBG) sensors, which can withstand high cyclic strains and temperatures. Additionally, FBGs have been previously utilized for damage monitoring and have shown the potential for this application [15-18, 67–76]. However, as discussed in Chapter 4, the formation of damage in the vicinity of the grating causes the spectrum to chirp and this might complicate strain calculations. Aiming to address this problem, two methods were considered for bonding FBGs to the specimen surface. One FBG was bonded by applying adhesive along the full length of the grating so that it would be sensitive to localized strain variations. Alternatively, one FBG was bonded by gluing the optical fiber in two locations at opposite sides of the grating so it would function as an extensometer. Overall, the objective of this study is to assess the applicability of FBGs for stiffness and damage monitoring of PMCs at elevated temperatures as well as to compare the results of the two bonding methods.

5.2 Experimental Set-Up

5.2.1 Specimens

Specimens under investigation were woven (8-harness satin) carbon/BMI laminates. All the plies were oriented at 45^{o} to the loading direction. This material was supplied by another party and detailed information about the manufacturing process and material properties is proprietary and cannot be disclosed. Similarly, in the results section the force vs. strain curves will be presented instead of the stress vs. strain curves and all the strain data will be scaled by a factor **N**. Specimens had a nominal length of 470 mm [18.5 in] and were cut using a water-jet cutting technique to ensure good edge quality. These specimens were quite long since they had to be of sufficient length to protrude outside the furnace to allow for gripping. Figure 41 shows specimen dimensions.

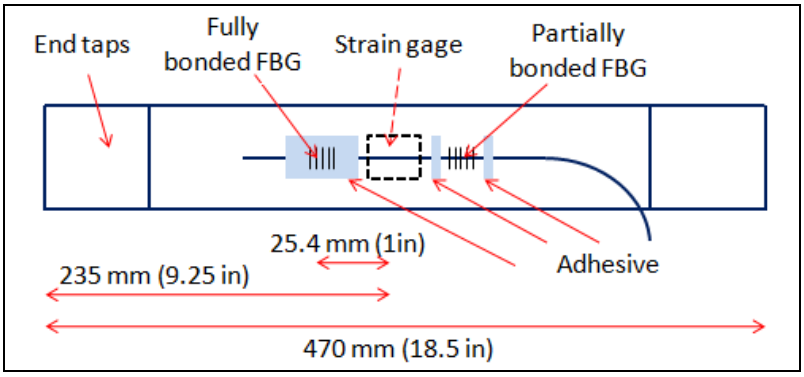

Figure 41: Specimen dimensions, and location of a strain gage and FBGs on the surface of a specimen.

An optical array with two FBGs was bonded in the center section of the specimen, as shown in Figure 41. The two FBGs were bonded by different techniques to assess and compare their usability for strain and damage monitoring. One FBG was fully bonded to the surface; adhesive was applied along the full length of the grating to make that FBG sensitive to the strain variation in the vicinity of the grating. For the other FBG, the optical fiber was bonded in two spots approximately 15 mm [0.6 in] away from either end of the grating, while the grating itself was not directly bonded to the specimen [FBGs bonded in this manner are referred to as partially bonded in this report]. It was anticipated that the partially bonded FBGs would function like an extensometer and measure the global stress-strain behavior of the material. The FBGs were positioned 51 mm (2 in) apart, as shown in Figure 41. This positioning allowed for ease in handling (during bonding) and ensured that FBGs were located within a uniform temperature zone in the furnace (to be discussed in Section 5.2.2). In the case of specimens tested at room temperature (RT), only one fully bonded FBG was used and it was positioned in the center of the specimen.

Fiber optic sensors were fabricated at the Fiber Optic Communication and Sensing Laboratory at Ryerson University. FBGs used for testing at RT were written on a polyacrylate coated OF, and those used for testing at ET were written on a polyimide coated OF. Once the gratings were written, they were coated with protective polyimide coating (Ø 160 µm) and annealed at 150°C for 15 hours to ensure their long-term stability. Gratings were 5-8 mm in length and had wavelengths in the range of 1535-1555 nm.

To allow for correlation of the FBG data, a strain gage was also bonded to the surface of the specimen opposite the OF. It was positioned in between the fully and partially bonded FBG, as shown in Figure 41. In the case of RT specimens the strain gage was bonded directly opposite the FBG. For testing at RT, 105°C and 160°C standard Vishay EA series strain gages were used, whereas for testing at 205°C a Vishay WK series strain gage was used.

Overall, the same bonding procedures were used for strain gages and FBGs, while FBGs were pre-strained to avoid buckling of the OF during unloading. Prior to bonding the surface of the specimen was degreased, wet abraded (400 grid), conditioned and neutralized. Two types of adhesives were used depending on the test temperature. For RT specimens instant adhesive (Loctite 496) was applied and allowed to air-dry at RT. For ET specimens M-Bond 610 was used and the cure cycle recommended by the manufacturer was followed. With this adhesive, a set up involving clamps, aluminum plates and rubber was used to apply even pressure on the optical fiber and the strain gage during the cure time, as illustrated in Figure 42. Also, prior to testing tapered aluminum end-tabs, which were 50 mm [2 in] long, were glued to the specimen with contact cement.

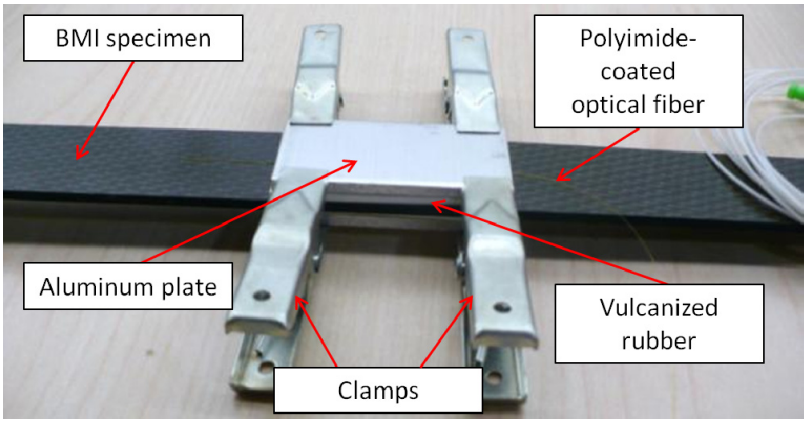

Figure 42: Set-up used to apply even pressure on the optical fiber and the strain gage during cure.

5.2.2 Test Protocol

A total of six specimens were tested at static or fatigue loading and at temperatures ranging from RT to 205^{o}C, as summarized in Table 3. Interrupted fatigue tests were performed in combination with static tests in order to monitor stiffness degradation and damage development. Data recorded during fatigue tests was used to assess the usability of FBGs for in-situ fatigue monitoring. Data from the static tests was used to measure stiffness reduction and damage progression during fatigue. Once mechanical testing was completed, specimens were sectioned and studied under the scanning electron microscope (SEM) in order to characterize damage. Two specimens were not tested to failure and were used to assess the damage state of the laminates during the early stages of fatigue. In this thesis "failure" refers to the ultimate failure (i.e. fracture).

All tests were conducted using an MTS 322 test frame, MTS 647 hydraulic wedge grips, and MTS FlexTest GT/Teststar IIm controller and data acquisition unit. For testing at elevated temperatures, the ATS 3210 furnace with an integrated temperature controller was used. This furnace has three heating zones, each with a K-type thermocouple for temperature feedback to the controller, as shown in Figure 43. To minimize the heat loss and promote thermal stability of the system, high temperature insulation was used to close off any openings in the furnace. Additional images of the experimental set up (Figure B1) can be found in Appendix - B.

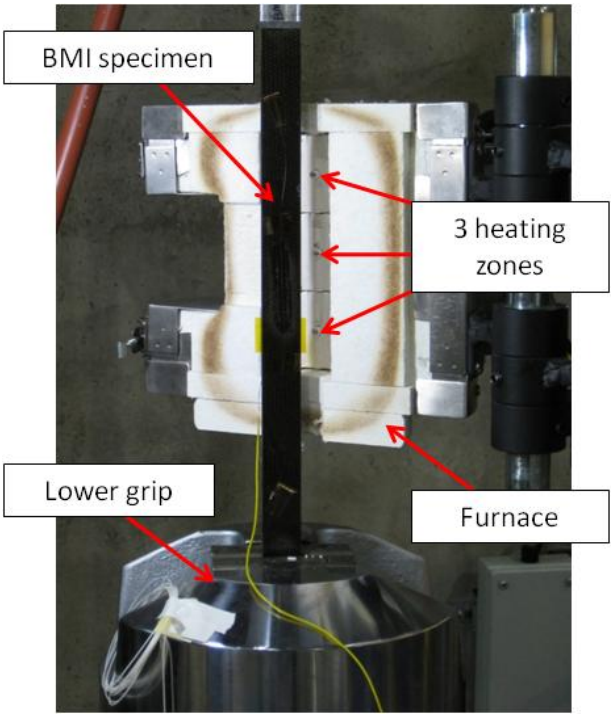

Figure 43: Experimental set-up showing the specimen, the grips and the furnace.

Previous calibration tests have shown that temperature is uniform (within $\pm 2^{o}$C) in the center of the furnace. However, the temperature decreases by as much as 20^{o}C when going from the central region to the top or the bottom of the furnace. Hence specimens were always positioned such that FBGs and strain gages were in the uniform temperature region (~75 mm [3 in]). It was also noticed that temperature at the center of the furnace was higher than at the sides where the control thermocouples are located. For this reason, an additional K-type thermocouple placed in the middle of the furnace close to the specimen surface was used to measure the actual temperature of the specimen. Moreover, in order to test at a particular temperature ($\mathbf{T_{Desired}}$), the furnace temperature was set to a lower value ($\mathbf{T_{Furnace}}$), and the surface temperature ($\mathbf{T_{Surface}}$) of the specimen was taken as the actual temperature. Temperature values recorded for each test are summarized in Table 3. During cyclic loading, specimens exhibited self-heating, which is anticipated with off-axis specimens [1, 19, 24, 26]. The resultant specimen temperature during fatigue ($\mathbf{T_{Fatigue}}$) was also noted and is included in Table 3.

Table 3: Summary of the tested specimens, the loading conditions and the test temperatures.

Specimen (BMI [45#-45])	Type of Loading	$T_{Desired}$ (^{o}C)	T_{Set} (^{o}C)	$T_{Surface}$ (^{o}C)	$T_{Fatigue}$ (^{o}C)	Fatigue Loads (N [lbs])
BMI-01	Static to failure	RT	RT	RT	-	-
BMI-02	Fatigue to failure	RT	RT	RT	-	F_{max} = 6,700 [1,500]
BMI-03	Fatigue to failure	200	185	205	208	F_{max} = 4,900 [1,100]
BMI-04	Fatigue to failure	105	95	105	117	F_{max} = 6,700 [1,500]
BMI-05	Fatigue not to failure	150	145	160	165	F_{max} = 4,900 [1,100]
BMI-06	Fatigue not to failure	200	185	205	208	F_{max} = 4,900 [1,100]

During temperature ramp ups, the temperature was increased at a rate of 5 seconds/°C and was allowed to settle for 30 min prior to testing. Specimens were left unclamped in order to avoid buckling due to specimen expansion.

Fatigue tests were run under force control with stress ration R = 0.1 and at a frequency of 5 Hz. The maximum load level used for each specimen is given in Table 3. Two types of static tests were conducted between fatigue intervals. First, a quasi-static test was run in displacement control, and the specimen was elongated by 2.5 mm (0.1 in) at the rate of 0.6 mm/min. Measurements of wavelength, time and force, and strain were recorded with the interrogator, the LVDT, and the P3 strain indicator,

respectively. This data was used to monitor stiffness and generate the stress vs. strain curves. Secondly, the specimen was statically loaded to different load levels (about five or seven) up to the maximum cyclic stress, and while the force was kept constant, the FBG spectrum was recorded with the Ando A66331 optical spectrum analyzer (OSA). Spectral data was used for damage monitoring. It is also noteworthy that during unloading, displacement was never returned to a zero value but was rather brought to a near-zero magnitude of 0.2 mm in order to avoid buckling. Additional information regarding data acquisition and equipment set-up can be found in Section 4.2.2.

Finally, the mechanism of damage development in off-axis woven laminates was investigated. Samples of the surface areas and the cross-sectional areas were cut from the specimens and examined under the JEOL JSM-6380LV SEM. To evaluate the progression of damage, samples were cut from failed and non-failed specimens. In the case of failed specimens, samples were cut from different locations with respect to the fracture zone, as shown in Figure 23. With the non-failed specimens, only two samples (one cross-section and one surface) were cut from the central region and they were adjacent to one another. The cross-sectional samples were molded into pucks for the ease of handling and their surfaces were polished to reveal the microstructure (refer to Section 4.2.2). Also, in order to enhance the quality of SEM images, samples were gold-coated in Denton Vacuum Desk IV (CTC Parker Automation).

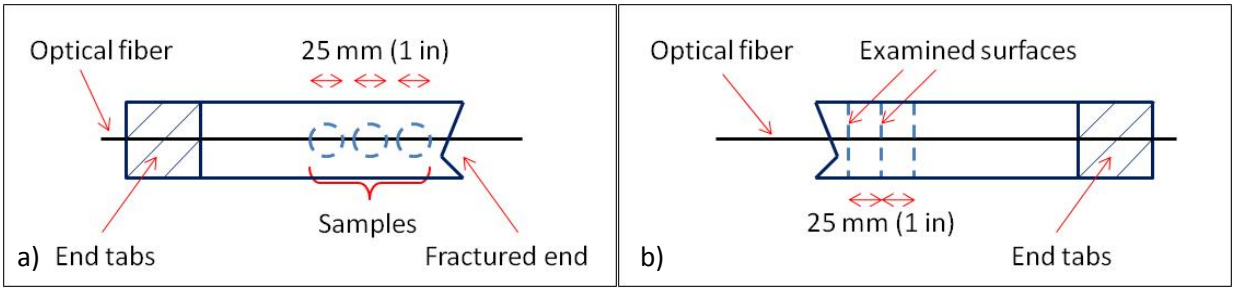

Figure 44: Samples used to study damage formation on the a) surface and b) thru the thickness of specimens.

Prior to commencing cyclic tests of the specimens, a number of preliminary tests were performed in order to assess the time and temperature dependence of off-axis BMI specimens. The experimental methodology and results of these tests will be covered in Section 5.3.

5.2.3 Data Analysis

The Data Analysis section in Chapter 4 was dedicated to dealing with chirping. However, as it will be later discussed in Section 5.5.1, chirping was not an issue with the BMI specimens and the measured peak wavelengths were used directly to calculate strain values. Instead of relying on the OSA data, the interrogator data was used for strain measurements. Direct synchronization of the LVDT and the interrogator signals was not possible, because the interrogator was not compatible with the controller of the universal testing machine (MTS), so synchronization of the data was performed manually. For this purpose, a short 5 second dwell was added to the ramp-up segment of a static test at a low displacement value of 0.2 mm. During the analysis, data was shifted with respect to time in order to align the dwell period of the LVDT and the interrogator data. Figure 45 shows the strain vs. time graphs obtained with the strain gage and the FBG data (a) prior to and (b) after synchronization.

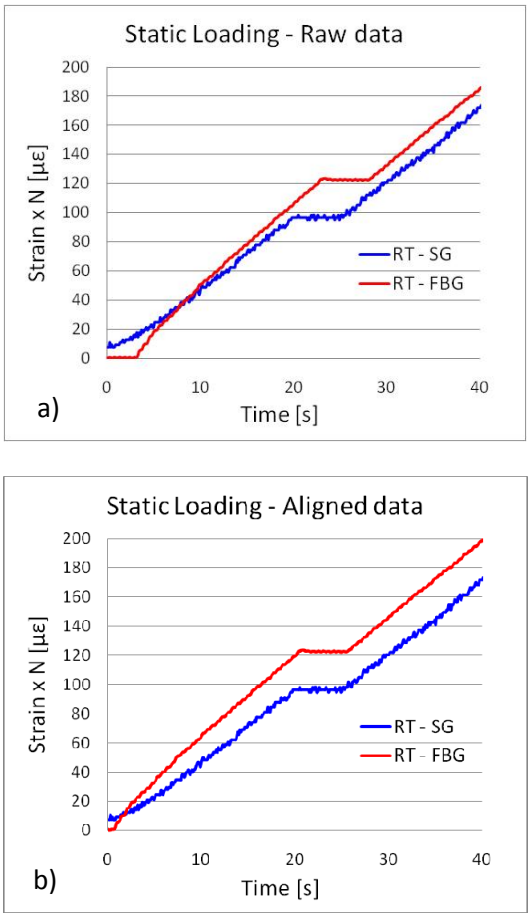

Figure 45: Strain vs. time graphs based on a) raw and b) synchronized data from a SG and an FBG.

5.3 Preliminary Test

An initial assessment of the time and temperature dependence of the BMI off-axis laminates was obtained by performing a series of static tests that accounted for different temperatures (RT-205°C) and loading scenarios. All tests were run in displacement control and acquired data from the P3 strain indicator, the Si425 interrogator, and the LVDT. The Type A test consisted of a single ramp-up stage up to a displacement of 2.5 mm and was followed by a short 5 second dwell and the subsequent ramp-down stage. For this test a moderate loading rate of 0.6 mm/min was used. Alternatively, the Type B test involved a three stage ramp-up and a faster loading rate of 0.2 mm/s. During this test, displacement was increased to three successive magnitudes (1.0 mm, 2.0 mm and 2.5 mm) and held constant for 45 s at each level. The specimen was then unloaded at the same rate.

The ramp-up and ramp-down segments of Type A tests are depicted in Figure 46. These plots show that FBG data correlated well with the strain gage data at RT as wells as at 205°C. Strain measurements calculated based on the FBG wavelength were within 5% of the strain gage values. This discrepancy is due to the possible temperature variation in the gage section of a specimen ($\pm$2°C) or a minor misalignment between the SG and the FBG.

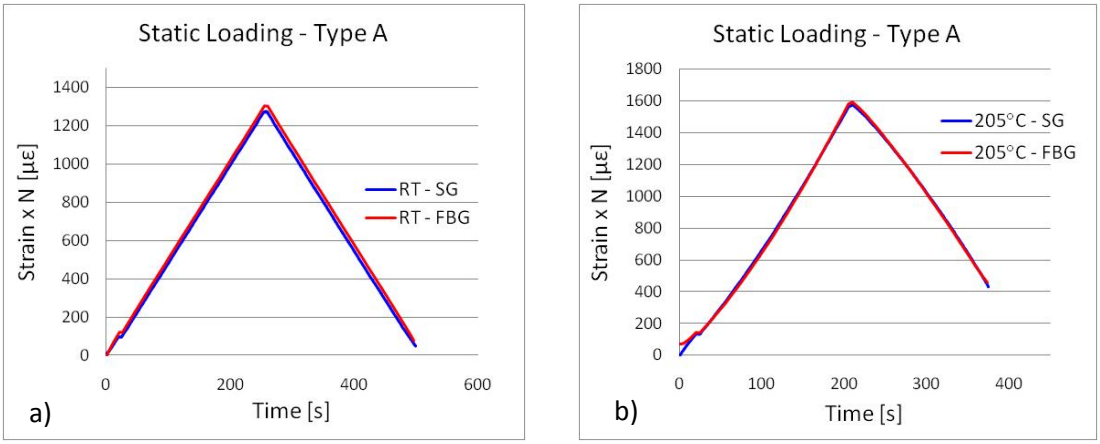

Figure 46: Strain data recorded with FBGs and strain gages (SG) during the Type A static tests at a) RT and b) 205°C.

Moreover, comparison of Figure 46a and b highlights an interesting difference between the ET and RT results. Strain ramp-up was linear at RT (Figure 46a) as it was expected to be since the test was ran in displacement control. However, the strain ramp-up at ET was non-linear (Figure 46b). This raises a question of whether or not this graph depicts the actual behavior of the specimen. It is possible that the strain and total elongation (displacement) of the specimen were not linearly related, because different parts of the specimen were subjected to different temperatures and exhibited different mechanical

properties and levels of viscoelasticity. Alternatively, the non-linearity of the graph could signify an error in the strain transmission through the adhesive layers. For future tests a high temperature extensometer will be used as an additional source of data for calibration. Its application would bypass the errors associated with the use of an adhesive.

An example of strain and force data recorded during a Type B test is presented in Figure 47a. It is evident that during each dwell interval, the specimen experienced stress-relaxation, and the force required to maintain a constant displacement decreased. An alternative force vs. strain plot is given in Figure 47b. Each jump or kink in this plot corresponds to the dwell interval and clearly depicts the drop in force for a given constant strain (displacement) value. These results portray the time-dependent properties of the tested specimens. Furthermore, Figure 48 compares strain measurements obtained with a strain gage (SG) and an FBG sensor during a Type B test at RT and 105°C. Once again it is evident that at ET, strain was not linearly related to displacement. During the constant displacement dwell, strain increased slightly. Nonetheless, FBG measurements were in agreement with strain gage data. Overall, a good correlation between the SG and the FBG data was obtained from the tests that were performed at different loading rates. This demonstrates the usability of FBGs for strain monitoring of PMCs that exhibit a time-dependent response.

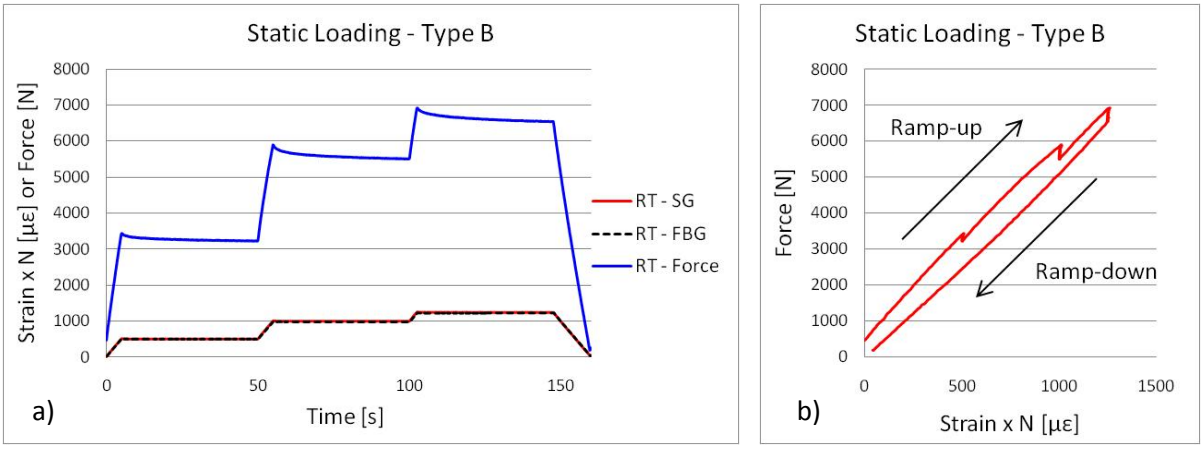

Figure 47: Strain and force data recorded during the Type B static test at RT. The graphs depict a) strain and force data vs. time and b) the force vs. strain curve.

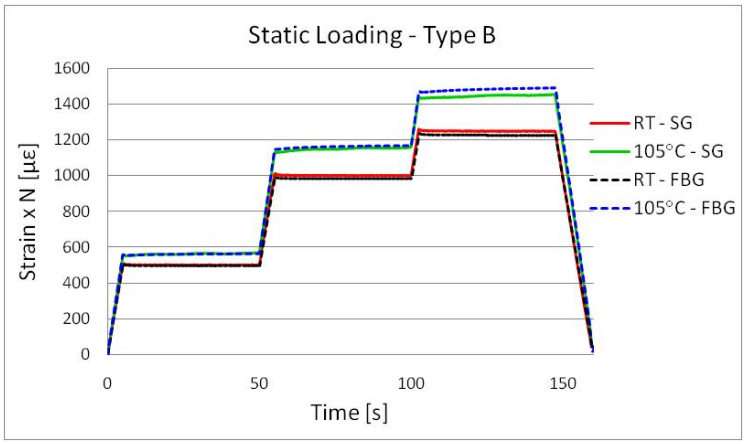

Figure 48: Strain and force data recorded during the Type B static tests at a) RT and b) 105°C.

Finally, the summary of static tests presented in Figure 49 clearly illustrates the influence of temperature on the stress-strain behavior of specimens. It shows that with an increase in temperature, the stiffness of the specimen decreased and the hysteresis loop widened. This dependence on temperature is well reported in literature for off-axis PMCs and is said to signify that material properties are matrix-dominated [21, 34, 38].

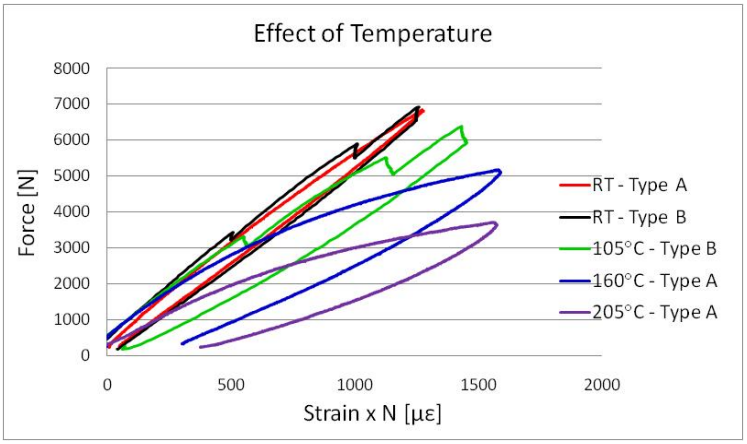

Figure 49: Effect of temperature on the force vs. strain response of tested specimens.

5.4 Fracture Mechanisms

Off-axis laminates demonstrated an intriguing failure mechanism that was influenced by the test temperature and the type of loading. This section will summarize the results of damage analysis at the macroscopic (e.g. fracture surface) and microscopic levels (e.g. cross-section).

5.4.1 Macroscopic Observations – Fracture Surfaces

Chapter 4 identified the main failure mechanism that accompanied fatigue fracture of [0#90]s woven laminates. These laminates experienced extensive delamination and fiber failure that happened along the 90^{o} weft bundles. The current section will aim to discuss the fracture characteristics of the off-axis specimens which were drastically different from those of the on-axis laminates. Prior to failure the off-axis specimens underwent significant elongation and exhibited deformation that resembled necking of metallic materials. As previously explained by Fouinneteau *et al.* [3], necking of PMCs is facilitated by the scissoring mechanism that occurs when the fiber and matrix begin to debond and separate, hence allowing the fiber bundles to re-orient towards the axial direction. Figure 50 shows the fracture surfaces of specimens fatigued at RT, 105^{o}C and 205^{o}C. Overall, the fracture morphology was "brushy" and fiber failure occurred along the +45^{o}/-45^{o} bundles. Similar results were reported by Kawai *et al.* [19] in relation to fatigue failure of off-axis plain woven laminates at RT and ET.

Magnified images of the specimen surface, taken close to the site of failure, revealed many loose pieces of the matrix material and debonding among the fiber bundles, Figure 51. This demonstrates the presence of fiber-matrix interface failure. In Figure 50c it is evident that the area affected by necking was significantly larger in the case of 205^{o}C test temperature than in case of lower temperatures. In fact, at elevated temperatures the matrix becomes more ductile and the adhesion between the two constituents weakens [6, 22]. Both these events would give fiber bundles more freedom to straighten out and rotate towards the longitudinal direction. Weakening (i.e. strength degradation) of the specimens due to thermal effects is further supported by the fact that at ET specimens failed after a fewer number of fatigue cycles than at RT.

However, in contrast to fatigued specimens, the statically broken specimen at RT did not exhibit necking and fractured along the 45^{o} line (i.e. not ± 45^{o}), Figure 52. Similar results were obtained with RT static tests by Kawai *et al.* [19]. It can be concluded that failure of the fiber-matrix interface is induced by cyclic loading and is accelerated by thermal effects. The discussion of failure mechanisms will be further continued in the next section by taking a closer look at the initiation and the propagation of damage.

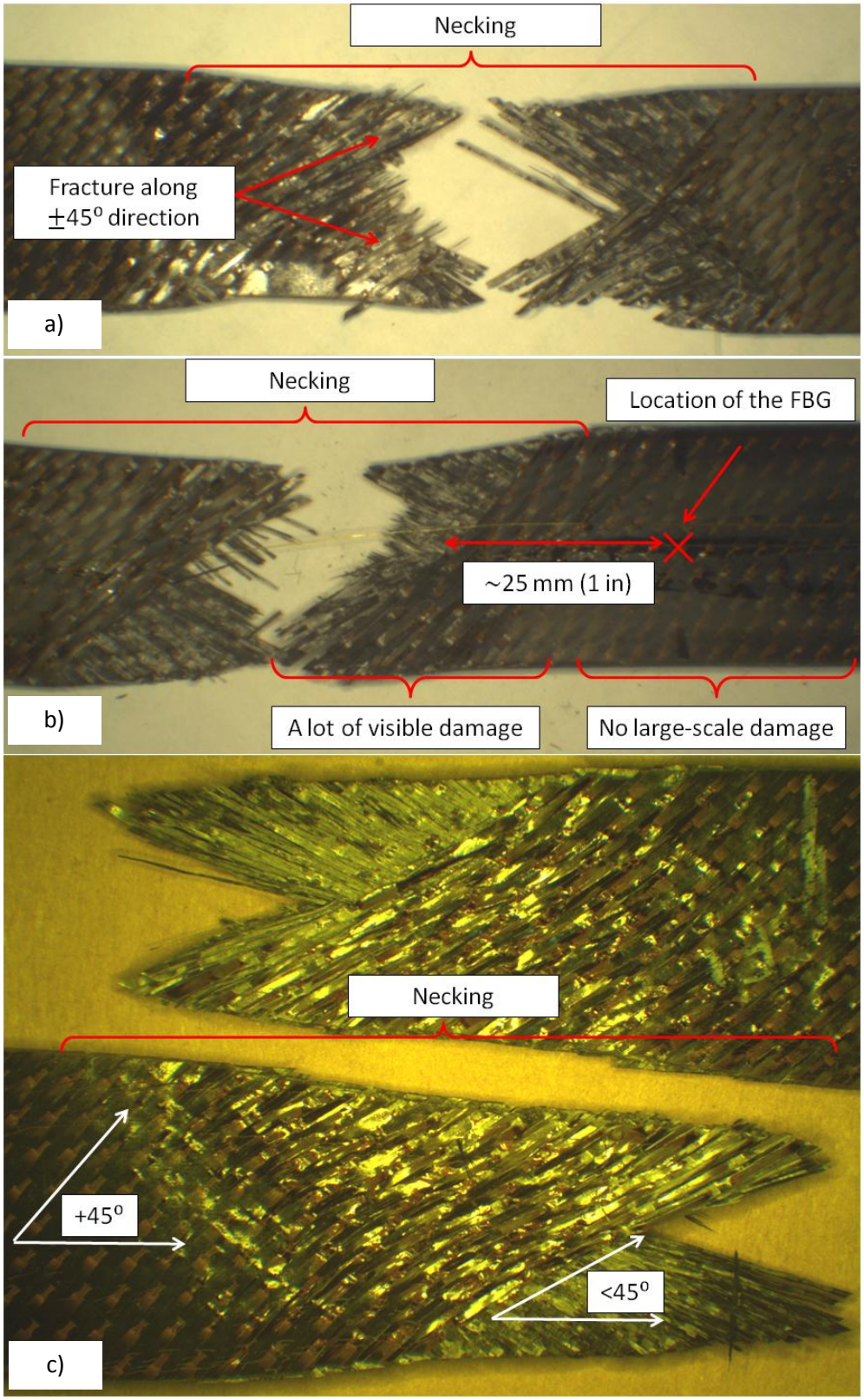

Figure 50: Fracture surface of specimens fatigued at a) RT, b) 105°C and c) 205°C.

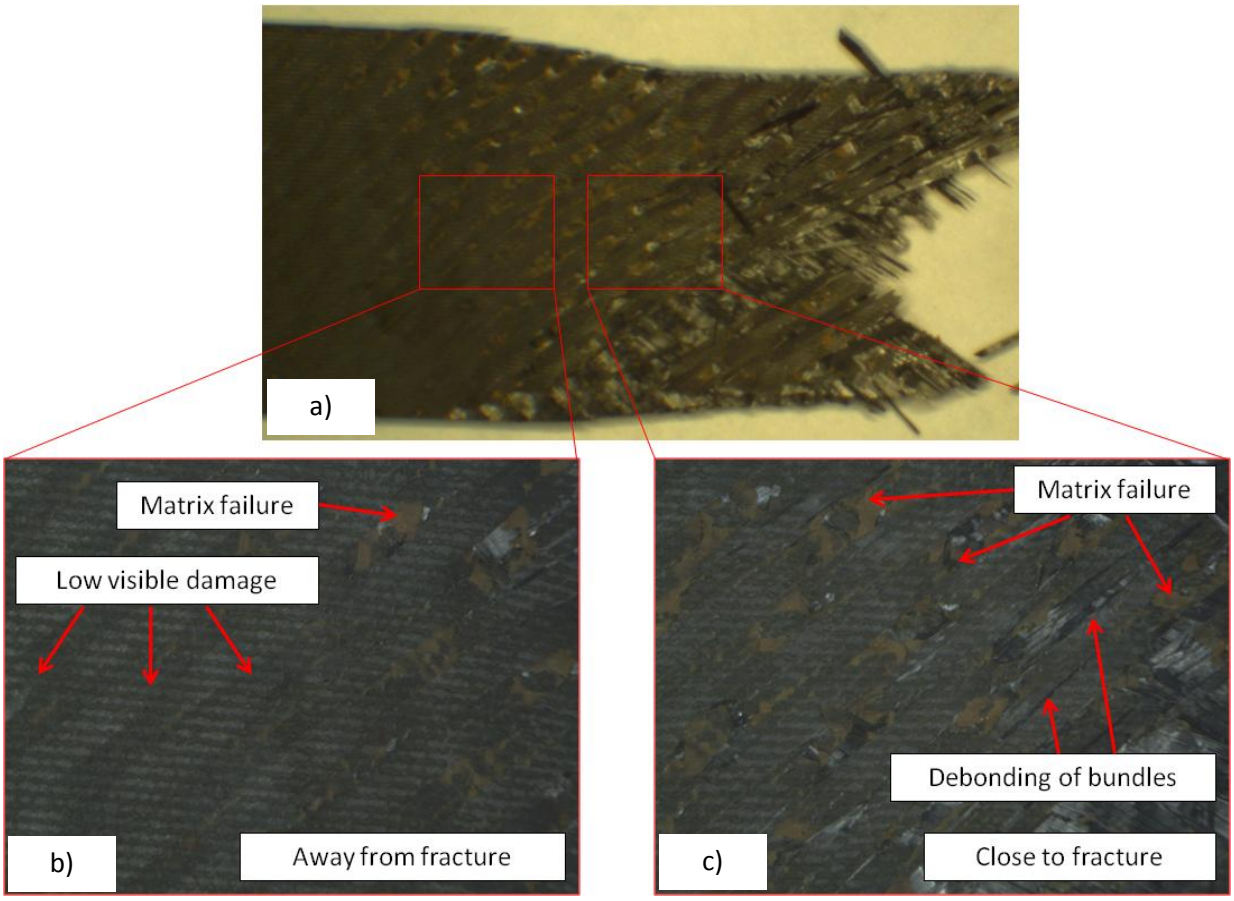

Figure 51: Images illustrating a) the fracture surface, and magnified regions captured b) away from the fracture surface and c) close to it. These images show the specimen fatigued at RT.

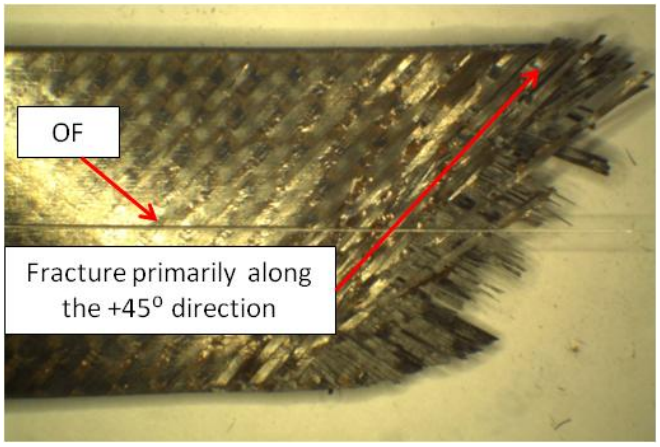

Figure 52: Fracture surface of a specimen that was statically loaded to failure at RT.

5.4.2 Microscopic Observation – Cross-Sectional Areas

To investigate the microscopic nature of damage initiation and propagation in the off-axis woven PMCs, the cross-sectional areas and surfaces of the specimens were studied under SEM. Cross-sectional images that were taken close to the site of final failure showed a significant amount of transverse cracks in the fiber bundles as well as debonding and delamination, Figure 53a. However, samples taken from the non-failed specimens or from failed specimens but farther away from the fracture exhibited a significantly lower amount of damage, Figure 53b. Hence specimens seem to have developed the critical amount of damage in a localized region just prior to failure. Additional images of the high-damage (Figure B2) and low-damage (Figure B3 and Figure B4) areas can be found in Appendix - B.

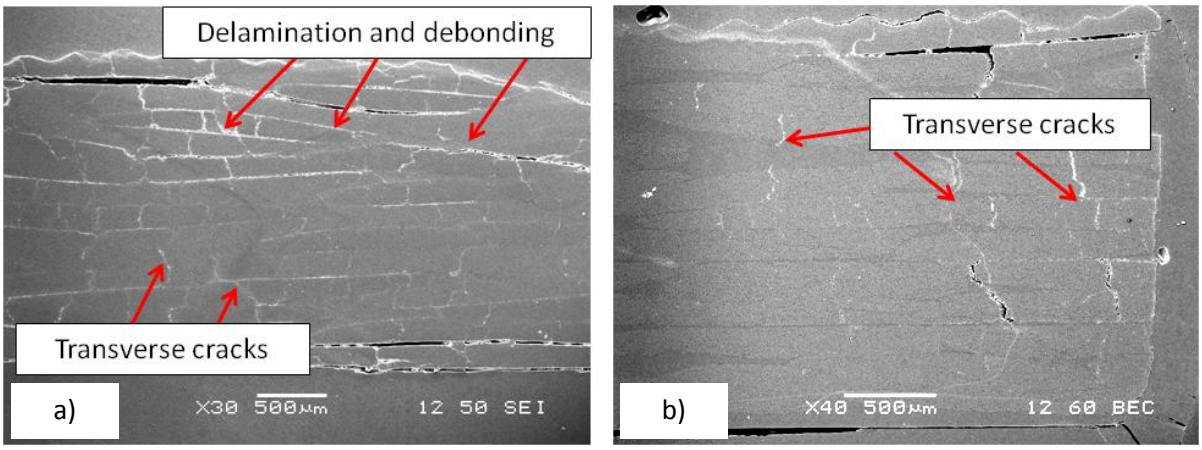

Figure 53: Cross-sectional images of samples taken from a) a high-damage and b) a low-damage areas.

Further comparison of samples taken from low-damage areas to those from high-damage areas helped gain insights into the sequence of damage development. SEM observations of low-damage samples detected a lower number of transverse bundle cracks and infrequent sites of debonding or delamination. However, from these images it was difficult to differentiate debonding from delamination, Figure 54a. This difficulty was associated with the fact that the warp and the weft bundles looked identical in cross-sections cut at a 90^{o} angle to the loading direction. It was hard to determine whether an interface crack was propagating between two bundles of the same ply (debonding) or different plies (delamination). To address this problem, an additional specimen was cut at a 45^{o} angle to the loading direction. Figure 54b illustrates that at this cut angle the architecture of the sample is revealed. Analysis of this sample concluded that bundles corresponding to the same ply were in fact debonding, but plies were not yet delaminating.

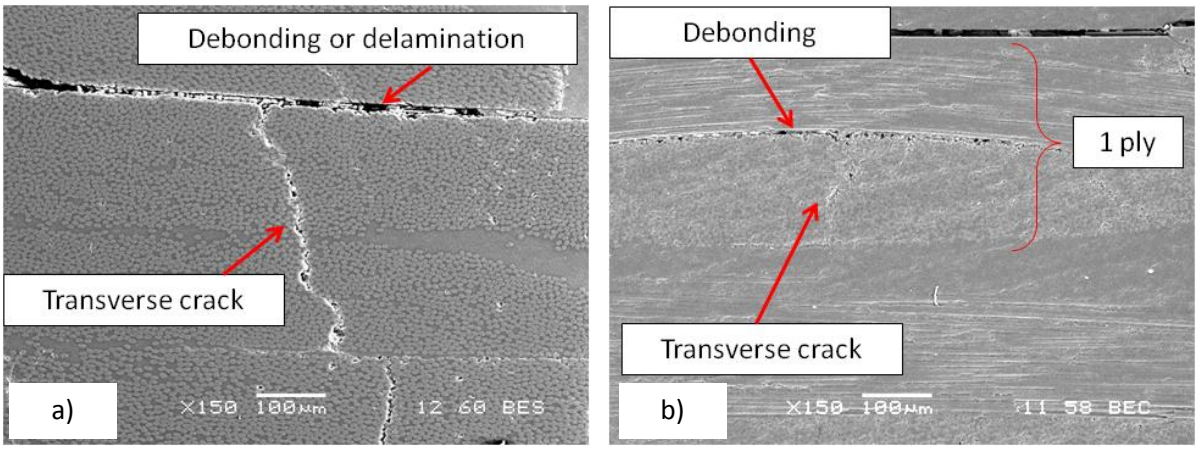

Figure 54: Debonding within a ply and transverse bundle cracks observed in samples cut at a) 90° and b) 45° angles.

Figure 55 also captures the interaction between matrix cracks, transverse bundle cracks and debonding. Matrix cracks seem to have adjoined transverse cracks that had propagated in the bundles oriented in the same direction. Similarly, debonding between the bundles appears to co-exist with the transverse cracks in these bundles. This view shows that transverse cracks were arrested as they reached a bundle oriented in a different direction. However, in a 90° view, as shown in Figure 54a, transverse cracks that extended through the thickness of two or three bundles were detected. It seems that transverse cracks in certain locations could propagate through the thickness of multiple bundles and then continue to grow along the fiber direction within the different bundles.

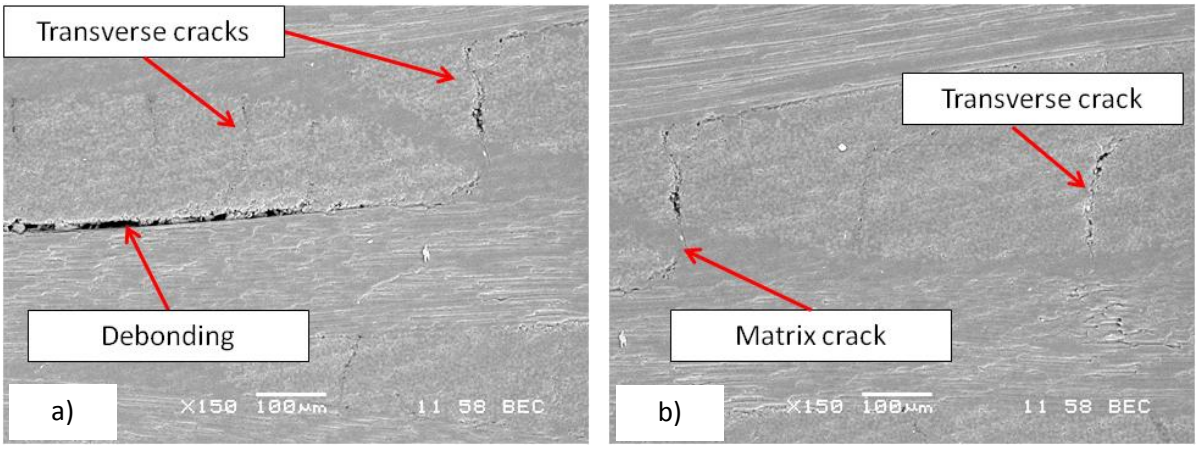

Figure 55: Debonding, transverse cracks and matrix cracks observed in the 45° sample.

Overall, based on the cross-sectional analysis, all specimens demonstrated the same pattern of damage development regardless of the loading type and test temperature. Characterization of damage development can be furthered by examining the specimen surfaces.

5.4.3 Microscopic Observation – Surface Areas

The pattern of crack formation typically observed on the surface of the specimen is shown in Figure 56. On the surface numerous cracks propagated along the fibers at a 45° angle to the loading directions, and matrix cracks formed in resin rich areas at a 90° angle, as shown in Figure 56. It appears that matrix cracks arranged themselves in the direction of the transverse bundle cracks. The pattern of cracks in Figure 56b also suggests of the alignment of matrix cracks with the submerged (or underlying) cracks in weft and warp bundles. The effect of fibers on the growth of a matrix crack is clearly depicted in Figure 57, which shows propagation of a matrix crack impeded by the presence of fibers. In the vicinity of a fiber bundle, matrix cracks were re-directed to grow along the fiber direction. Also, an interesting zig-zag pattern was observed in the region where a bundle crack transitions into the formation of matrix cracks, Figure 58. Additional images can be found in Appendix - B (Figure B5 – Figure B7).

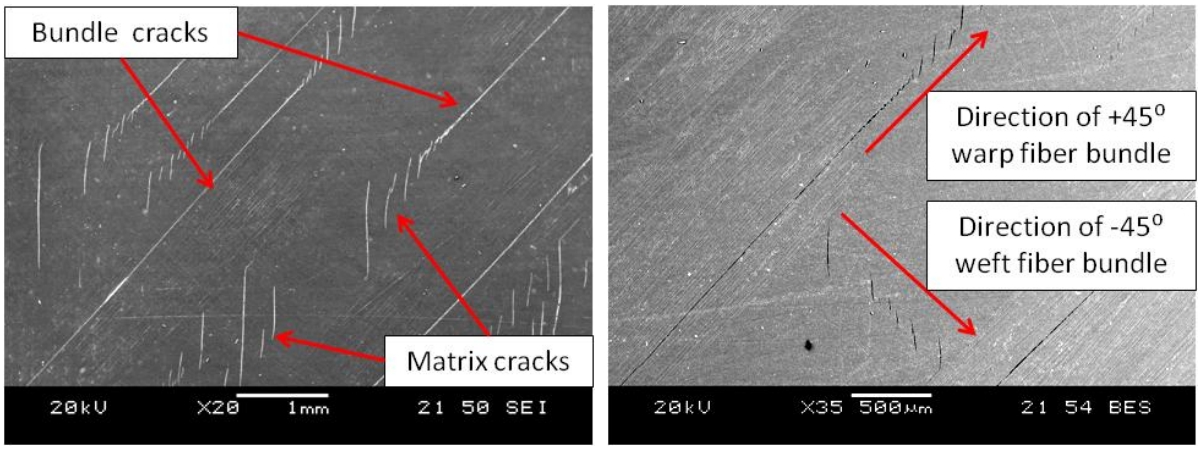

Figure 56: General pattern of bundle cracks and matrix cracks formed on the specimen surface.

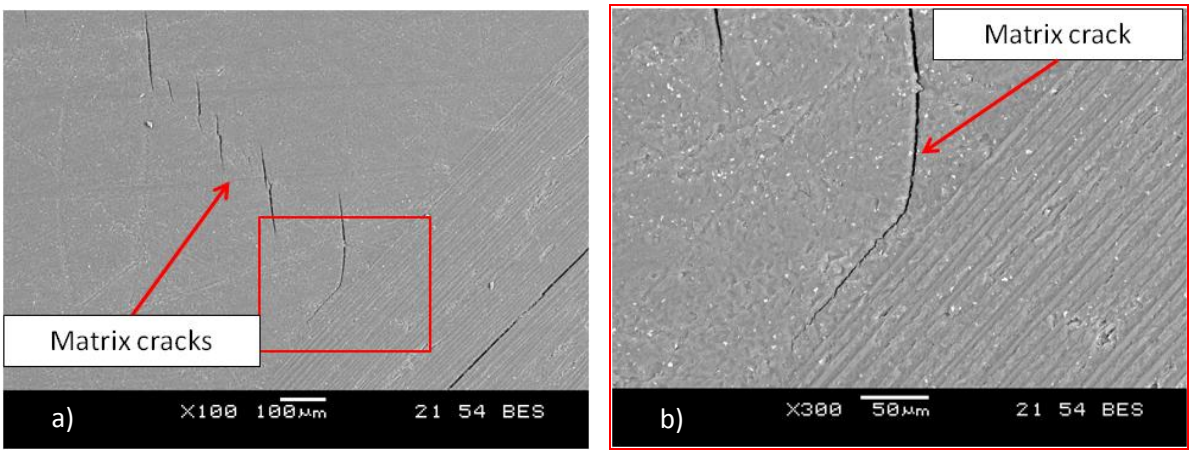

Figure 57: Matrix crack that is re-directed when it encounters fibers. Images were captured at a) x100 and b) x300.

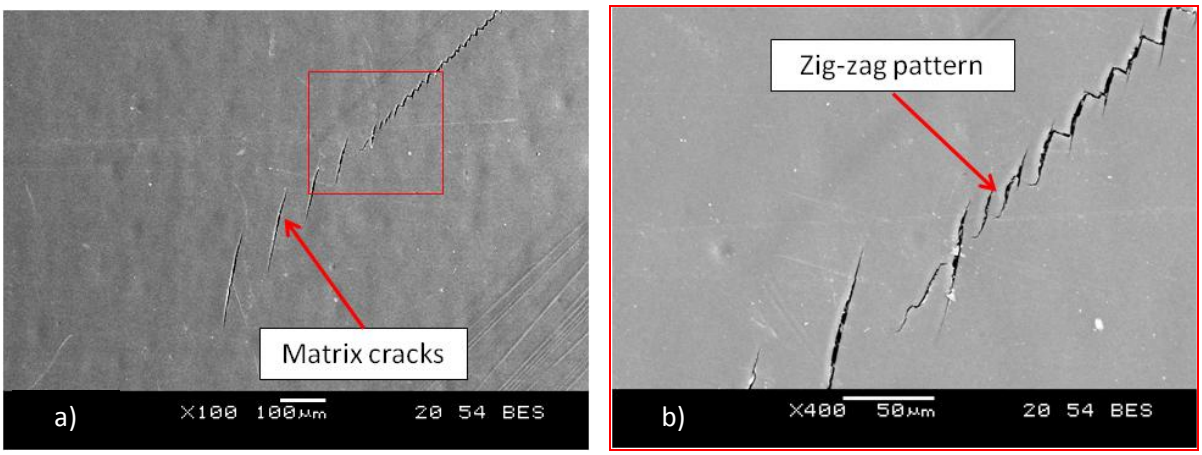

Figure 58: Zig-zag pattern formed by cracks as they transition from the fiber bundle to the matrix area. Images were captured at a) x100 and b) x400.

This general pattern of crack formation was observed in all specimens. However, an interesting difference in surface smoothness was observed between specimens tested at RT and ET, as depicted in Figure 59. In the case of RT specimens, the surface of the matrix was smooth (Figure 59a). On the contrary, the surface of the ET specimens was not smooth and showed signs of matrix deformation (Figure 59b) that might have occurred due to the increased plasticity or ductility of the BMI resin at ET. Moreover, the fracture morphology of the transverse bundle cracks was also affected by temperature. Figure 59a shows that bundle cracks in RT specimens had rugged sides, hence signifying brittle fracture. Fracture sides in ET specimens had smooth surfaces (Figure 59b) which probably formed as a result of fiber-matrix interface weakening and failure at ET. Additional images comparing the surfaces of RT (Figure B8) and ET (Figure B9) specimens can be found in Appendix - B. Finally, matrix cracks in the specimen fatigued at 205^{o}C did not propagate at a 90^{o} angle; instead they continued to grow in the direction of bundle cracks (45^{o}), Figure 60. This dependence of the matrix related failures on the test temperature is anticipated. It was previously reported that resins that are brittle at RT begin to exhibit more ductile properties at ET [22]. Results thus far exemplify that the test temperature has a definite effect on damage formation and growth in PMCs.

In conclusion, the reader is referred to Figure 61. This figure captures propagation of transverse bundle cracks across the area, which is indicated by the glue line, where an OF was bonded. Hence the FBG was exposed to strain non-uniformity created by surface cracks and its spectrum was expected to chirp. The following section will continue to discuss damage formation of PMCs and present the results of damage monitoring with FBGs.

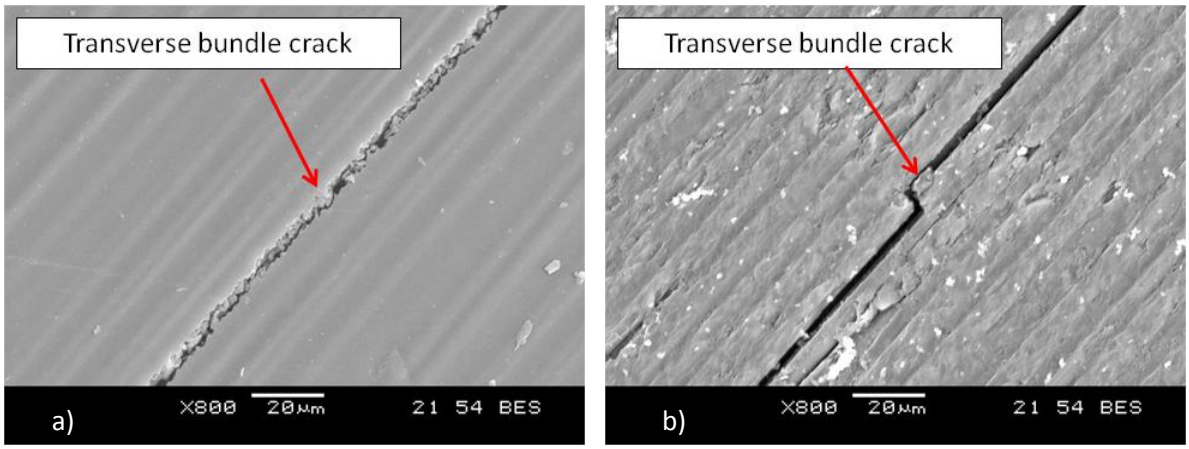

Figure 59: Surface of the specimens fatigued at a) RT and b) ET.

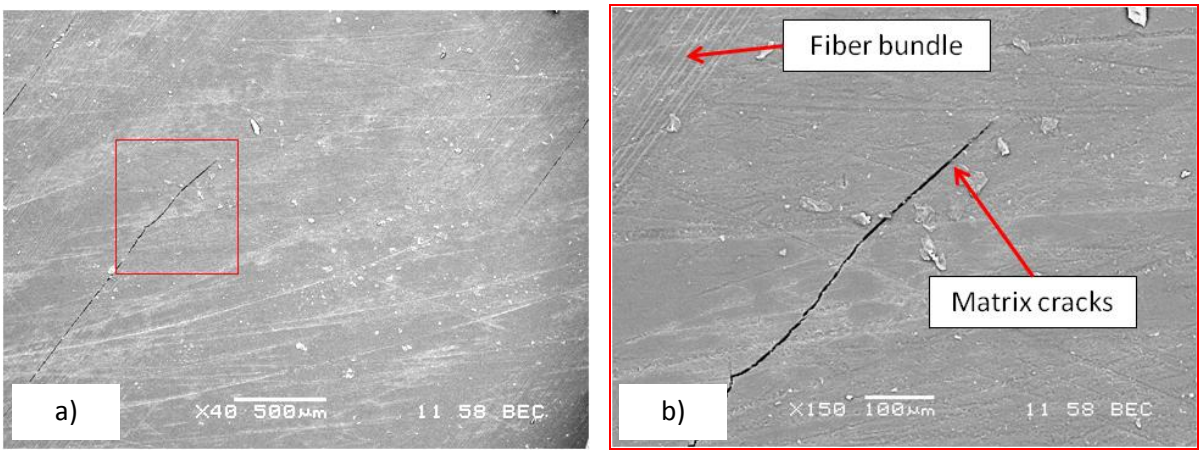

Figure 60: Matrix crack formation on the surface of the specimen tested at 205°C. These images were captured at a) x40 and b) x150.

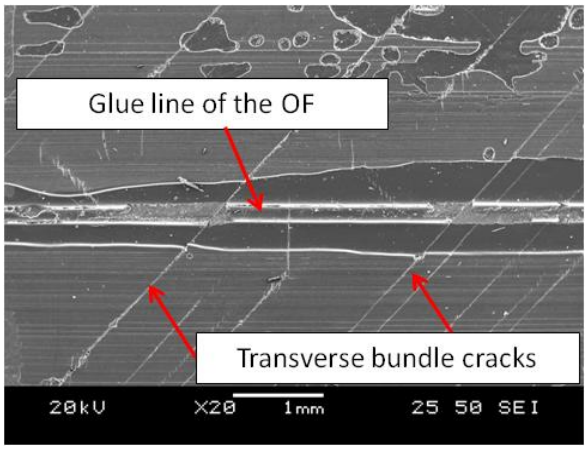

Figure 61: Transverse bundle cracks passing through the location of the OF.

5.5 Monitoring Damage Evolution

Previous studies have shown that FBG sensors have the potential to be utilized for damage monitoring as they are sensitive to non-uniform strain fields created by the presence of damage [15-18, 67–76]. The aim of this section is to correlate the spectral changes experienced by the FBG sensors during fatigue to the damage mechanism characteristic of off-axis woven specimens. The differences between the spectra of fully bonded and partially bonded FBGs will also be presented. Due to the proprietary nature of these specimens, the number of cycles was scaled by a factor **N**.

5.5.1 Fully vs. Partially Bonded FBGs

The goal of the application of partially bonded FBGs is to avoid chirping of the spectra while capturing the strain or temperature measurements. Both partially bonded (PB) and fully bonded (FB) FBGs were used with specimens tested in fatigue at 105°C, 160°C and 205°C. Figure 62 clearly illustrates that with an increasing number of cycles, the loading spectra of a fully bonded FBG have chirped, widened, and dropped in intensity. The slight chirping of the spectrum can be attributed to the formation of bundle cracks and matrix cracks on the surface of the specimen. On the contrary, the spectra of a partially bonded FBG remained essentially unchanged and the sensor behaved like an extensometer. Further comparison of the strain measurements with the two sensors will be discussed in Section 5.6.2.

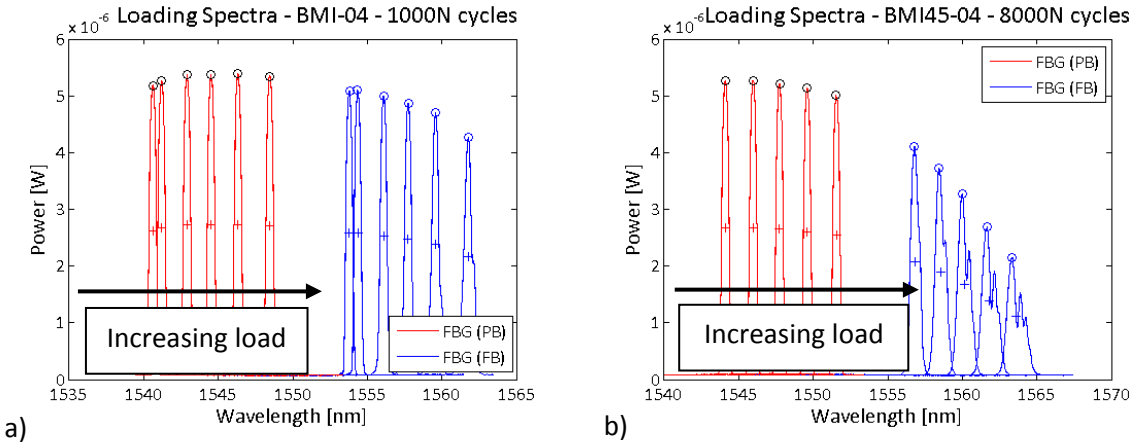

Figure 62: Comparison between the spectra of a fully bonded (FB) and a partially bonded (PB) FBG recorded at a) 1,000N cycles and b) 8,000N cycles.

An interesting functional difference between the partially and the fully bonded FBGs is the ability of the latter to signal the onset of debonding. For instance, Figure 63 shows that when a fully bonded FBG began to debond, the spectrum split into two parts (Figure 63a) and with the progression of fatigue, the

peak corresponding to the debonded portion became larger than that corresponding to the bonded portion (Figure 63b). This property of a fully bonded FBG is advantageous since it can signal a problem with the adhesion integrity of the sensor which can then be fixed (i.e. an FBG can be re-bonded). Conversely, failure of a partially bonded FBG would be abrupt. However, in order to observe this type of a spectral change, the FBG would have to be debonding from a free (or loose) end. In order words, if the FBG starts to debond somewhere along the length of the grating when the ends are still bonded, it is hard to predict what the resultant spectrum would be.

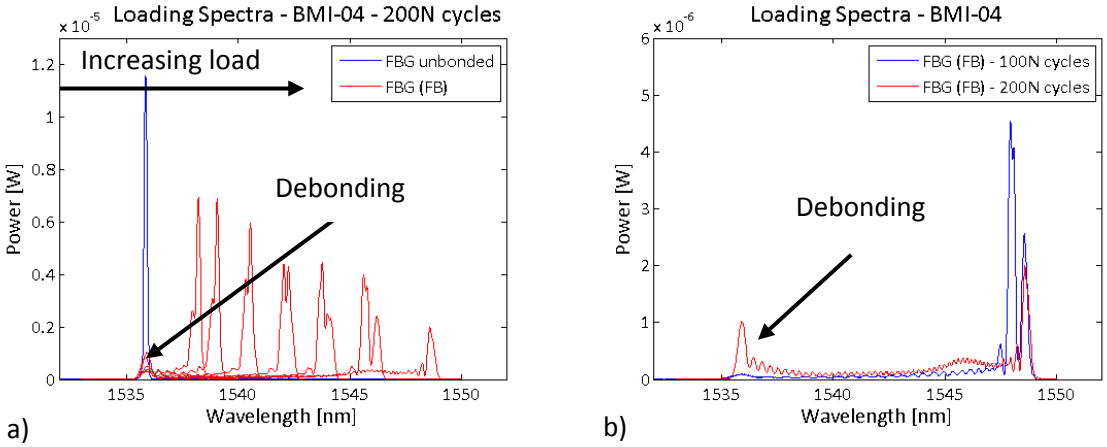

Figure 63: Comparison between a) the loading spectra of the FB FBG when it began to debond and the spectrum of that same FBG prior to bonding, and b) the loading spectra of the FB FBG after 100N and 200N cycles.

Overall, as it was anticipated the partially bonded FBGs are insensitive to damage formation, whereas the fully bonded ones seem to react to it. The next section will discuss spectral changes detected in this study and will aim to explain their contributing factors.

5.5.2 FBG Spectral Analysis

SEM analysis presented in Sections 5.4.2 and 5.4.3 have shown that the type of damage observed among the different specimens was similar. The evolution of the FBG loading spectra during fatigue was expected to be analogous for all specimens as was the case with the on-axis woven specimens, which were discussed in Chapter 4. However, in the case of off-axis specimens the general shapes of the FBG loading spectra recorded for different specimens were somewhat inconsistent. For instance, specimen BMI-02 showed no chirping even after 40,000N cycles (Figure 64a), while specimens BMI-04 and BMI-05 showed some chirping (Figure 62, Figure 64b) and specimen BMI-06 showed extensive chirping with a skewed bell shape of the curve (Figure 65). Hence it can be hypothesized that in certain cases

mechanisms other than damage initiation were responsible for these spectral changes, for instance, debonding of the FBG.

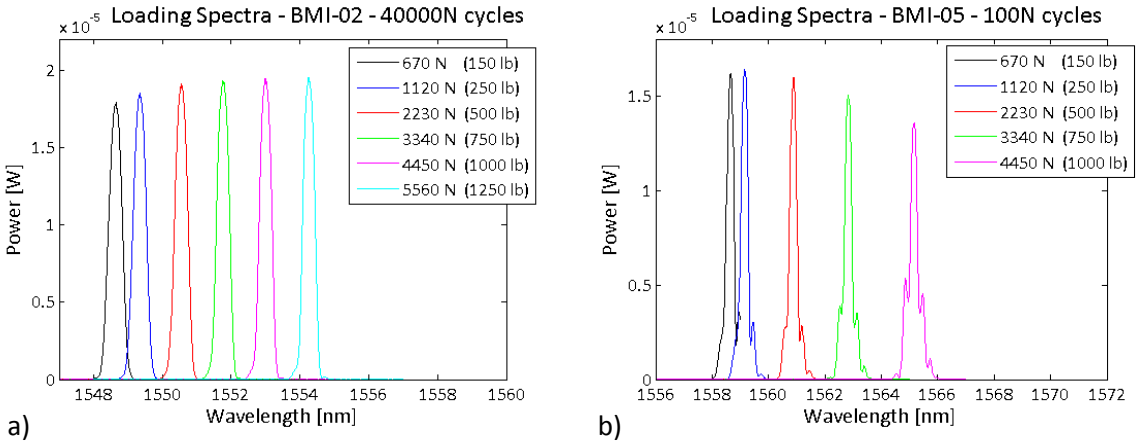

Figure 64: FBG loading spectra recorded with a) BMI-02 after 40,000N cycles and b) BMI-05 after 100N cycles.

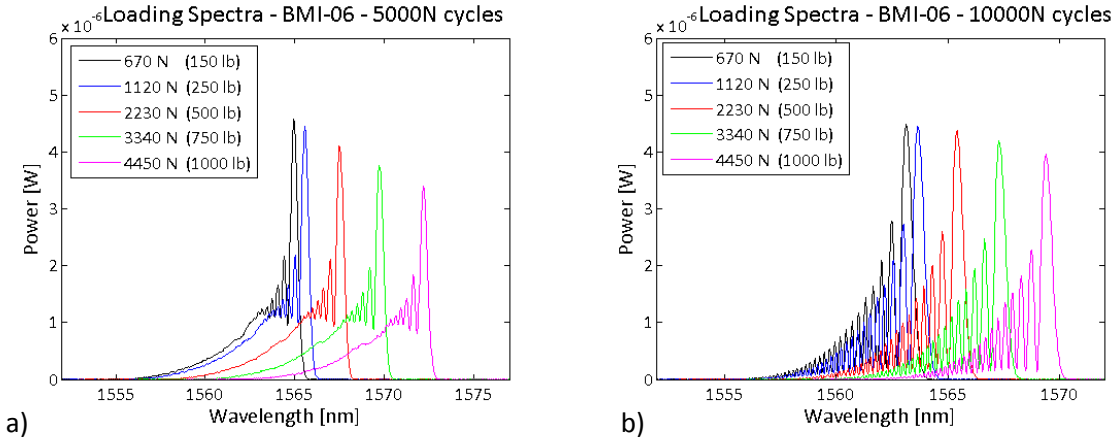

Figure 65: FBG loading spectra recorded with BMI-06 after a) 5,000N cycles and b) 10,000N cycles.

The spectra of the fully bonded FBG recorded from BMI-04 and BMI-05 exhibited slight chirping. This type of chirping can be attributed to the presence of matrix and bundle cracks on the surface of the specimen (Figure 61) that creates local strain non-uniformity. In the case of BMI-04, the FBG lasted until the end of the test and the spectrum did not undergo any noteworthy changes. In the case of BMI-05 the FBG unfortunately failed after 100N cycles.

In contrast to BMI-04 (105^{o}C) and BMI-05 (160^{o}C), the loading spectrum of BMI45-02 (RT) did not chirp during the entire fatigue test while this specimen had definitely developed matrix and bundle cracks, as was shown by SEM analysis. A possible explanation for this difference is the fact that different adhesives

were used for these specimens due to the different test temperature. Moreover, these adhesives called for different application and cure procedures. In the case of the RT specimen more adhesive was applied and pressure was not used. With the ET specimens only a thin layer of the adhesive was used and pressure was applied during cure. Therefore, the adhesive layer was probably thicker in the case of the RT specimen and it absorbed the slight strain non-uniformity created by cracks. Hence the FBG spectrum did not chirp. However, the author does acknowledge the fact that an alternative explanation might exist.

The fact that the loading spectra of the aforementioned fully bonded FBGs did not exhibit any concrete changes during the test can be attributed to the fact that these specimens did not develop any major damage up to just before the failure. Additionally, most of the damage was concentrated in the vicinity of the fracture surface. It was noted that BMI-02 failed closer to the grips and BMI-04 failed about 25 mm [1 in] from the FBG (Figure 50b); hence both fractures happened relatively far away from the FBGs while the sensors remained unaffected by the onset of final failure. Previous studies suggested that surface mounted FBGs are not as sensitive to internal damage (e.g. delamination) as embedded sensors [62].

The FBG loading spectra that corresponded to BMI-06 possessed an intriguing shape which was different from other specimens, Figure 65. The spectrum had a skewed shape and experienced significant chirping after 10,000N cycles. At higher load values the interrogator detected more than 20 wavelengths. It is also interesting to note that distortion of the fully bonded FBG spectra coincided with the breakage of a partially bonded FBG that occurred close to the bonded portion of the OF during the initial static test, Figure 66. This suggests that the two events are co-related. Additionally, since SEM analysis demonstrated that specimens developed a minimal amount of damage during the early stages of fatigue, damage initiation taking place during the initial static test was not expected to cause distortion of the FBG spectrum. An alternative cause of this spectral change could be poor adhesion (or onset of debonding) between the FBG and the specimen.

The effect of the bond quality on the FBG spectrum can be further illustrated by the spectral results from the BMI-04 specimen. The first FBG that was bonded to the specimen experienced significant chirping and debonded after 200N cycles, as shown in Figure 63. A new FBG was then bonded onto the specimen and its signal was only slightly chirped during testing, as shown in Figure 62. Hence, chirping of the first FBG was not caused by crack formation but rather by a poor bond quality.

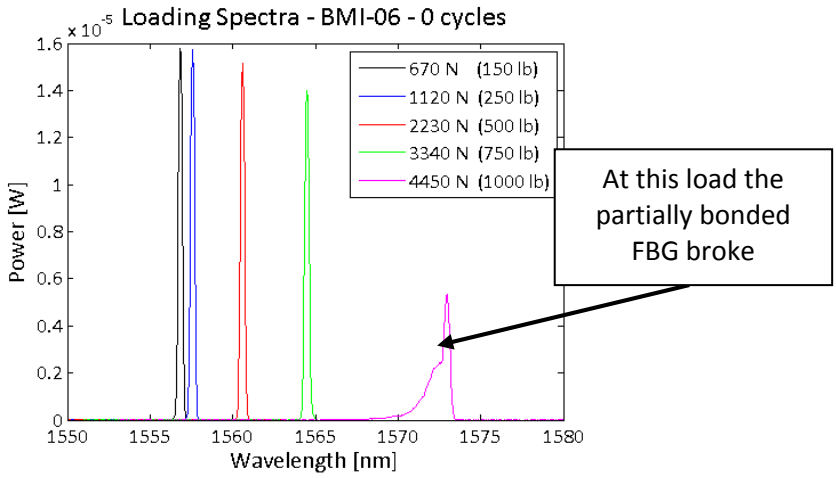

Figure 66: FBG loading spectra recorded with BMI-06 during the initial static test.

Results thus far indicate that surface bonded FBG are sensitive to strain non-uniformity, which might be caused by a number of factors including damage formation and adhesive failure (between the FBG and the sample). A couple of FBGs expressed excessive chirping that was linked to their poor adhesion to the specimens. The other FBGs exhibited only slight chirping that was probably caused by the matrix and bundle cracks which were detected on the surface of the specimen. Moreover, these FBGs did not undergo any identifiable spectral changes that could be linked to a new damage mechanism or to an approaching final failure. This response of the FBGs is understandable since specimens did not develop substantial damage until the final fracture; hence there was “nothing” for the FBGs to detect. Usability of FBGs for damage monitoring is directly related to the failure mechanism characteristic of a particular material. Overall, response of the FBG must be correlated against another method, such as SEM, in order to be meaningful.

5.6 Monitoring Stiffness Degradation

This section will discuss the general trends pertaining to the stiffness degradation of the BMI off-axis specimens during fatigue. The effect of temperature on the stress-strain curves will also be presented. Applicability of different sensors and the correlations among them will be discussed. Due to the proprietary nature of these specimens, the strain values and the number of cycles were scaled by a factor **N**.

5.6.1 Stress-Strain Curves

The typical evolution of a stress-strain response of an off-axis BMI specimen during cyclic loading is presented in Figure 67. Reduction of the fatigue modulus (F_1-F_4) during fatigue is clearly captured in Figure 67. It is evident that with an increasing number of cycles the stress-strain curve shifted in the direction of increasing strain. This behavior is known as strain ratcheting or cyclic creep and has been previously reported for polymers and PMCs [27–29]. As fatigue loading progressed, the ratcheting strain gradually reached a saturated value and the stress-strain curves became more linear. Further comparison between Figure 68a and b demonstrates a prominent influence of temperature on the fatigue behavior of these specimens. The amount of strain ratcheting was significantly higher with specimens tested at ET (Figure 68b (205°C) and Figure 69 (160°C)) than with the one tested at RT (Figure 68a). It is expected that an increase in temperature would amplify strain ratcheting since at ET mechanical properties of the matrix and the PMC degrade and become more time-dependent.

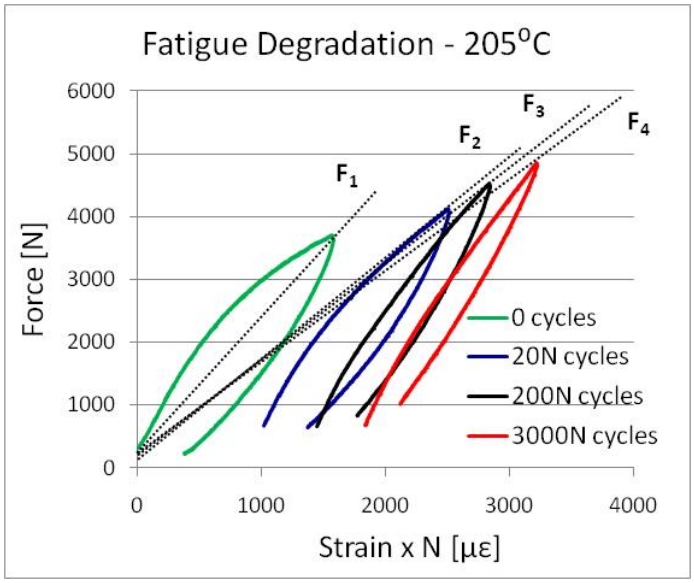

Figure 67: Fatigue modulus degradation of a specimen tested at 205°C.

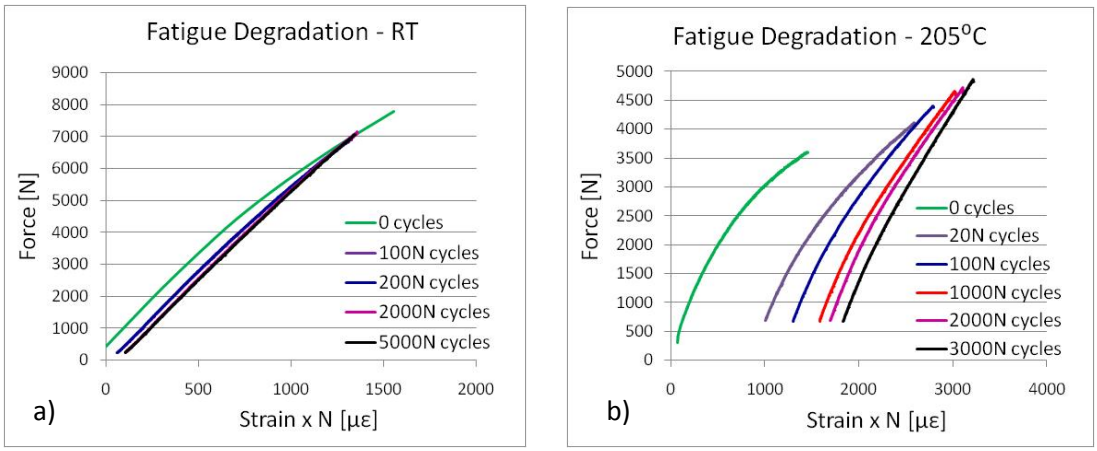

Figure 68: Comparison between the stress vs. strain response of specimens fatigued at a) RT and b) 205°C.

5.6.2 Comparison among Different Sensors

The preliminary results presented in Section 5.3 show a good correlation between the FBG and strain gage data. Similarly a good agreement was observed between the fatigue data obtained from the two sensors, as shown in Figure 69. The minor discrepancy between the FBG and stain gage values (<5%) was caused by the slight misalignment of the strain gage.

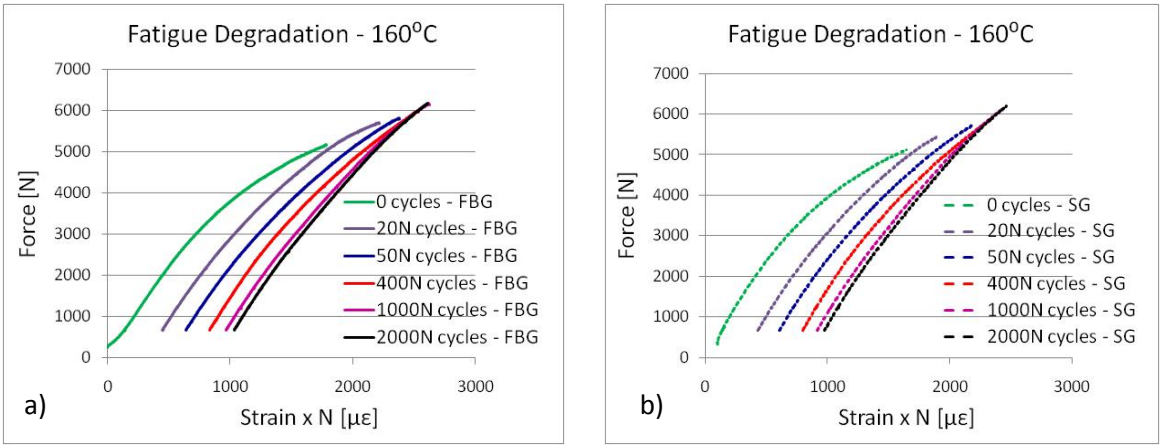

Figure 69: Comparison between data captured with a) a partially bonded FBG and b) a strain gage (SG). These graphs depict the evolution of the stress-strain response of the specimen during fatigued at 160°C.

With respect to the different bonding methods, both the partially and fully bonded FBGs demonstrated the ability to detect and quantify the change in the material stress-strain behavior during cyclic loading. An excellent correlation between the two sensors was attained, as shown in Figure 70. The main advantage of a partially bonded FBG over a fully bonded one is its natural immunity to chirping which

greatly simplifies data analysis. This is an important parameter to consider when dealing with specimens that develop a lot of damage, such as matrix cracks, during the early stage of static or dynamic testing.

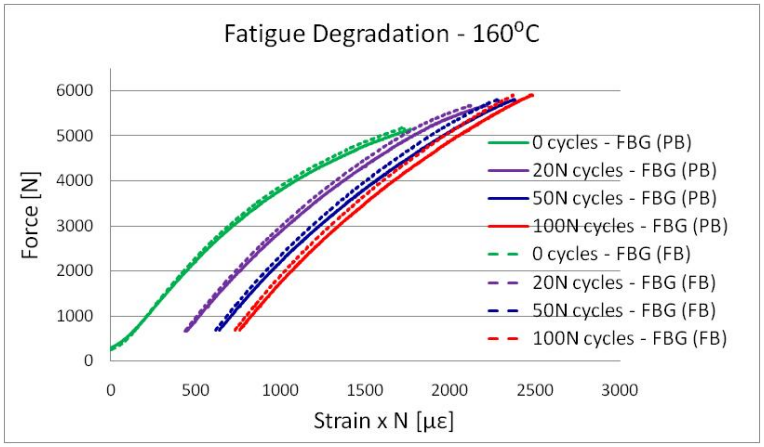

Figure 70: Comparison between data captured with partially bonded (PB) and fully bonded (FB) FBGs. These graphs depict the evolution of the stress-strain response of the specimen during fatigued at 160°C.

Moreover, with respect to in-situ stiffness monitoring, the cyclic data recorded with the interrogator provided excellent results. Figure 71 shows the correlation between the strain gage and FBG data obtained after 2,500 cycles. Analogous results were obtained with specimens tested at other temperatures. Hence FBGs show the potential to be used for in-situ stiffness monitoring when they do not chirp extensively.

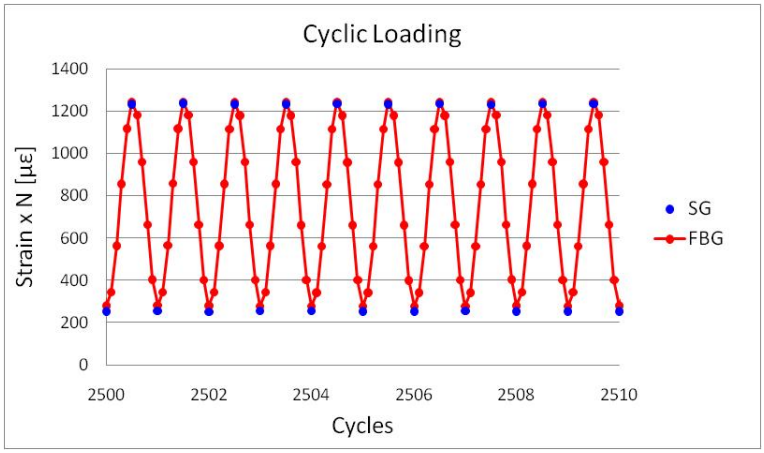

Figure 71: Strain data recorded with an FBG and a strain gage (SG) during cyclic loading at RT.

5.7 Concluding Remarks

In this study, surface mounted FBG were used for stiffness and damage monitoring for off-axis woven BMI specimens tested at room temperature (RT) and elevated temperatures (ET). Preliminary static tests have clearly displayed the influence of time and temperature on the material response to mechanical loading. With an increase in temperature specimens expressed a non-linear stress-strain behavior, underwent stress-relaxation during constant displacement loading, and experienced stiffness degradation. FBG data was shown to correlate well with the strain gage data for the different temperatures and loading rates considered.

Due to the woven architecture and the off-axis orientation, the specimens demonstrated a unique fracture mechanism. These specimens underwent significant elongation prior to failure and experienced necking during cyclic loading. The presence of necking in PMCs is associated with failure of the fiber-matrix interface and the matrix; these failures allow fiber bundles to rotate from a 45^{o} to a shallower angle with respect to the loading direction. The subsequent SEM analysis of surfaces and cross-sectional areas captured cracks propagating in the matrix and along the fibers as well as some occurrences of debonding and delamination. Fracture mechanisms were similar among the different specimens and some differences were associated with thermal effects. Comparison between failed and non-failed specimens indicated that the majority of the damage developed prior to failure.

In order to evaluate the applicability of FBGs for damage monitoring, microscopic observations of damage development in these specimens were correlated with results from the FBG spectral analysis. FBGs have shown slight chirping that was presumably caused by the presence of matrix and bundle cracks on the surface of the specimen. In the case of damage monitoring, no major changes of the spectrum, which could have been related to a tangible change in the specimen damage state, were observed. Such results can be explained by the fact that specimens developed relatively low amount of damage with the exception of the area around the fracture zone. Since fracture occurred relatively far from the FBGs, they did not react to it. When considering utilization of FBGs for damage monitoring, the prevalent damage mechanism in that material as well as the location or positioning of the FBG(s) should be taken into account. If the material develops minimal damage or the FBG is located far from the epicenter (e.g. delamination of central plies vs. surface bonded FBG), the sensor might be insensitive to damage initiation and propagation.

On the contrary, some FBGs have exhibited significant chirping. However, further analysis of the spectral shapes and the assessment of the specimen damage state suggested that distortion of the spectrum was

not a reflection of damage. It is proposed that poor quality of the bond between the FBG and the specimen has resulted in distortion of the FBG signal. Additional specimens would have to be tested in order to uphold or dismiss this hypothesis. These results emphasize that a careful assessment of the damage state of the specimen must be conducted prior to reaching a verdict on the cause of spectral chirping or change.

During fatigue loading the specimens have demonstrated strain ratcheting. The degree of ratcheting increased with temperature due to degradation of mechanical properties of the BMI matrix. Overall, FBG data correlated well with the strain gage data at RT and ET. Strain measurements obtained with fully bonded and partially bonded FBGs were also in agreement. The use of partially bonded FBGs is advantageous if a specimen is expected to develop a significant amount of damage that creates chirping of a fully bonded sensor.

Overall, FBGs show their usability for strain or stiffness monitoring of PMCs at ET. However, their ability to provide useful information regarding the damage state of the material is strongly related on their location and failure mechanism of the substrate material.

6 Discussion and Recommendations

Fiber Bragg grating sensors are perceived as attractive means for strain and damage monitoring of specimens during mechanical testing as well as for health monitoring of in-service components [12-18, 67-76]. The experimental programs conducted as a part of this thesis further investigated applicability of surface bonded and embedded FBGs for stiffness and damage monitoring of woven PMCs during tension-tension fatigue loading at different temperatures. However, certain limitations pertaining to their use exist and have to be considered for future implementations. This chapter will merge the results of the two experimental programs and will propose recommendations for application of FBG sensors for strain and damage monitoring of woven laminates.

6.1 Strain Measurement

Results of both experimental programs showed that FBG sensors can be used for strain and stiffness monitoring. However, if the specimen is heavily damaged (Chapter 4), chirping of the FBG spectra will be substantial and will complicate data analysis. When dealing with a chirped spectrum it is advisable to use an effective Bragg wavelength instead of a peak Bragg wavelength for strain calculations, as it was discussed in Section 4.2.3. Moreover, partially bonded FBG sensors are recommended for use with specimens that are expected to exhibit strong strain non-uniformities that lead to a distortion of a fully bonded FBG spectrum. Under these conditions, partially bonded FBGs offer a particular advantage over the fully bonded ones as they are not susceptible to chirping and can be utilized without complicating data analysis and compromising the validity of strain measurements. In Section 5.6.2 a good agreement was shown between the strain measurements obtained with fully and partially bonded FBGs. It should be noted that partially bonded FBGs cannot be used for compression testing.

6.2 Damage Monitoring

By monitoring the changes of the FBG spectra, it was possible to detect the transition between the different stages of damage development in carbon/epoxy on-axis specimens (Section 4.4). In the case of carbon/BMI off-axis specimens, FBG spectra were also representative of the damage state of the substrate; however, final fracture was localized and FBGs did not detect or signal it (Section 5.5). In general, to increase the sensitivity of an FBG sensor to damage development, the sensor should be placed as close to the expected site of damage development as possible. This point is especially important if damage is not evenly distributed throughout the specimen. Similarly, if damage

development in the material is not uniform, it is recommended to use a network of sensors in order to adequately map out damage distribution. In regards to damage monitoring, configuration and positioning of the FBG as well as the failure mechanism particular to that substrate have to be considered as these parameters will determine effectiveness of the sensors.

For damage monitoring, a possible alternative to a uniform FBG would be a chirped grating. In the case of a uniform FBG the pitch (or period) of the grating is constant, hence resulting in a single wavelength being reflected, refer to Figure 72a. On the other hand, in the chirped grating the period varies linearly along the length of the grating, resulting in a range of wavelengths being reflected, Figure 72b. In fact there is a direct relationship between the reflected wavelengths of the chirped spectrum and the locations along the length of the grating. Thus if the intensity of a particular wavelength increases or decreases (caused by a non-uniform strain field) it is possible to relate this event to the precise location along the grating. Previous studies [76] have shown that locations of cracks correspond to the locations of jumps or drops in the spectrum, Figure 72c. Hence chirped FBG can potentially provide a better quantitative assessment of the crack formation on the material surface than uniform FBGs would.

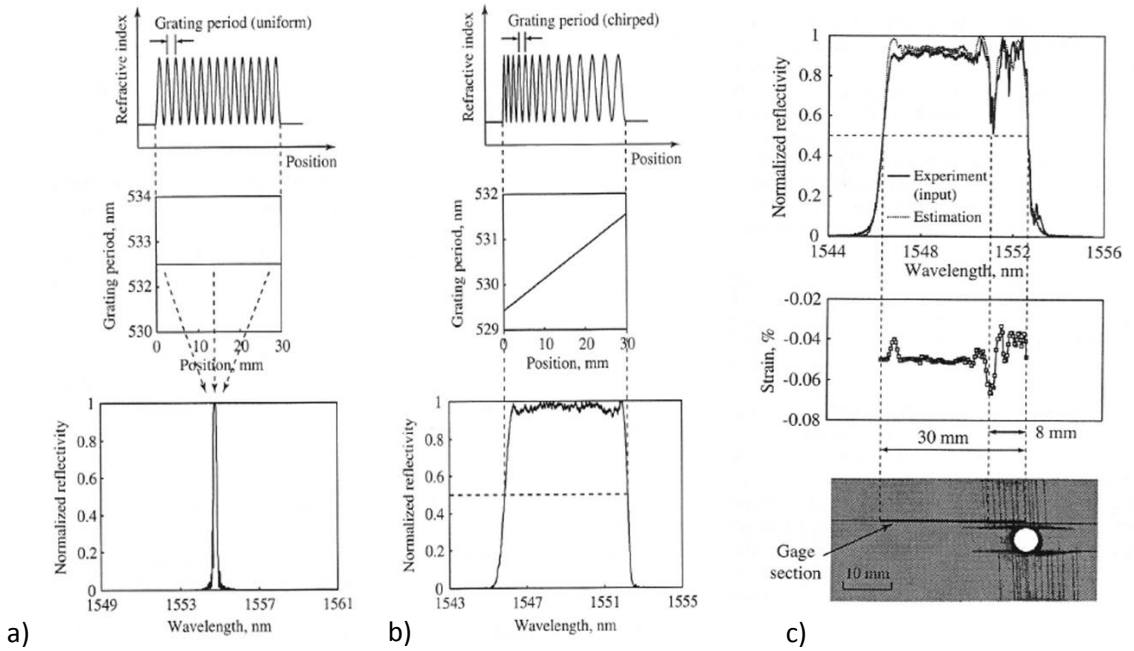

Figure 72: Schematic diagrams of the grating period and the reflected spectra of a) uniform FBG sensors and b) chirped FBG sensors, and c) relationship between FBG spectrum and damage pattern in the material [76].

6.3 Equipment Set-Up

Another parameter to consider when using FBG sensors is the equipment and the set-up used to measure Bragg wavelengths (i.e. OSA vs. interrogator). For the experimental work discussed in this report, an OSA and an interrogator were used which are characteristically different pieces of equipment and have their own benefits and limitations. An interrogator has a maximum sampling frequency of 250Hz and hence can be used for in-situ strain monitoring during cyclic testing. However, it does not capture the entire spectrum and acts as a black box by recording only time-stamped wavelength data. On the contrary, an OSA captures the entire spectrum that can potentially be used for health monitoring of the substrate material or the sensor integrity (e.g. bond quality). As it was shown in Chapter 4, when a specimen is substantially damaged and the signal from the sensor is severely distorted, the OSA data is easier to analyze and is more meaningful than the interrogator data. The most limiting factor of an OSA is the time required to scan through the whole spectrum. Hence it is cumbersome to use an OSA for measuring strain and capturing stiffness degradation. Overall, the choice regarding utilization of an OSA, an interrogator, or both depends on the objectives for the application of FBGs (i.e. damage or strain monitoring, or both) and the expected spectral changes throughout their lifetime. In general, an interrogator is recommended for strain measurements of materials that develop a minimal amount of damage (Chapter 5), whereas an OSA is recommended for damage monitoring and strain measurements of heavily damaged materials (Chapter 4).

Nonetheless, it is advantageous to employ both an OSA and an interrogator during initial tests of a new experimental program in order to evaluate the response of the specimens and the sensors, and to formulate the test protocol accordingly. These tests can be performed in conjunction with other conventional techniques used for damage, strain or temperature monitoring to provide a complete evaluation and calibration of FBGs. If chirping occurs when the interrogator is used as the primary device, it is recommended that the user or the operator examines the specimen and or the spectrum (via an OSA) to identify the possible source of chirping and its severity.

Additionally, an alternative set-up is proposed that can be used for simultaneous data acquisition with an OSA and an interrogator, as shown in Figure 73. In this arrangement an OSA and an interrogator are connected to the opposite ends of the optical fiber, and the interrogator records the reflected spectrum, and the OSA records the transmitted spectrum. The benefit of this set-up is that equipment does not have to be repeatedly disconnected and reconnected in order to take measurements. Hence wavelength data can be recorded continuously with an interrogator, and spectra can be captured with an OSA

during periodic dwell periods. Moreover, Prabhugoud *et al.* [79] wrote an interesting paper which examined the self-diagnostic capabilities of FBGs via the transmitted spectra.

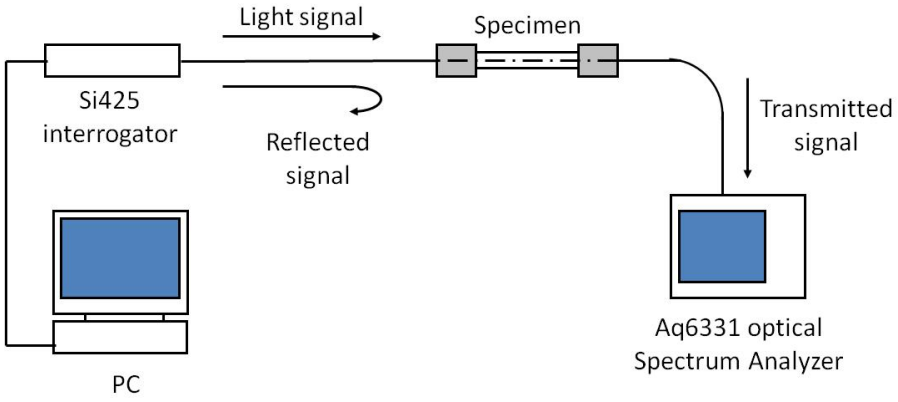

Figure 73: Experimental set-up that incorporates the use of an interrogator and an OSA.

6.4 Bonding

Results presented in Section 5.5 highlighted an important concern regarding premature debonding of surface mounted FBGs. The main difficulty in achieving a strong bond between a substrate and an FBG is related to its relatively small available bonding area. If an issue with achieving good bond integrity arises, it is suggested to consider application of a flat cladding OF. This type of optical fibers has flat sides and provides a larger area for bonding, Figure 74. Li *et al.* [12] had successfully used FBGs written on a flat cladding OF to characterize fatigue (R=-1) deformation of friction stir welded aluminum alloys at high strain amplitudes (5000 με).

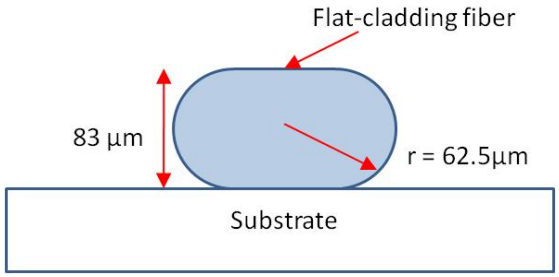

Figure 74: Schematic diagram of a flat-cladding optical fiber bonded to a substrate [12].

7 Conclusions and Future Work

7.1 Conclusions

Fiber Bragg grating sensors are perceived as attractive means for strain and damage monitoring of specimens during mechanical testing as well as for health monitoring of in-service components. The experimental programs conducted as a part of this thesis further investigated applicability of surface bonded and embedded FBGs for stiffness and damage monitoring of woven PMCs during tension-tension fatigue loading at different temperatures. In the meanwhile, the influence of temperature on the behavior of off-axis specimens was also investigated.

Implementation of embedded FBGs for monitoring carbon/epoxy on-axis woven laminates has shown their sensitivity to damage initiation and propagation. During the early stages of fatigue, these laminates developed matrix cracks in the overlap region between the warp and the weft fibers that resulted in severe chirping of the spectra. With further progression of cyclic loading, FBG spectrum was restored to a relatively clean shape. The proposed explanation of this change was debonding of the sensor due to delamination of the plies. In fact, final failure of the specimen was accompanied by complete delamination of the plies. Moreover, cross-sectional observation of a non-failed specimen showed extensive delamination. Overall, evolution of the FBG spectra during fatigue was coherent with the development of damage in these laminates.

It was found that woven specimens exhibited a significant reduction of stiffness during the early stages of fatigue and experienced subtle degradation throughout the remainder of the test. FBGs have successfully captured this trend. However, magnitudes of stiffness degradation measured with FBGs were not in precise agreement with the LVDT data. The main reason for this discrepancy was the misalignment of the OF. Results thus far demonstrate the applicability of embedded FBGs for stiffness monitoring, but additional work is required to assess their ability to accurately capture stiffness degradation.

Fatigued off-axis woven specimens have demonstrated an interesting failure mechanism that resembled necking of metallic materials. Microscopic observations of surface and cross-sectional areas have revealed the presence of matrix and transverse bundle cracks, and debonding and delamination between the bundles of the same and adjacent plies. The final fracture was localized and FBGs did not detect it. Nonetheless, FBG spectra were representative of the damage state of the material in the

vicinity of the sensor. Minimal damage was observed in non-failed specimens and in failed specimens in regions away from the fracture zone. As a result, the surface bonded FBGs have chirped only slightly in response to matrix and bundle cracks.

Moreover, the off-axis specimens exhibited a non-linear stress-strain response and demonstrated strong temperature dependence. An increase in test temperature has led to a reduction of stiffness, has increased non-linearity and has promoted strain ratcheting. The time-dependent behavior (e.g. stress relaxation) of the material was also evident at elevated temperatures. Overall, measurements made with FBG sensors were in good agreement with the strain gage data, and the sensors themselves possessed a significantly longer fatigue life than strain gages.

In conclusion, results of the experimental work presented in this thesis show the applicability of FBG sensors for damage and stiffness monitoring of textile PMCs during tension-tension fatigue at temperatures up to 200^{o}C. They also show potential for becoming the sensor of choice for in-situ structural health monitoring of components and parts made from PMCs.

7.2 Future Work

The future work will entail additional testing of PMCs at elevated temperatures with the application of FBG sensors for fatigue monitoring. These tests will be focused on fine-tuning the methodology used with FBGs, and on characterizing fatigue behavior of PMCs at ET. One series of tests will be performed with on-axis woven BMI specimens with the aim to investigate the effect of frequency on the fatigue performance of these specimens at ET. These tests will contribute to a comparison of failure mechanisms between on-axis and off-axis specimens cut from the same laminate. Another set of tests will involve carbon/MVK-10 braided PMCs and their fatigue properties will be evaluated at different temperatures (up to 300^{o}C) and frequencies. Future tests will be performed in an environmental chamber, which was recently purchased, and will eliminate issues with temperature gradients along the length of the specimen. Also, utilization of flat-cladding FBGs and an alternative OSA-interrogator set-up (Figure 73) will be considered.

8 Appendix – A

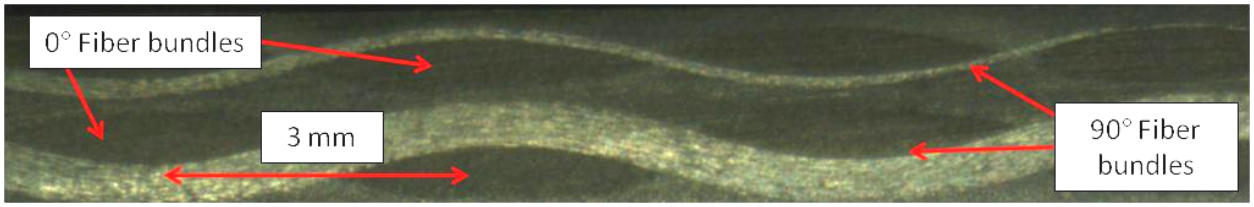

Figure A1: Cross-section of a woven specimen in its undamaged state.

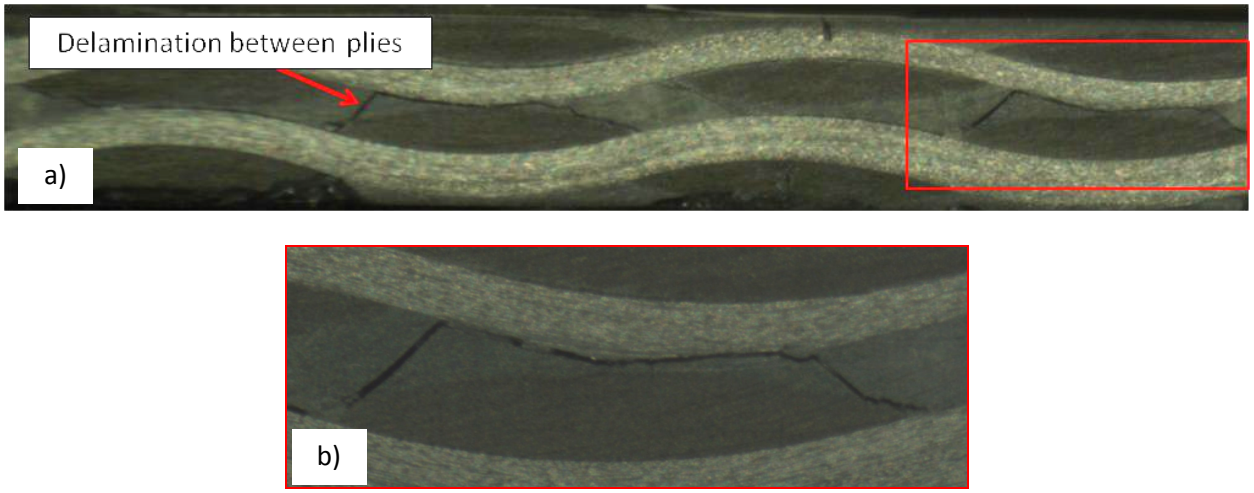

Figure A2: Propagation of delamination between the two woven plies; b) shows a magnified image of the section defined by a red box in (a).

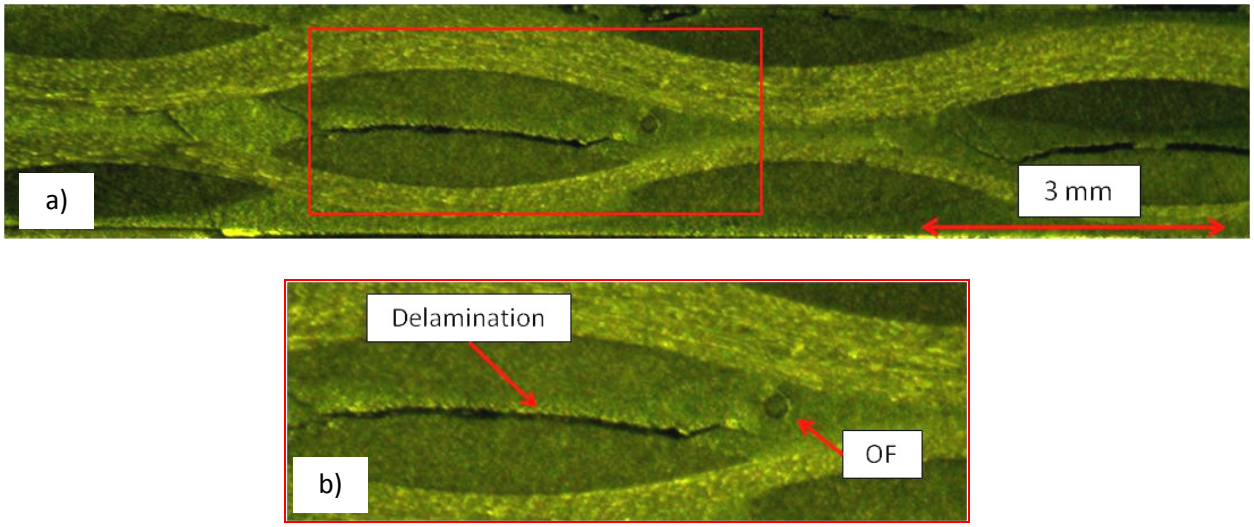

Figure A3: Presence of delamination in the vicinity of an OF captured at two magnifications; b) shows a magnified image of the section defined by a red box in (a).

Figure A4: Woven specimen in its original non-damaged state.

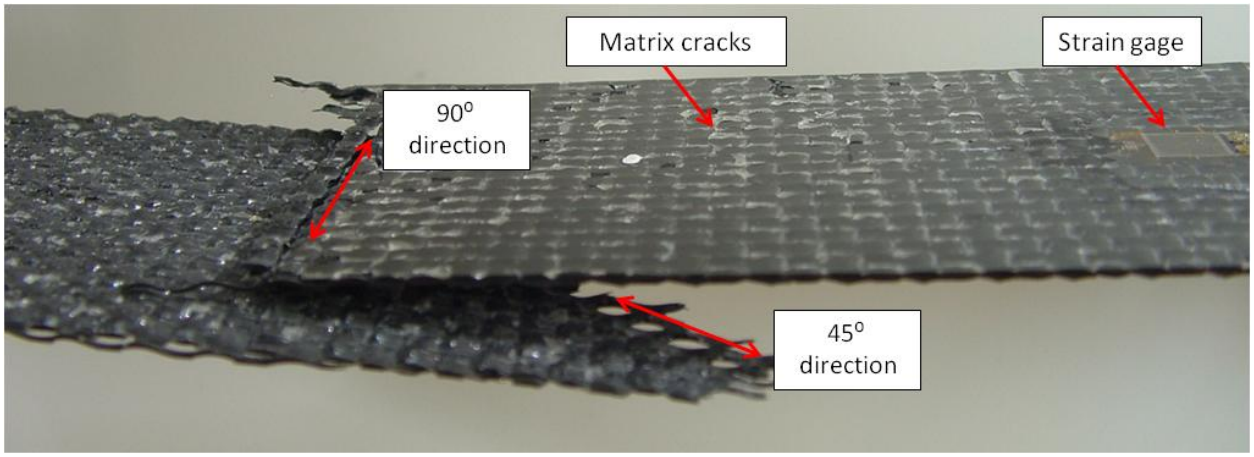

Figure A5: Fracture of a failed woven laminate.

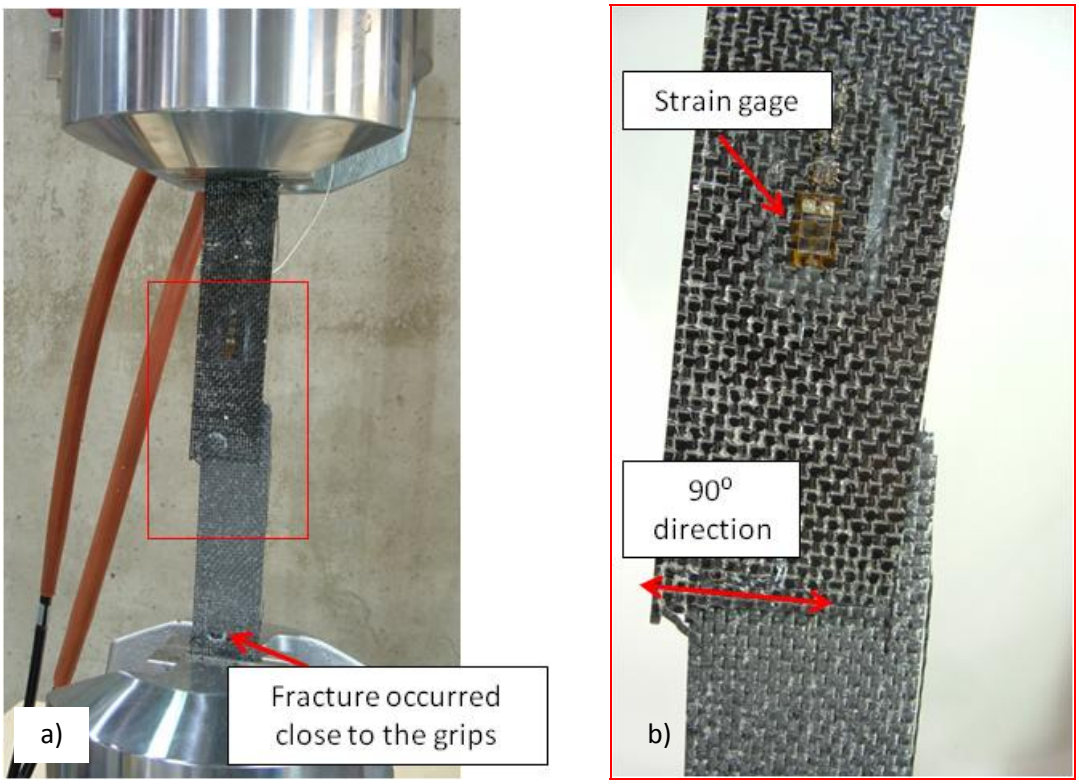

Figure A6: Fracture of a failed woven laminate; b) shows a magnified image of the section defined by a red box in (a).

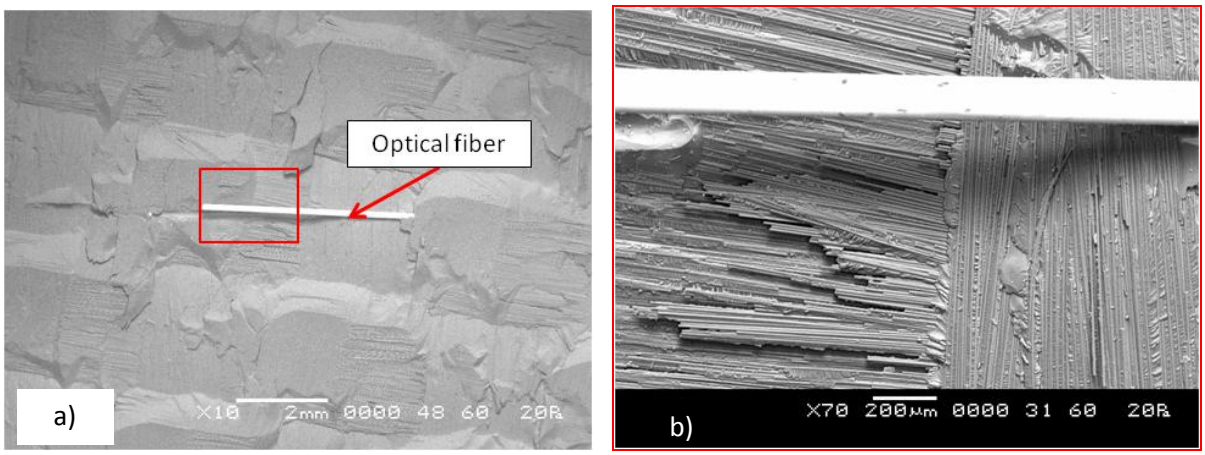

Figure A7: Fracture surface of a woven specimen with an embedded OF captured at a magnification of a) x10 and b) x70.

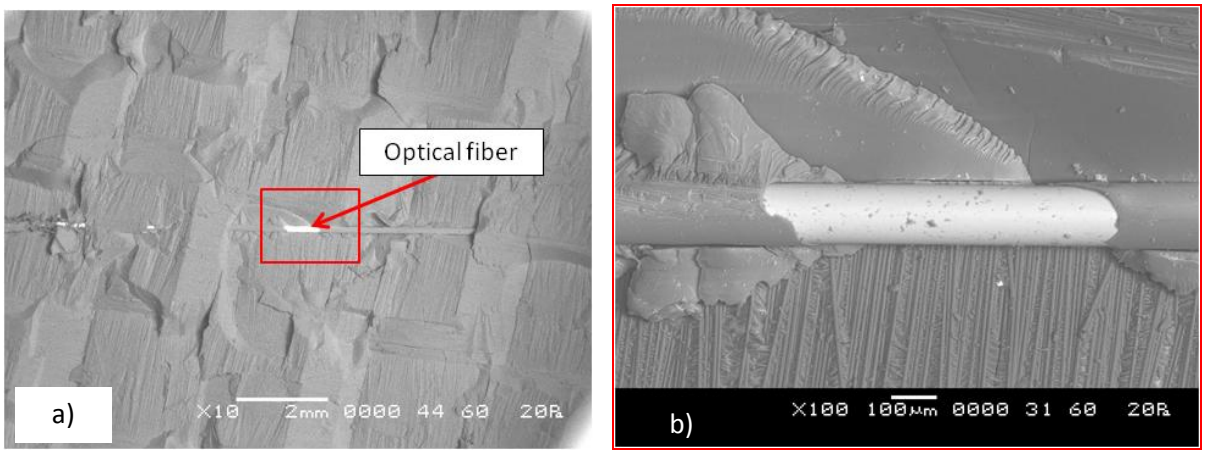

Figure A8: Fracture surface of a woven specimen with an embedded OF captured at a magnification of a) x10 and b) x100.

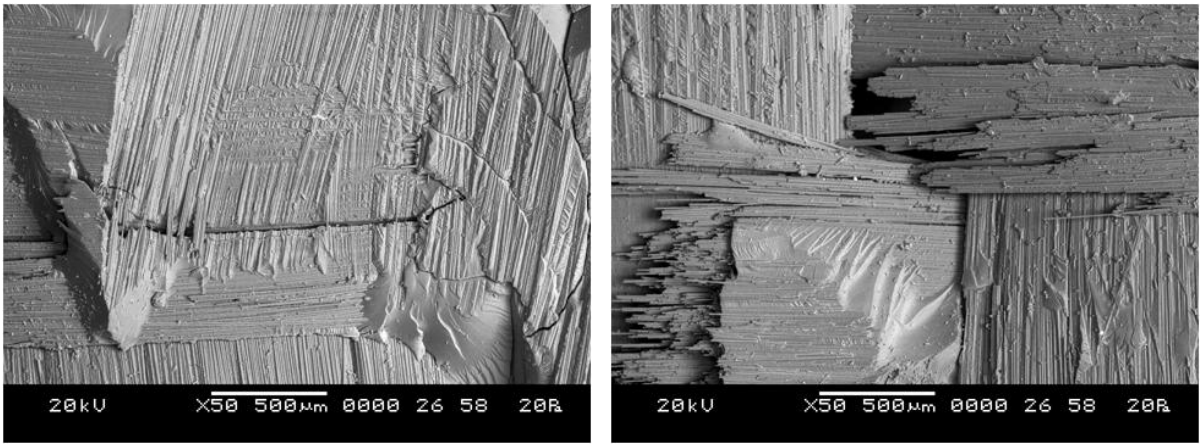

Figure A9: Fracture surfaces of a woven specimen captured at a magnification of x50.

9 Appendix – B

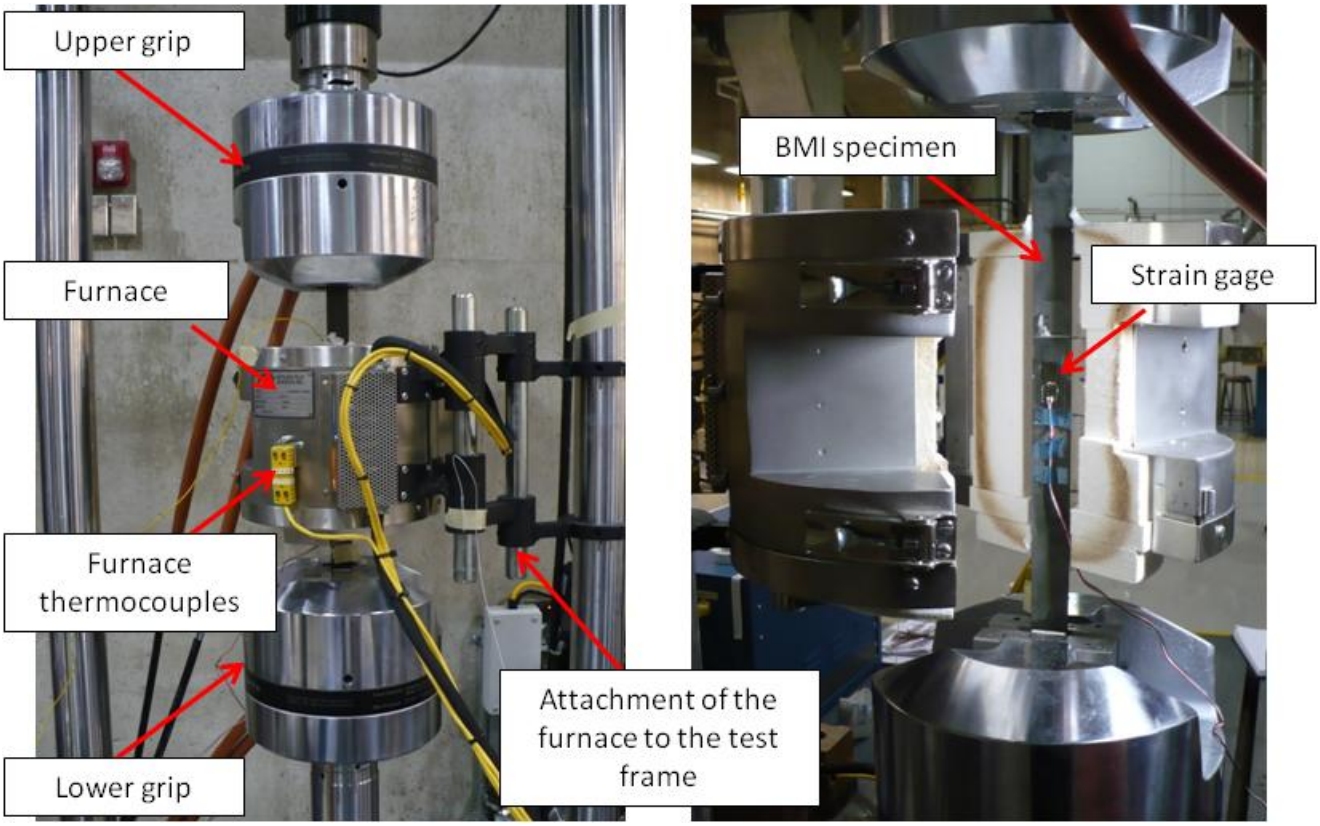

Figure B1: Experimental set-up showing the specimen, the grips and the furnace.

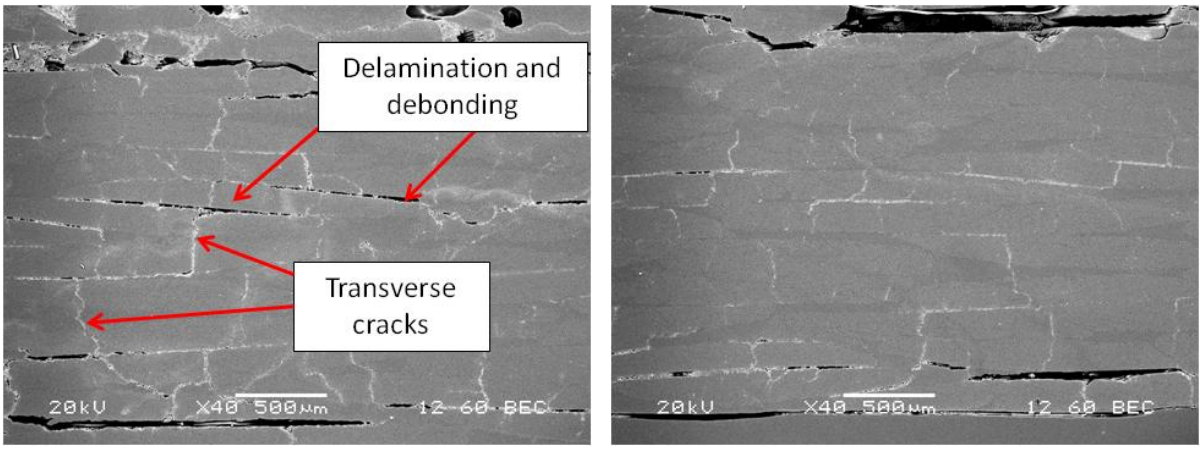

Figure B2: Cross-sectional images of samples taken from high-damage areas.

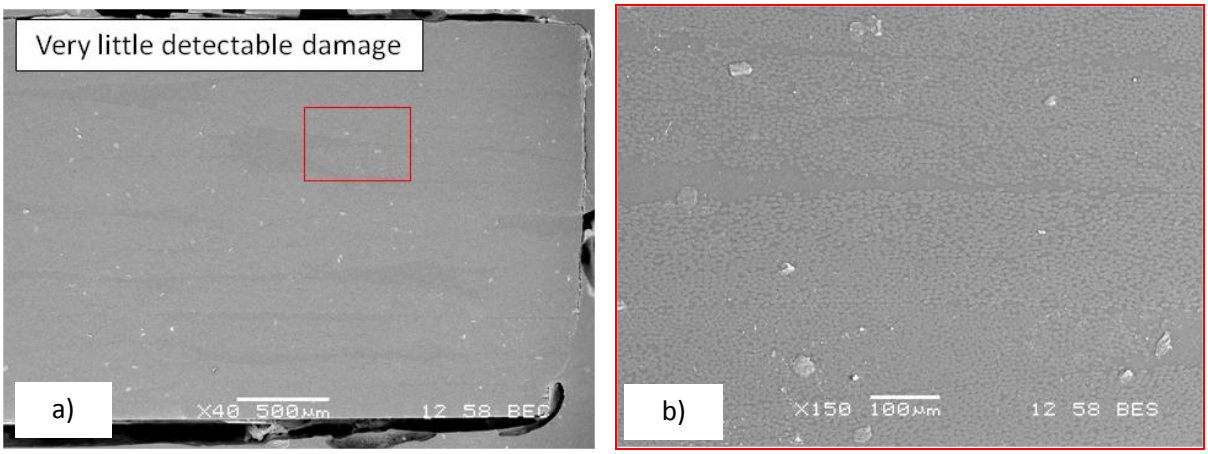

Figure B3: Cross-sectional images of samples from a low-damage area captured at a magnification of a) x40 and b) x150.

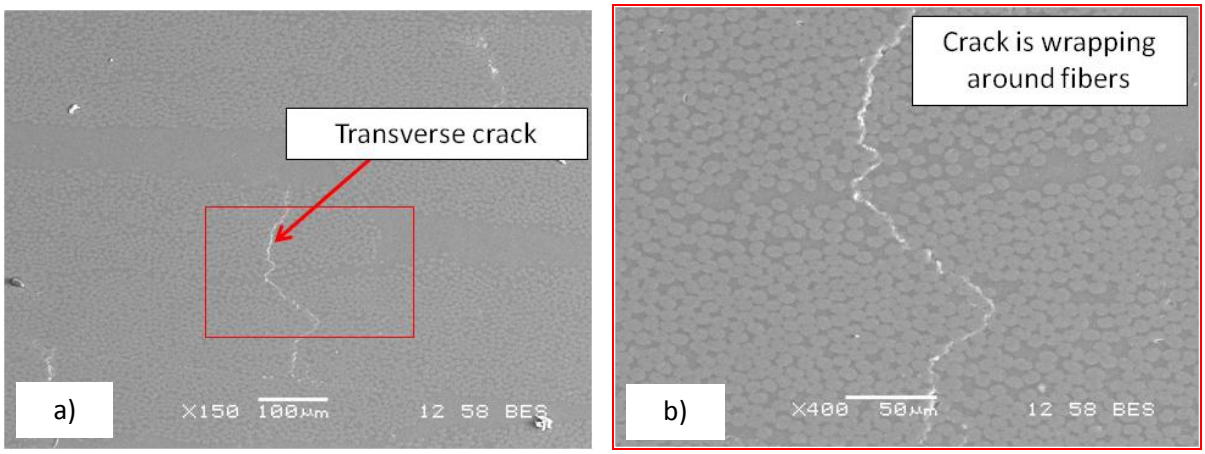

Figure B4: Propagation of transverse bundle cracks captured at a magnification of a) x150 and b) x400.

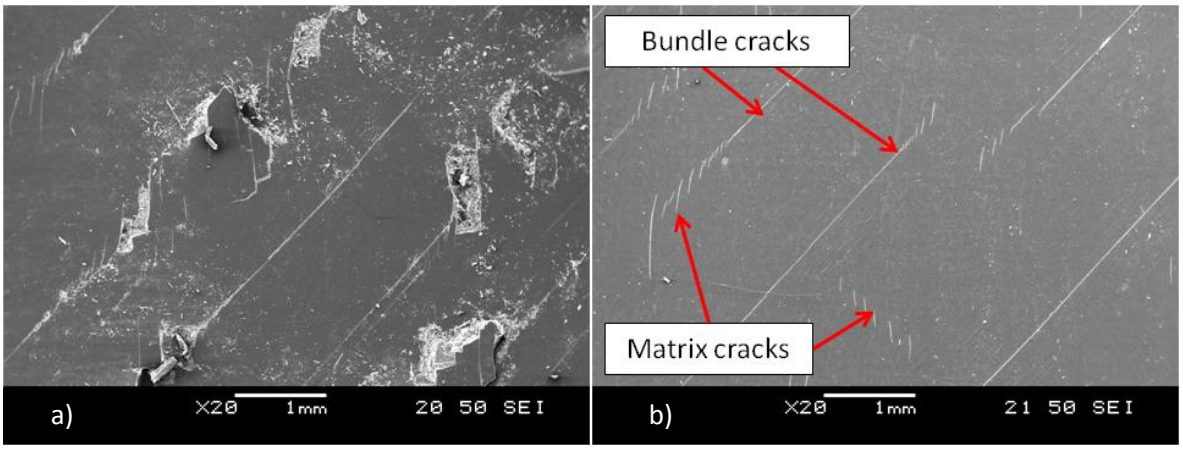

Figure B5: General pattern of bundle cracks and matrix cracks formed on the specimen surface in a) high-damage and b) low-damage areas.

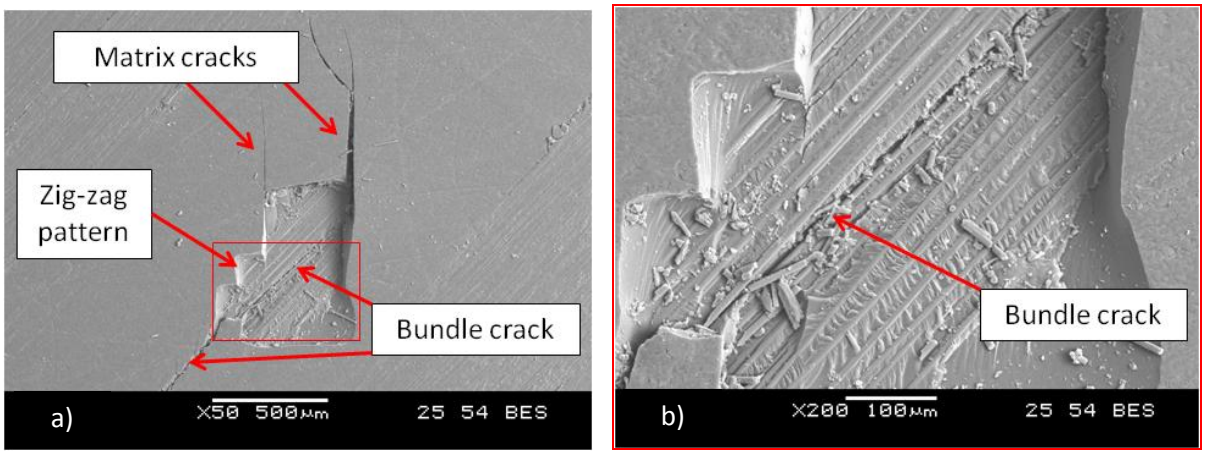

Figure B6: Interaction between bundle cracks and matrix cracks. Images were captured at a) x50 and b) x200.

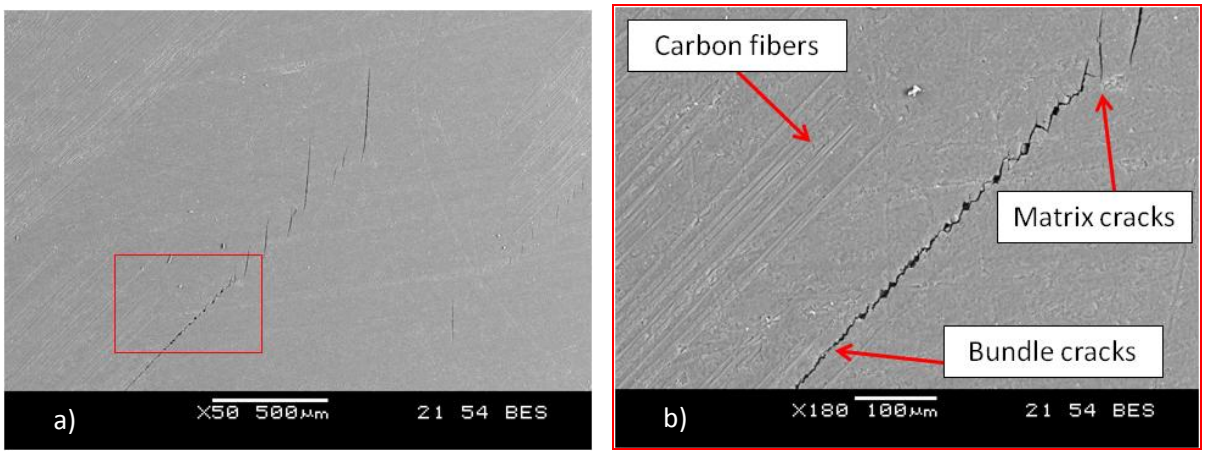

Figure B7: Transition between development of bundle cracks and matrix cracks. Images were captured at a) x50 and b) x180.

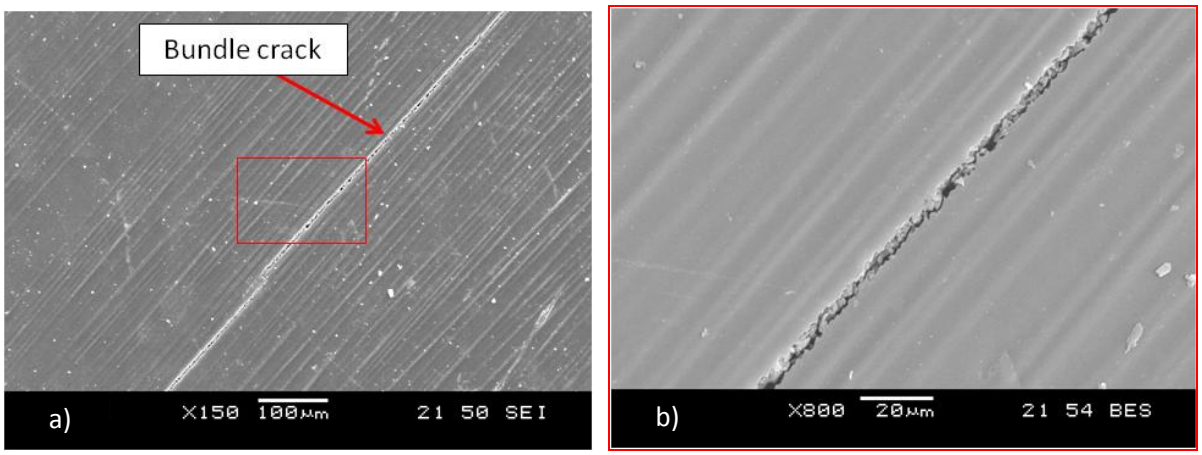

Figure B8: Surface of the specimen fatigued at room temperature captured at a magnification of a) x150 and b) x800.

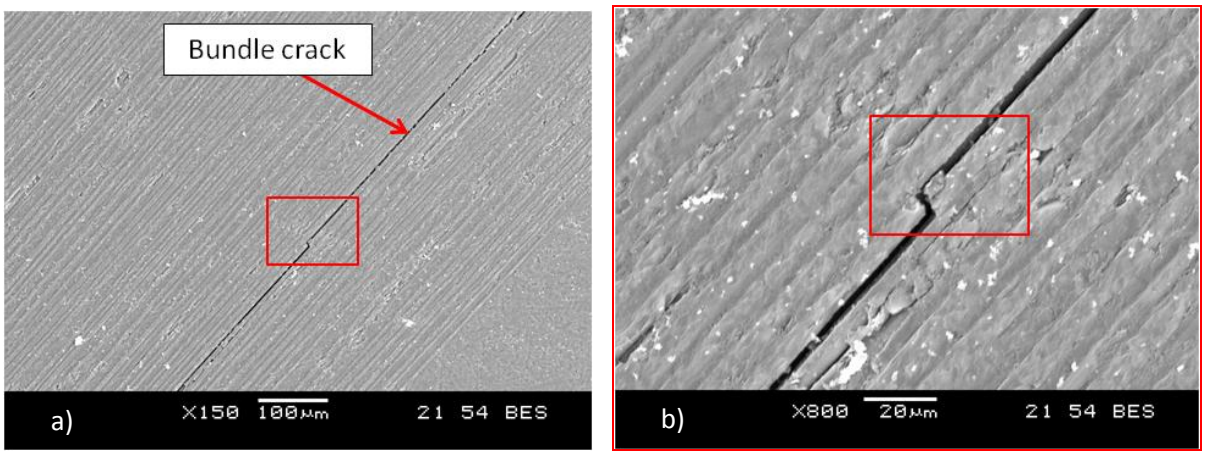

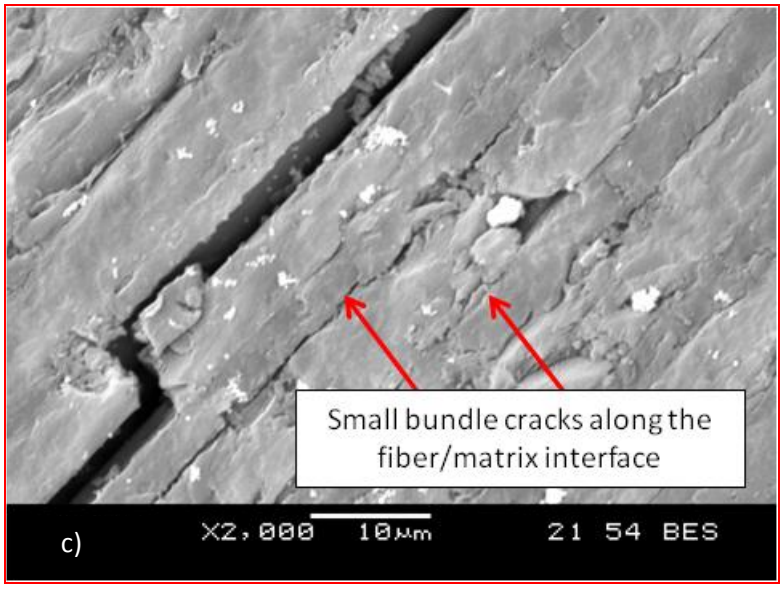

Figure B9: Surface of the specimens fatigued at ET captured at a magnification of a) x150, b) x800 and c) x2000.

10 References

1. Hansen, U. “Damage development in woven fabric composites during tension-tension fatigue.” *Journal of Composite Materials* 33-7 (1999): 614-639.
2. Huang, Z.-M., Teng, X. C. & Ramakrishna, S. “Fatigue behaviour of multilayer braided fabric reinforced laminates.” *Polymers & Polymer Composites* 12-1 (2005): 73-81.
3. Fouinneteau, M. R. C. & Pickett, A. K. “Shear mechanism modelling of heavy tow braided composites using a meso-mechanical damage model.” *Composites: Part A 28* (2007): 2294-2306.
4. Lomov, S. V., Ivanov, D. S., Truong, T. C., Verpoest, I., Baudry, F., Vanden Bosche, K. & Xie, H. “Experimental methodology of study of damage initiation and development in textile composites in uniaxial tensile test.” *Composite Science and Technology* 68 (2008): 2340-2349.
5. Jen, M.-H. R., Tseng, Y.-C., Kung, H.-K. & Huang, J. C. “Fatigue response of APC-2 composite laminates at elevated temperatures.” *Composites: Part B* 39 (2008): 1142-1146.
6. Khan, R., Khan, Z., Al-Sulaiman, F. & Merah, N. “Fatigue life estimates in woven carbon fabric/epoxy composites at non-ambient temperatures.” *Journal of Composite Materials* 36 (2002): 2517-2535.
7. Shimokawa, T., Kakuta, Y., Saeki, D. & Kogo, Y. “Carbon plain-weave fabric low-temperature vacuum cure epoxy composite: static and fatigue strength at room and high temperatures and practicality evaluation.” *Journal of Composite Materials* 41-18 (2007): 2245-2265.
8. Shimokawa, T., Kakuta, Y., Hamaguchi, Y. & Aiyama, T. “Static and fatigue strengths of a G40-800/5260 carbon fiber/bismaleimide composite material at room temperature and 150C.” *Journal of composite Materials* 42-7 (2008): 655-679.
9. Jen, M.-H. R., Tseng, Y.-C. & Lin, W.-H. “Thermo-mechanical fatigue of centrally notched and unnotched AS-4/PEEK APC-2 composite laminates.” *International Journal of Fatigue* 28 (2006): 901-909.
10. Kobayashi, S. & Takeda, N. “Experimental characterization of microscopic damage behavior in carbon/bismaleimide composite-effects of temperature and laminate configuration.” *Composites: Part A* 33 (2002): 1539-1538.
11. Ahci, E. & Talreja, R. “Characterization of viscoelasticity and damage in high temperature polymer matrix composites.” *Composites Science and Technology* 66 (2006): 2506-2519.
12. Li, C., Feng, A. H., Gu, X. J. & Chen, D. L. “Localized cyclic strain measurements of friction stir welded aluminum alloy using a flat-cladding optical fiber sensor array.” Manuscript submitted to *Sensors Journal* (2009).
13. De Baere, I., Luyckx, G., Voet, E., Van Paepegem, W. & Degrieck, J. “On the feasibility of optical fibre sensors for strain monitoring in thermoplastic composites under fatigue loading conditions.” *Optics and Lasers in Engineering* 47 (2009): 403-411.

14. Kosaka, T., Osaka, K., Nakakita, S. & Fukuda, T. “Fiber optic strain monitoring of textile GFRP during RTM molding and fatigue tests by using embedded FBG sensors.” *Proceedings of Smart Structures and Materials* (2003): 73-80.

15. Takeda, S., Okabe, Y. & Takeda, N. “Delamination detection in CFRP laminates with embedded small-diameter fiber Bragg grating sensors.”*Composites: Part A* 33(2002): 970-980.

16. Takeda, S., Yamanoto, T., Okabe, Y. & Takeda, N. “Debonding Monitoring of composite repair patches using embedded small-diameter FBG sensors.” *Smart Materials and Structures* 16 (2007): 763-770.

17. Kadoya, A., Yashiro, S. & Okabe, T. “Prediction of fatigue damage in holed composite laminates with embedded FBG sensors.” *Proceedings of ICCM-17* (2008).

18. Takeda, Nobuo. “Characterization of microscopic damage in composite laminates and real-time monitoring by embedded optical fiber sensors.” *International Journal of Fatigue* 24 (2002): 281-289.

19. Kawai, M. & Taniguchi, T. “Off-axis Fatigue behavior of plain weave carbon/epoxy fabric laminates at room and high temperatures and its mechanical modeling.” *Composites: Part A* 37 (2006): 243-256.

20. Tate, J. S. & Kelkar, A. D. “Stiffness degradation model for biaxial braided composites under fatigue loading.” *Composites: Part B* 39 (2008): 548-555.

21. Branco, C. M., Ferreira, J. M., Faelt, P. & Richardson, M. O. W. “A comparative study of the fatigue behaviour of GRP hand lay-up and pultruded phenolic composites.” *International Journal of Fatigue* 18-4 (1995): 255-263.

22. Kawai, K., Yajima, S., Hachinohe, A. & Kawase, Y. “High-temperature off-axis fatigue behaviour of unidirectional carbon-fibre-reinforced composites with different resin matrices.” *Composites Science and Technology* 61 (2001): 1285-1302.

23. Cain, K. J., Glinka, G. & Plumtree, A. “Damage evolution in an off-axis unidirectional graphite bismaleimide composite loaded in tension.” *Composites: Part A* 34 (2003): 987-993.

24. Tamuzs V., Dzelzitis, K. & Reifsnider, K. “Fatigue of woven composite laminates in off-axis loading I. The master curves.” *Applied Composite Materials* 11 (2004): 259-279.

25. Tamuzs, V., Dzelzitis, K. & Reifsnider, K. “Fatigue of woven composite laminates in off-axis loading II. Prediction of the cyclic durability.” *Applied Composite Materials* 11 (2004): 281-293.

26. Tamuzs, V., Dzelzitis, K. & Reifsnider, K. “Prediction of the cyclic durability of woven composite laminates.” *Composites Science and Technology* 68 (2008): 2717-2721.

27. Shen, X., Xia, Z. & Ellyin, F. “Cyclic deformation behavior of an epoxy polymer. Part I: Experimental investigation.” *Polymer Engineering and Science* 44-12 (2004): 2240-2246.

28. Hwang, W. & Han, K. S. “Fatigue of composites – fatigue modulus concept and life prediction.” *Journal of Composite Materials* 20 (1986): 154-165.

29. Cain, K. J., Glinka, G. & Plumtree, A. “Cyclic damage characterization of an off-axis unidirectional graphite bismaleimide composite.” *Canadian Metallurgical Quarterly* 45-4 (2006): 433-440.

30. Miyano, Y., Nakada, M. & Nishigaki, K. “Prediction of long-term fatigue life of quasi-isotropic CFRP laminates for aircraft use.” *International Journal of Fatigue* 28 (2006): 1217-1225.

31. Noda, J., Nakada, M. & Miyano, Y. “Fatigue life prediction under variable cyclic loading based on statistical linear cumulative damage rule for CFRP laminates.” *Journal of Reinforced Plastics and Composites* 26-7 (2007): 665-680.

32. Guedes, R. M. “Durability of polymer matrix composites: viscoelastic effect on static and fatigue loading.” *Composites Science and Technology* 67 (2007): 2574-2583.

33. Guedes, R. M. “Creep and fatigue lifetime prediction of polymer matrix composites based on simple cumulative damage laws.” *Composites: Part A* 39 (2008): 1716-1725.

34. Miyano, Y. & Nakada, M. “Prediction of flexural fatigue strength of CRFP composites under arbitrary frequency, stress ration, and temperature.” *Journal of Composite Materials* 31-6 (1997): 619-638.

35. Counts, W. A. & Johnson, W. S. “Bolt bearing fatigue of polymer matrix composites at elevated temperatures.” *International Journal of Fatigue* 24 (2002): 197-204.

36. Uematsu, Y., Kitamura, T. & Ohtani, R. “Delamination behavior of a carbon-fiber-reinforced thermoplastic polymer at high temperatures. “ *Composites Science and Technology* 53 (1995): 333-341.

37. Gates, T. S. “Effects of elevated temperature of the viscoplastic modeling of graphite/polymeric composites.” *NASA Technical Memorandum* 104160 (1991): 1-29.

38. Gregory, J. R. & Spearing, S. M. “Constituent and composite quasi-static and fatigue fracture experiments.” *Composites: Part A* 36 (2005): 665-674.

39. Miyano, Y., McMurray, K., Enyama, J. & Nakada, M. “Loading rate and temperature dependence on flexural fatigue behavior of a satin woven CFRP laminate.” *Journal of Composite Materials* 28-13 (1994): 1250-1260.

40. Jen, M.-H. R. & Lee, C.-H. “Strength and life in thermoplastic composite laminates under static and fatigue loads. Part II: Formulation.” International Journal Fatigue 20-9 (1998): 617-629.

41. Tang, R., Guo, Y.-J. & Weitsman, Y. J. “An appropriate stiffness degradation parameter to monitor fatigue damage evolution in composites.” *International Journal of Fatigue* 26 (2004): 421-427.

42. Ju, J. & Morgan, R. J. “Characterization of microcrack development in BMI-carbon fiber composite under stress and thermal cycling.” *Journal of Composite Materials* 38-22 (2004): 2007-2024.

43. Shimokawa, T. “Effect of thermal cycling on microcracking and strength degradation of high-temperature polymer composite materials for use in next-generation SST structures.” *Journal of Composite Materials* 36-7 (2002): 885-895.

44. Shah, A. R., Murphy, P. L. N. & Chamis, C. C. “Effect of cyclic thermo-mechanical loads on fatigue reliability in polymer matrix composites.” *NASA Technical Memorandum* 107091 (1995): 1-15.

45. De Oliveira, R., Ramos, C. A. & Marques, A. T. “Health monitoring of composite structures by embedded FBG and interferometric Fabry-Perot sensors.” *Computers and Structures* 86 (2008): 340-346.

46. Measures, R. M. “Structural monitoring with fiber optic technology.” *Academic Press*, 2001.

47. Kersey, A. D., Davis, M. A., Patrick, H., LeBlanc, J. M., Koo, K. P., Askins, C. G., Putnam, M. A. & Friebele, E. J. “Fiber grating sensors.” *Journal of Lightwave Technology* 15-8 (1997): 1442-1463.

48. Tao, X., Tang, L., Du, W. & Ad Choy, C. “Internal strain measurement by fiber Bragg grating sensors in textile composites.” *Composite Science and Technology* 60 (2000).

49. Jung, K. & Kang, T. J. “Cure monitoring and internal strain measurement of 3-D hybrid braided composites using Fiber Bragg Grating sensor.” *Journal of Composite Materials*, Vol. 41, No. 12, 2007.

50. Kuang, K. S. C. & Cantwell, W. J. “Use of conventional optical fibers and fiber Bragg gratings for damage detection in advanced composite structures: A review.” *Applied Mech*. Rev. 56-5 (2003): 493-513.

51. Surgeon, M. & Wevers, M. “The influence of embedded optical fibers on the fatigue damage progress in quasi-isotropic CFRP laminates.” *Journal of Composite Materials* 35-11 (2001): 931-940.

52. Takeda, N., Okabe, Y. & Mizutani, T. “Damage detection in composites using optical fibre sensors.” *JAERO* (2007): 497-508.

53. Yuan, S., Huang, R. & Yunjiang, R. “Internal strain measurement in 3D braided composites using co-braided optical fiber sensors.” *Journal of Mater. Sci. Technol*. 20-1 (2004): 199-202.

54. Jung, K. & Kang, T. J. “Cure monitoring and internal strain measurement of 3-D hybrid braided composites using fiber Bragg grating sensors.” *Journal of Composite Material* 42-12 (2007): 1499-1521.

55. Tao, X., Tang, L., Du, W. & Choy, C. “Internal strain measurement by fiber Bragg grating sensors in textile composites.” *Composite Science and Technology* 60 (2000) 657-669.

56. Vieira, A., De Oliveira, R., Frazao, O., Baptista, J. M. & Marques, A. T. “Effect of the recoating and the length of fiber Bragg grating sensors embedded in polymer composites.” *Materials and Design* 30 (2009): 1817-1821.

57. Li, W. Y., Cheng, C. C. & Lo, Y. L. “Investigation of strain transmission of surface-bonded FBGs used as strain sensors.” *Sensors and Actuators A* 149 (2009): 201-207.

58. Malik, S. A., Mahendran, R. S., Harris, D., Paget, M. & Pandita, S. D. “Finite element modeling of fiber Bragg grating strain sensors and experimental validation.” *Proceedings of Sensors and Smart Structures Technologies for Civil, Mechanical, and Aerospace Systems* (2009).

59. Metthewson, M. J. & Padiyar, V. “Cyclic fatigue of high strength optical fibers in bending.” *Proceedings of Optical Fiber and Fiber component Mechanical Reliability and Testing* (2001).

60. Ling, H.-Y., Lau, K.-T., Jin, W. & Chan, K.-C. “Characterization of dynamic strain measurement using reflection spectrum from a fiber Bragg grating.” *Optics Communications* 270 (2007): 25-30.

61. Shin, C. S. & Chiang, C. C. “Fatigue damage monitoring in polymeric composites using multiple fiber Bragg gratings.” *International Journal of Fatigue* 28 (2006): 1315-1321.

62. Ling, H.-Y., Lau, K.-T., Cheng, L. & Jin, W. “Utilization of embedded optical fibre sensors for delamination characterization in composite laminates using a static strain method.” *Smart Materials and Structures* 14 (2005): 1377-1386.

63. Ling, H.-Y., Lau, K.-T., Su, Z. & Wong, E. T.-T. “Monitoring mode II fracture behavior of composite laminates using embedded fiber-optic sensors.” *Composites: Part B* 38 (2007): 488-497.

64. Peters, K., Studer, M., Botsis, J., Locco, A., Limberger, H. & Salathe, R. “Embedded optical fiber Bragg grating sensor in a nonuniform strain field: measurements and simulations.” *Experimental Mechanics* 41-1 (2001): 19-28.

65. Guemes, A., Fernandez-Lopez, A., Dominguez, C. & de Miguel, C. “Experimental determination of strain in-homogeneities in woven laminates by FBG.” *Proceedings of ICCM-17* (2009).

66. Kosaka, T., Kurimoto, H., Osaka, K., Nakai, A., Osaka, T., Hamada, H. & Fukuda, T. “Strain monitoring of braided composites by using embedded fiber-optic strain sensors.” *Advanced Composite Materials* 13-3 (2004): 157-170.

67. Kuang, K. S. C., Kenny, R., Whelan, M. P, Cantwell, W. J. & Chalker, P. R.”Embedded fibre Bragg grating sensors in advanced composite materials.” *Composites Science and Technology* 61 (2001): 1379-1387.

68. Ussorio, M., Wang, H., Ogin, S. L., Thorne, A. M., Reed, G. T., Tjin, S. C. & Suresh, R. “Modification to FBG sensor spectra due to matrix cracking in a GFRP composite.” *Construction and Building Materials* 20 (2006): 111-118.

69. Mizutani, T., Okabe, Y. & Takeda, N. “Quantitative evaluation of transverse cracks in carbon fiber reinforced plastic quasi-isotropic laminates with embedded small-diameter fiber Bragg gratings sensors.” *Smart Materials and Structures* 12 (2003): 898-903.

70. Palaniappan, J., Wang, H., Ogin, S. L., Thorne, A., Reed, G. T., Tjin, S. C. & McCartney, L. N. “Prediction of the reflected spectra from chirped fibre Bragg gratings embedded within cracked crossply laminates.” *Measurement Science and Technology* 17 (2006): 1609-1614.

71. Okabe, Y., Tsuji, R. & Takeda, N. “Application of chirped fiber Bragg grating sensors for identification of crack locations in composites.” *Composites: Part* A 35 (2004): 59-65.

72. Leng, J. S. & Asundi, A. “Non-destructive evaluation of smart materials by using extrinsic Fabry-Perot interferometric and fiber Bragg grating sensors.” *NDT & E International* 35 (2002): 273-276.

73. Leng, J. S. & Asundi, A. “Structural health monitoring of smart composite materials by sing EFPI and FBG sensors.” *Sensors and Actuators A* 103 (2003): 330-340.

74. Yashiro, S., Takeda, N., Okabe, T. & Sekine, H. “A new approach to predicting multiple damage states in composite laminates with embedded FBG sensors.” *Composites Science and Technology* 65 (2005): 659-667.

75. Yashiro, S., Murai, K, Okabe, T. &Takeda, N. “Numerical study for identifying damage in open-hole composites with embedded FBG sensors and its application to experiment results.” *Advance Composite Materials* 16-2 (2007): 115-134.

76. Yashiro, S., Okabe, T. & Takeda, N. “Damage identification in a holed CFRP laminate using a chirped fiber Bragg grating sensor.” Composites Science and Technology 67 (2007): 286-295.

77. Kolubinski, L. “On the use of fiber optic sensors embedded in fiber reinforced polymers.” *MASc Thesis*, Ryerson University, Toronto, On., Canada, 2008.

78. Lu, H., Hussian, R., Zhou, M. & Gu, X. “Fiber Bragg grating sensors for failure detection of flip chip ball grid array in four-point bend tests,” *IEEE Sensors Journal*, 2008.

79. Prabhugoud, M., Peters, K., Pearson, J. & Zikry, M. A. “Independent measurement of strain and sensor failure features in Bragg grating sensors through multiple mode coupling.” Sensors and Actuators A 135 (2007): 433-442.